Materials under extreme conditions: applications to the study of the interior of solar and extrasolar planets

Tesis
entregada a la
Universidad de Chile
en cumplimiento parcial de los requisitos
para optar al grado de
Doctor en Ciencias con mención en Física
Facultad de Ciencias

por

Felipe Javier González Cataldo

Marzo, 2015

Directores de Tesis: **Dr. Gonzalo Gutiérrez Gallardo**
Dr. Sergio Davis Irarrázabal

FACULTAD DE CIENCIAS
UNIVERSIDAD DE CHILE

INFORME DE APROBACIÓN
TESIS DE DOCTORADO

Se informa a la Escuela de Postgrado de la Facultad de Ciencias que la Tesis de Doctorado presentada por el candidato

Felipe Javier González Cataldo

ha sido aprobada por la Comisión de Evaluación de la Tesis como requisito para optar al grado de Doctor en Ciencias con mención en Física, en el examen de Defensa de Tesis rendido el día 21 de Enero de 2015.

Directores de Tesis

Dr. Gonzalo Gutiérrez
Gonzalo Gutiérrez

Dr. Sergio Davis
S Davis

Comisión de Evaluación de la Tesis

Dr. Patricio Rojo

Dr. Ricardo Ramirez
R Ramirez

Dr. Rodrigo Soto

Dr. Martin Reich

A mi mamá.

Nunca te olvidaré.

BIOGRAFÍA

Nací en Santiago el 14 de noviembre de 1985, e ingresé a la Licenciatura en Ciencias con Mención en Física en Universidad de Chile en 2004, sin duda uno de los hitos más importantes de mi vida. No sólo cambió mi forma de ver la física, sino mi forma de ver la vida, de una manera mucho más crítica, analítica y profunda. Junto con aprender a estudiar, analizar y comprender la naturaleza a través de la física, aprendí a programar, lo cual representó otro hito importante en mi vida. La programación computacional despertó en mi una nueva pasión (y a veces, obsesión) que deseaba comprender y aplicar. Es este punto en el que usar la programación como una herramienta para estudiar complejos problemas de mi pasión primaria, la física.

Comencé el programa de doctorado el año 2009. En un esfuerzo por combinar los conocimientos computacionales del mundo atómico de la materia condensada y satisfacer mi curiosidad por el universo en general, nace la idea principal de esta tesis: estudiar el interior de planetas solares y extrasolares. Una estadía de 5 meses en la University of California Berkeley ayudó de sobremanera a concretar esta idea, y además me dió la posibilidad de vivir en otro país, desarrollando ciencia de primer nivel, una grata experiencia que jamás olvidaré. Espero que el tiempo y esfuerzo dedicado al trabajo realizado durante estos años de doctorado se vean reflejados en esta tesis, que espero que el lector disfrute, así como yo disfruté realizándola.

AGRADECIMIENTOS

La presente tesis es un esfuerzo en el cual, directa o indirectamente participaron varias personas, ya sea leyendo, opinando, corrigiendo, aportando información relevante, o bien, dándome ánimo y teniéndome paciencia. Por eso y mucho más, quiero entregar mi más sincero agradecimiento:

A mi madre, cuyo temprano fallecimiento marcó mi vida, pero fue y será para mí el mejor ejemplo de perseverancia, esfuerzo y superación, valores que me han inspirado a seguir adelante y crecer en el campo científico, que es lo que me apasiona.

A mi padre, quien siempre me ha apoyado, aconsejado, animado y estado presente en mi vida, esforzándose por inculcarme el amor por los estudios y el conocimiento, entregándome largas horas de enseñanza y dedicación que forjaron mi tenacidad académica.

A mi amada Aylin, mi compañera, amiga, y confidente quien ha estado conmigo por más de 8 años, viendo de cerca mi recorrido académico, cediendo paciente y generosamente grandes espacios de tiempo a mi realización profesional. Su amor y apoyo han sido fundamentales para salir adelante y lograr una vida feliz.

A mis hermanos, familiares y amigos en general, que con su presencia e interés en mi trabajo, de una u otra forma han aportado mucho a mi vida y a mi desarrollo personal.

A las personas que gentilmente me concedieron parte de su tiempo, entregándome información y conocimientos esenciales para sustentar esta investigación.

A Burkhard Militzer, quien fue mi tutor en la University of California, Berkeley, y me entregó conocimientos claves para el desarrollo de esta tésis.

A mi cotutor, Sergio Davis, sin cuyos conocimientos, consejos y habilidades computacionales, el desarrollo de esta tesis no habría sido posible.

Y, especialmente, a mi profesor guía Gonzalo Gutiérrez quien siempre demostró confianza e interés en mi trabajo. No sólo me asesoró en la realización de éste y estuvo llano a contestar amablemente todas mis preguntas e inquietudes, sino que además me ayudó en diversos aspectos de mi vida personal y lo considero ahora un amigo.

Mi permanencia en el plan de doctorado fue posible gracias a la Beca CONICYT Nº 201090712 para estudios de doctorado en Chile, año académico 2009, y mi estadía en la University of California, Berkeley, gracias a la Beca de Estadías Cortas de Investigación en el Extranjero, otorgada por la Universidad de Chile. Este trabajo ha sido parcialmente financiado por FONDECYT, proyecto No. 1120603, y Proyecto Anillo ACT/24.

Contents

ABSTRACT

Extrasolar planets are formed by accretion of the material available in the initial molecular cloud that forms the protoplanetary disk, which includes silicates, iron, graphite and polycyclic aromatic hydrocarbons. Since direct observation or measurement of the composition are not yet possible, several models for the internal structure of a planet have been built on the basis of measurements of its mass and radius, coupled with a possible range of compositions. These models rely on the knowledge about the properties of the materials that are part of the composition, which are known to be under very high pressures and temperatures in the different layers that form the planet. Hence, these models and our understanding of planetary evolution will be more accurate to the extent that we know the changes induced by pressure and temperature on these materials and the interactions carried out between them at the extreme conditions reached in their interiors.

This thesis presents a succession of ab initio studies about materials relevant for planetary interiors, which include iron and silica, aimed to address different scenarios inside gas giants and super-Earths after its formation. The first study deals with the erosion of the rocky core of gas giants due to the presence of metallic hydrogen, where silica, one of the main candidates for the rocky-core composition, has been chosen as a representative material. In this study, the free energy of solvation of silica into metallic hydrogen was calculated, using the thermodynamic integration technique to get the Helmholtz free energy from molecular dynamics simulations. The study reveals that, for the thermodynamic conditions present in the core–mantle boundary of the gas giants of our solar system, erosion is energetically favored, in good agreement with calculations performed for other rocky core materials, like water ice, periclase and iron, which can also be dissolved by hydrogen. These results have major im-

plications for the evolution of giant planets, since erosion, coupled with convection, may explain the enrichment in heavy elements in giant planet atmospheres.

The second study addresses the melting properties of silica for pressures relevant to the core of giant planets and the mantle of super-Earths, where silica is also expected to be very abundant. The results of this study reveal an abrupt increase in the melting curve previously reported by other studies, and extend the curve up to 6000 GPa. The implications of this study modify the picture of stable rocky cores in giant planet interiors, since they may not only be dissolving, but they may also be melting. For our solar system's giants, this study concludes that the silica component is not molten at their cores, and the curve itself provides a constraint for planetary interior models, which allows more accurate predictions and, therefore, better understanding of their structure and evolution.

The structure of iron at the center of Earth was also studied in this thesis. There have been persistent arguments that the stable phase of iron at Earth's inner-core conditions is *bcc*, but these studies suffered from misinterpretation of the requirements of mechanical instability and the use of classical many-body potentials, the accuracy of which is untested in studies of the mechanical instability of *bcc* iron. In this study, different distortions were performed over the system in order to calculate mechanical stability properties, like stress and shear anisotropies and mean square displacement of the atoms. The results point toward a close-packed crystalline structure for Earth's inner core (*hcp* and/or *fcc*), rather than *bcc*. The importance of this studies lies in the fact that it indicates that iron will melt in *hcp* phase because *bcc* structure is mechanically and thermodynamically unstable at 360 GPa to the temperatures of 7000 K.

All ab initio calculations throughout this thesis were performed using VASP, a plane wave electronic structure code based on density functional theory. Part of the analyses throughout the work were performed using the classical molecular dynamics program LPMD.

This thesis has produced the following publications:

- Las Palmeras Molecular Dynamics: A flexible and modular molecular dynamics code, S. Davis, C. Loyola, F. González and J. Peralta, *Comput. Phys. Communications*: **181**, 2126–2139 (2010).
- Ab initio free energy calculations of the solubility of silica in metallic hydrogen and application to giant planet cores, F. González-Cataldo, H. Wilson and B. Militzer, *The Astrophysical Journal*: **787**, 79–84 (2014).
- Stability of Iron Crystal Structures at 0.3–0.5 TPa, B.K. Godwal, F. González-Cataldo, A. K. Verma, L. Stixrude and R. Jeanloz. *Earth and Planetary Science Letters* **409**, 299–306 (2015).
- Melting of SiO_2 at multimegabar pressures: implications for gas giants and super-Earths, F. González-Cataldo, S. Davis, G. Gutiérrez, *In manuscript.*

An additional publication, not directly related to this thesis, but derived from partial work on it (Las Palmeras Molecular Dynamics code), is the 12th chapter of the book *Molecular Dynamics - Theoretical Developments and Applications in Nanotechnology and Energy*, InTech, 2012, entitled “Inelastic Collisions and Hypervelocity Impacts at Nanoscopic Level: A Molecular Dynamics Study”.

Chapter 1

Introduction

1.1 Planet formation

Planetary systems are formed from the gravitational collapse of a region within a large molecular cloud that contains hydrogen, helium and some amounts of heavy materials, fused by previous generations of stars. As the nebula collapses, the system starts spinning and, due to the conservation of angular momentum, it begins to rotate faster and flattens into a protoplanetary disk. The center, where most of the mass is collected, becomes increasingly hotter than its surrounding environment, giving birth to the host star. Accretion takes place in the disk, where formation of dust is promoted and, as it collides, the small grains stick to one another via electromagnetic force and grow until they are massive enough to attract via gravity, forming pebbles and rocks. Gravity helps to attract more rocks and forms kilometer sized rocky bodies called planetesimals. If the mass of rocks is big enough, it attracts gas, which is the origin of gas giant planets. When the mass is not enough to accrete gas, this planetesimal turns into an Earth-like body. Beyond the frost or snow line, the distance from the host star where it is cool enough for hydrogen compounds such as water, ammonia and methane to condensate into solid ice grains, there are many more solid grains available for accretion due to the presence of ices, resulting in bigger planetesimals that can accrete gas. Therefore, it is widely believed that gas giants are formed in the outer parts of the disk, while smaller rocky planets are formed in the inner parts of the disk. However, gas giants have been found inside the frost line (it is thought that later inwards migration takes place), reaching higher temperatures and called, therefore, hot Jupiters.

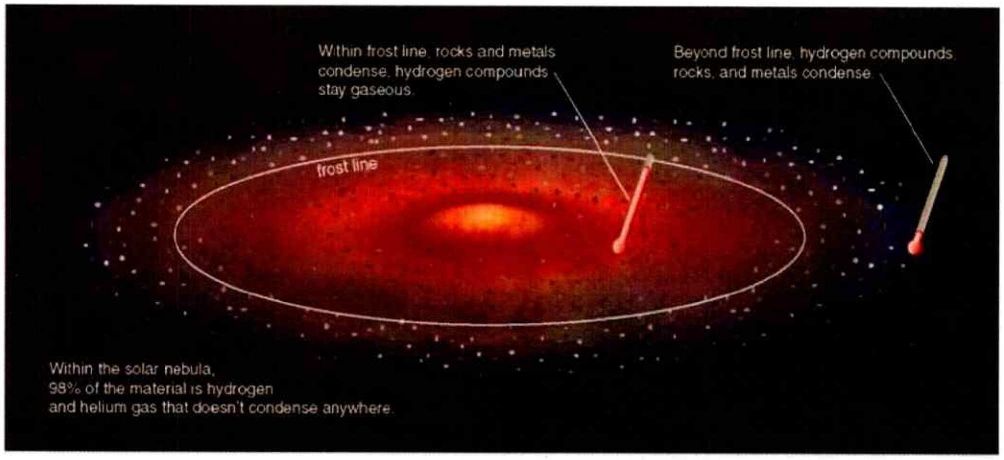

Fig. 1: Protoplanetary disk. The formation process of a planet depends on its location respect to the frost line. Image from *The Essential Cosmic Perspective*, 2005 Pearson Education.

In 1995, Michel Mayor and Didier Queloz made the first discovery of a planet outside our Solar System (exoplanet), in orbit around a Sun-like star in the constellation of Pegasus. Despite controversy over similar, earlier claims, Mayor and Queloz's discovery has withstood the test of time. Their Jupiter-sized planet completes its orbit every 4.2 days – placing it at a distance from its star, 51 Pegasi, that is much less than the Sun-Mercury distance [1]. Since those early days of exoplanet hunting, the number of such planets identified by scientists has pushed beyond a thousand [2], thanks largely to the advent of high-tech space observatories, such as the *Kepler* and CoRoT Space Telescopes. Exoplanet discoveries have been full of surprises from the outset. Nobody expected exoplanets around the remnants of a dead star (i.e. PSR 1257+12), nor Jupiter-size orbiting close to their stars (i.e. 51 Pegasi). We also know today of stellar systems packed with exoplanets (i.e. Kepler-11), around binary stars (i.e. Kepler-16), and with many potentially habitable exoplanets (rocky planets at a distance from its star where it is not too hot and not too cold for liquid water to exist on the surface). Figure 2 shows the number of planets by size for all known exoplanets and how the number increased considerably in the last report by NASA.

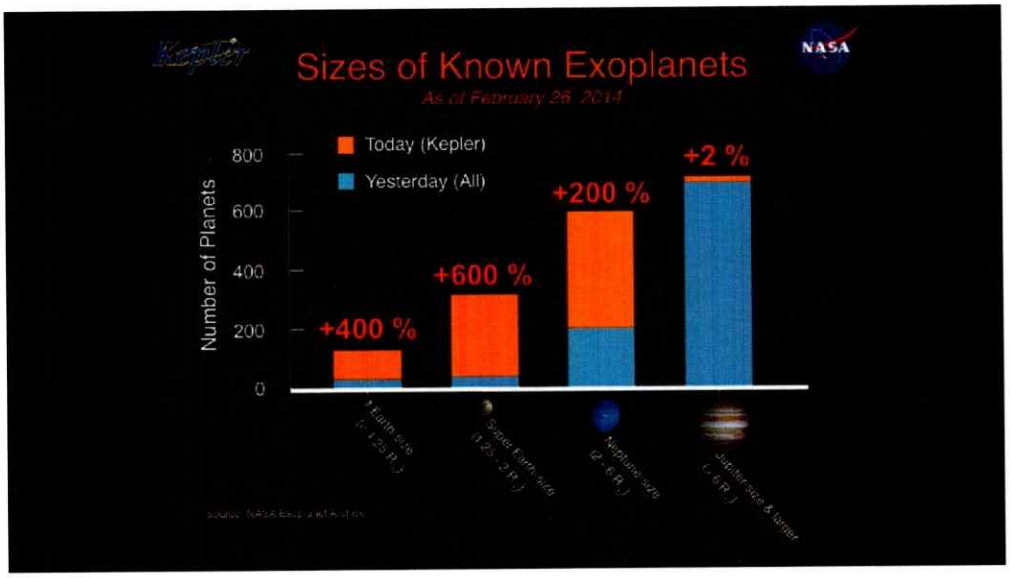

Fig. 2: Amount of confirmed exoplants until February 26th, 2014. The blue bars on the histogram represents all the exoplanets known, by size, before the *Kepler* Planet Bonanza announcement on Feb. 26th, 2014. The gold bars on the histogram represent *Kepler*'s newly-verified planets. Image from `www.nasa.gov`.

Nowadays, it is possible to know not only the mass and radius of a planet outside the solar system, which determines its mean density, but also its atmospheric composition. The thermal evolution of a planet depends on its atmospheric properties, initial state, dynamical evolution and internal composition, which is the focus of this thesis. We are entering an era of planetary characterization, with more than 1800 exoplanets already discovered, and that is the reason why it is so important to understand how can we link composition and internal structure of planets to the formation mechanism.

1.1.1 Interior structure of planets

Using probe missions, like Pioneer, Voyager and Galileo, and spectroscopic observations, scientists have been able to study the atmospheres of planets other than Earth. It has been determined that the atmospheres of Jupiter and Saturn, for example, are enriched in heavy materials like carbon, krypton, nitrogen and oxigen. Constraints on the interior structure of the giant planets of our solar system – Jupiter, Saturn, Uranus, and Neptune – are derived from knowledge of their mass M, equatorial radius a, and gravitational moments J_2, J_4, and J_6 measured by these probes (see appendix A.1). One of the reasons to study giant planets is because they shape the architecture of planetary systems, since they form very fast and have large masses. They are responsible for the excitation of small bodies in the inner protoplanetary disk and delivery of volatile material in the inner solar system. Since they have gas, they give us constraints on the composition of protoplanetary disks. The models for the structure and evolution of gas giant planets that are used in the scientific community to interpret these observations are essentially based in the concept that an atmosphere model is coupled with an internal structure model, which usually includes a layer of metallic hydrogen and an upper envelope of H and He with some amount of heavy elements (others than H and He), with a core that can be made of rock, ices and eventually, iron. Figure 3 shows the current accepted structure (roughly) of the interior of our solar system giants, and prevalent pressures and temperatures in each layer. There is still uncertainty on the structure of our giant

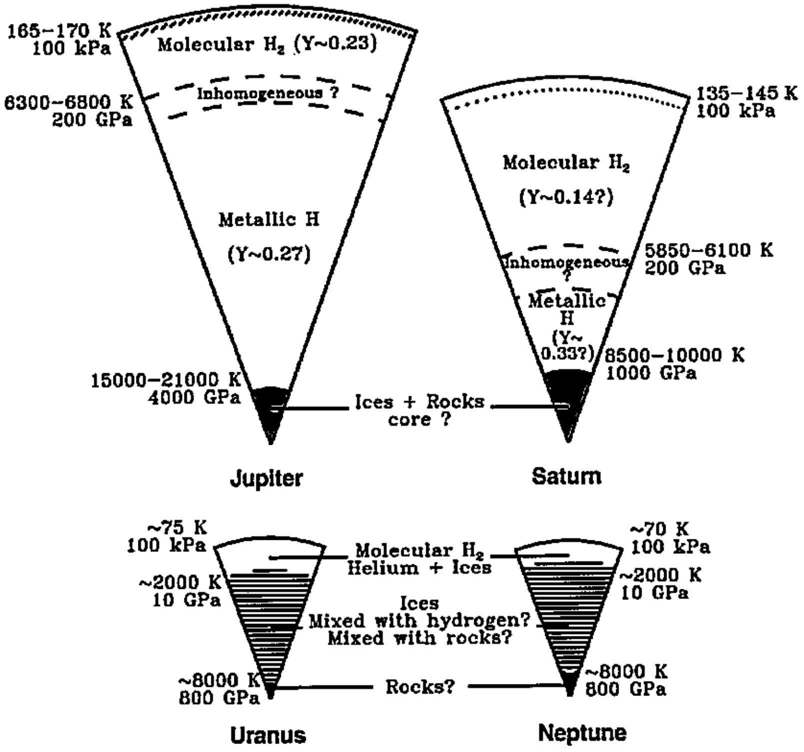

Fig. 3: Schematic representation of the interiors of Jupiter, Saturn, Uranus, and Neptune [3]. The range of temperatures is estimated using homogeneous models and including a possible radiative zone indicated by the hashed regions. Helium mass mixing ratios Y (mass of helium atoms over total mass) are indicated. The size of the central rock and ice cores of Jupiter and Saturn is very uncertain. In the case of Saturn, the inhomogeneous region may extend down all the way to the core which would imply the formation of a helium core.

planets regarding the equation of state (pressure/temperature and pressure/density relations for hydrogen–helium mixtures and heavier elements) but also regarding the transport of energy and whether the layers are homogeneous or not.

Models that explain the internal structure of these planets must take into account the constraints obtained through observation and measurements, such as the mass, radius and gravitational moments of the planet. These parameters are boundary conditions that these models, based in equations of state (EOS), must reproduce. The uncertainty on the equation of state used will be reflected in different predictions for the core mass and the amount of heavy material present in the planet. The more accurate the EOS, the more reliable the prediction about the internal composition will be.

Models usually assume that the mixtures of H and He are fully adiabatic and homogeneous, which means that the convective transport is supposed to be very efficient. More accurate models consider an inhomogeneous distribution of heavy elements, which hampers large-scale convection that turns into double-diffusive convection, yielding an inner thermal profile that departs from the traditionally assumed adiabatic interior and affecting these planets heat content and cooling history [4]. The idea that some layers in Uranus and Neptune may not be homogeneous was confirmed by Fortney *et al.* [5] at 2011. Looking at cooling models they show that Uranus is far cooler than the evolutionary models predict, which can be interpreted in terms of layers that are not homogeneous, which means that convective transport may not be as efficient as previously thought.

There has been a lot of progress in terms of structure of the planets because there has been quite a lot of progress on equations of state for hydrogen and helium, and also for heavy elements like water and silicates. It is possible to derive first-principles equations of state and this new models change the picture. For example, Jupiter has always been predicted to have a relatively small rocky core (between zero and seven Earth masses [6, 7]), which is surprising because similar theories predicted between

10 and 25 Earth masses for the core in Saturn [7]. The small core hypothesis for Jupiter has been challenged in a paper by Militzer *et al.* [8], who used first-principles computer simulations of hydrogen–helium mixtures in a two-layer model to compute the EOS in the interior of Jupiter. This work predicts a large core of 14–18 Earth masses for Jupiter, which is in line with estimates for Saturn and suggests that both planets may have formed by core-accretion. The paper further predicts small fraction of planetary ices in Jupiter's envelope suggesting that the ices were incorporated into the core during formation rather than accreted along with the gas envelope. Jupiter is predicted to have an isentropic and fully convective envelope that is of constant chemical composition. In order to match the observed gravitational moment J_4, the authors suggest that Jupiter may not rotate as a solid body and predicted the existence of deep winds in the interior leading to differential rotation on cylinders. This result has been recently contradicted by recent calculations by Nettelman *et al.* [9], who have also built models based on first-principles equations of state for hydrogen, helium and water, but using a three-layer model: core of rocks/ice + inner isentropic envelope. They confirm the previous results of a small core, with a mass ranging from 0–8 Earth masses. Interestingly, they conclude that the difference between both predictions does not depend on the amount of layers used.

This example ilustrates that there is progress going on, in particular, in the development of first-principles equations of state. For rocky planets, the EOS of different rocks is also important to build internal structure models (see appendix A.2), which rely on the knowledge about the properties of materials [10–13]. It is known that a rocky planet that has accumulated too much material can shrink due to gravity, increasing the pressure inside and altering the inner structure. This is a challenge for experiments and simulations, since more studies at high pressure are required in order to understand how materials behave at the interior of these planets. These models and our understanding of planetary evolution will be more accurate to the extent that we can characterize the materials relevant to planetry composition, which requires the calculation of different equations of state.

The progress is every day taking place at a higher base because of the development of high pressure experiments, using anvil cells and laser heating and shockwaves, which can test the validity of these equations in the laboratory.

1.2 Quantum mechanics explains matter

In the early 20^{th} century, a new theory, called *quantum mechanics*, emerged from experiments that contradicted Newton's theory, *classical mechanics*, which was a successful, precise mathematical model to describe reality for almost 300 years. The development of quantum mechanics is one of the most profound scientific advances of the twentieth century, and also the repeated experimental observations that confirmed that this theory of matter describes, with astonishing accuracy, the universe in which we live. This new theory provided a mathematical framework that correctly explained properties of matter at the atomic level, the dual particle-like and wave-like behavior and interactions of energy and matter. Quantum theory has prevailed as a rigorously tested and robust mathematical description of the behavior of microscopic, atomic matter. There is no doubt that it is a theory that allows scientists to accurately predict and understand properties of materials and has played a significant role in the development of many modern technologies.

Physicists, geophysicists and mineralogists need to understand and predict the properties of solids and liquids at normal and at high pressures and temperatures. For example, they need to know the equilibrium structure, equation of state, phase transitions, and vibrational properties of solids, and the interatomic or intermolecular interaction needed for a molecular dynamics study of liquids. This information, in sufficient detail, is not always available from experiment. Quantum Mechanics allow us to predict such properties. It accurately describes the structure of atoms, bonding of atoms in molecules and solids, behavior of electrons and, in fact, can describe all properties of matter. The main aim of this thesis is to obtain properties of matter, regarding planetary interiors, by means of solving the equations of quantum mechanics.

1.3 Numerical quantum-mechanics simulations

The equation that rules the behavior of matter in quantum physics is the Schrödinger equation,

$$\check{\mathbf{H}}\Psi = i\hbar\frac{\partial\Psi}{\partial t}, \tag{1.1}$$

which, in its time-independent form reads

$$\check{\mathbf{H}}\Psi = E\Psi. \tag{1.2}$$

This equation relates the properties of a system of particles, described by a wave function Ψ, to its energy, E, through the system's Hamiltonian $\check{\mathbf{H}}$. In practice, these equations are very difficult to solve, and analytic solutions are available only for noninteracting electron systems. Interacting electrons have a *correlation energy*, because of the Coulomb interaction, and a quantum mechanical *exchange energy*, that arises from the Pauli's exclusion principle. The Coulomb interaction between electrons leads to a term in the Hamiltonian that cannot be separated and, hence, the wave function cannot be written as an analytically solvable product of independent functions. This fact rules out any simple approach to a highly accurate solution.

However, the development of powerful computers has allowed scientists to build programs that can are able to find numerical solutions to physical problems, in particular, to the Schrödinger equation. A number of numerical techniques have been developed offering various levels of treatment of the troublesome exchange and correlation interactions of electrons. These are sometimes referred to as *electronic structure calculations.* These accurate electronic structure methods are classified as first-principles or ab initio, which means they are numerical simulations of Schrödinger's equation that have no experimental input or adjustable parameters that require previous knowledge of the system properties.

Despite of the availability of this numerical approach, exact, unapproximated first-principles simulations are still too difficult for all but the smallest systems. Although ab initio methods are technically able to exactly compute properties of materials, the computational time required for such a calculation often scales exponentially with system size, taking longer than the lifetime of the researcher. The calculations are said to be computationally expensive. In general, a method trades off accuracy for the ability to study larger system sizes.

Consequently, a highly active area of computational physics research involves developing approximations that speed up ab initio methods, but only negligibly reduce the accuracy and predictive power. It is the electron interactions in materials that are most computationally cumbersome and require approximations. One of the most popular and successful ab initio methods is density functional theory (DFT) [14], described in the next chapter, which is an exact theory.

In this thesis, we will make extensive use of DFT to solve the Schrödinger's equation of different systems, which will allow us to obtain their properties.

1.4 Organization and Thesis accomplishments

The research presented in this thesis uses knowledge and tools developed in various scientific communities. Chapter 2 introduces the electronic structure models, and how to perform molecular dynamics within the density functional theory which allows to understand the foundation for the research in this thesis. The first sections of chapter 2 give a brief description of the many-body problem, and the following sections describe the Hartree-Fock and Density Functional Theory approximations, two of the most common approches to solve the many-body Schrödinger equation. In chapter 3, a thermodynamical approach to compute solubility is discussed, which will be the basis of the study in the following chapter. The first sections correspond to the definition of Gibbs free energy of solvation, which is coupled with the free energy of mixing correction, while in the last section the thermodynamic integration technique is described, which is a fundamental procedure to compute Gibbs free energy in molecular dynamics simulations.

This thesis is motivated by the increasing understanding in planetary formation and evolution, and aims to connect what we are able to know about matter from a condensed matter point of view with the bulk behavior of planets. Thus, chapter 4 turns to focus on the calculation of the solubility of silica into metallic hydrogen, a phenomenon that has not been previouly been analyzed in the study of the interiors on gas giants, like Jupiter. We discuss the consequences of this study on the evolution and formation of gas giant planets.

The majority of new and original research within this thesis is presented in chapters 4, 5 and 6. These chapters involve the application of condensed matter techniques to evaluate properties of materials concerning to planetary interiors. In chapter 4 the possibility of solvation of silica into metallic hydrogen is analyzed. Thereafter, in chapter 5, the attention is focussed on the melting behavior of silica, which becomes relevant for understanding rocky planets, like super-Earths, as well as the core of gas giants. In this chapter, calculations of the melting temperature of silica in the multimegabar pressure range, where no previous data existed, are presented. The content of chapters 6 correspond to a study related to the Earth's inner core, in which the stability of the *bcc* phase of iron is analyzed in detail from many points of view. The chapter shows how the *bcc* structure is located in a saddle point of the energy surface, and shows how the addition of deformations at high temperature indicate that this structure cannot be stable at the Earth's core.

Some appendices follow chapter 6, providing details about astrophysical models for understanding the internal structure of planets, atomistic method for determining crystal structures, and additional details about solubility and tetragonal strains.

Chapter 2

Ab Initio Simulations

Computer simulations have become a powerful tool to solve complicated equations that model the behavior of physical systems. In particular, solving the Schrödinger equation for complicated atomic systems was not feasible until computational techniques were developed to solve it. In this chapter we will describe the principal methods for solving the Schrödinger equation, being the density functional theory the method chosen in this thesis to perform all calculations.

2.1 The Many Body Problem

If we have M atomic nuclei at positions $\mathbf{R}_1, \ldots, \mathbf{R}_M$, then we can can express the ground-state energy, E, as a function of the positions of these nuclei, $E(\mathbf{R}_1, \ldots, \mathbf{R}_M)$. This function is known as the *adiabatic potential energy surface* of the atoms. The situation we are interested in where multiple electrons (N) are interacting with multiple nuclei (M) is described by the following Hamiltonian:

$$\begin{aligned}\breve{\mathbf{H}} = &-\sum_{I=1}^{M} \frac{\hbar^2}{2M_I}\nabla_I^2 - \sum_{i=1}^{N} \frac{\hbar^2}{2m}\nabla_i^2 + \frac{e^2}{2}\sum_{I=1}^{M}\sum_{J\neq I}^{M} \frac{Z_I Z_J}{\|\mathbf{R}_I - \mathbf{R}_J\|} \\ &+ \frac{e^2}{2}\sum_{i=1}^{N}\sum_{j\neq i}^{N} \frac{1}{\|\mathbf{r}_i - \mathbf{r}_j\|} - \sum_{I=1}^{M}\sum_{i=1}^{N} \frac{e^2 Z_I}{\|\mathbf{R}_I - \mathbf{r}_i\|}. \end{aligned} \tag{2.1}$$

Here, M_I and Z_I are the mass and atomic number of the nucleus I , m is the electron mass and $\hbar$ is the Plank's constant. The terms in this equation define, in order, the kinetic energy of the nuclei, the kinetic energy of the electrons, the interaction energy between the different nuclei, the Coulomb interaction energy between the different electrons, and the interaction energy between each electron and the collection of atomic nuclei. Using this Hamiltonian in the Schrödinger equation

$$\check{\mathrm{H}}\Psi(\mathbf{R},\mathbf{r}) = E\Psi(\mathbf{R},\mathbf{r}), \tag{2.2}$$

results in an $3(M+N)$ – dimensional eigenvalue problem, where $\mathbf{R} = (\mathbf{R}_1, \ldots, \mathbf{R}_M)$ is the collective coordinate for the M nuclei, and $\mathbf{r} = (\mathbf{r}_1, \ldots, \mathbf{r}_N)$ the collective coordinate for all the N electrons. In practice, this problem is almost impossible to treat within a full quantum mechanical framework. Only in a few cases, such as hydrogenoid atoms or the H_2^+ molecule, a complete analytic solution is available. Exact numerical solutions are also limited to a few cases, mostly atoms and very small molecules. There are several features that contribute to this difficuly, but the most important is that this is a multi-component many-body system, and the two-body nature of the Coulomb interaction makes the above Schrödinger equation not separable.

Most materials of interest contain a large number of interacting protons and electrons, which means that approximations must be made in order to reduce the complexity of the problem and be able to find the wave-function and energy. Once the wave-function and energy is known for a system, many properties may be calculated. However, the various approximations made in a particular method have significant impact on the accuracy of the predictions. The following sections discuss two principal approaches to approximating the solution of the Schrödinger equation: Hartree–Fock Theory (HF), an orbital based method that approximates the wave function for the electrons as a Slater determinant of single particle orbitals, and Density Functional Theory (DFT), which is based fundamentally on the charge density rather than a many-body wave-function.

Born–Oppenheimer Approximation A first approach to reduce the complexity of the problem above is to consider that the nuclei are much more massive than electrons (1800 times heavier), which means that electrons move much faster. In this spirit Born and Oppenheimer (1927) proposed a scheme for separating the motion of the nuclei from that of the electrons. In this scheme, nuclei positions are considered a constant of motion for the system and a the electrons can be thought of as instantaneously following the motion of the nuclei, while remaining always in the same stationary state of the electronic Hamiltonian. A solution to (2.2) is then proposed in the form

$$\Psi(\mathbf{R},\mathbf{r},t) = \sum_n \Theta_n(\mathbf{R},t)\psi_n(\mathbf{R},\mathbf{r}), \tag{2.3}$$

where $\Theta_n(\mathbf{R},t)$ are the wave functions describing the evolution of the nuclear subsystem in each one of the adiabatic electronic eigenstates $\psi_n(\mathbf{R},\mathbf{r})$. These satisfy the time-independent Schrödinger equation

$$\check{\mathbf{h}}_e\psi_n(\mathbf{R},\mathbf{r}) = E_n(\mathbf{R})\psi_n(\mathbf{R},\mathbf{r}), \tag{2.4}$$

where

$$\check{\mathbf{h}}_e = -\sum_{i=1}^{N}\frac{\hbar^2}{2m}\nabla_i^2 + \frac{e^2}{2}\sum_{i=1}^{N}\sum_{j\neq i}^{N}\frac{1}{\|\mathbf{r}_i-\mathbf{r}_j\|} - \sum_{I=1}^{M}\sum_{i=1}^{N}\frac{e^2 Z_I}{\|\mathbf{R}_I-\mathbf{r}_i\|} \tag{2.5}$$

is the electronic Hamiltonian. Although the complexity of the problem has been reduced to a 3N–dimensional problem, the equation (2.4) is still difficult to solve, with no analytic solution for more than one electron, since the second term in (2.5) makes impossible to separate the Hamiltonian in a sum single-particle Hamiltonians. This leads to a simple solution, which is that ψ is the product of individual wave functions, $\psi = \psi_1\psi_2, \ldots, \psi_N$. However, the Born–Oppenheimer approximation is used as a base to build the mean field theory, which will be described in the following section.

2.2 Mean Field Theory

2.2.1 Hartree Approximation: No Exchange, Averaged Correlation

Separating the nuclei from the electrons through the Born–Oppenheimer approximation is the first step in solving the many-body problem. The next step is how to deal with the electron-electron interaction. The first approach may be considered to be the one proposed by Hartree (1928), in the very beginnings of the age of quantum mechanics. The basic assumption is that the many-electron wave function can be written as a simple product of one-electron orbitals,

$$\Psi(\mathbf{r}) = \prod_{i=1}^{N} \psi_i(\mathbf{r}_i), \tag{2.6}$$

which is exactly what would happen if the electrons were noninteracting. While this is not realistic enough for general electronic systems, it is included here to ilustrate the basic features of the one-electron approches.

In order to break down the Schrödinger equation into many simpler one-electron equations, Hartree proposed that the electrostatic field felt by an electron in an atom was due to the central potential of the nuclei together with the field created by the other electrons. That is, each electron at a position $\mathbf{r}_i$ experiences a mean-field electron-generated potential

$$V_H(\mathbf{r}_i) = e^2 \int \frac{n(\mathbf{r}')}{\|\mathbf{r}_i - \mathbf{r}'\|} \, d^3 r', \tag{2.7}$$

usually called the Hartree potential, and the electron-nucleus interaction potential,

$$V(\mathbf{R}, \mathbf{r}_i) = -\sum_{I=1}^{M} \frac{e^2 Z_I}{\|\mathbf{R}_I - \mathbf{r}_i\|}, \tag{2.8}$$

whose sum over all N electrons gives rise to the third term in (2.5). The electronic density $n(\mathbf{r})$ that appears in the Hartree potential is given by

$$n(\mathbf{r}) = 2\sum_i \psi_i^*(\mathbf{r})\psi_i(\mathbf{r}) = 2\sum_i |\psi_i(\mathbf{r})|^2. \tag{2.9}$$

This summation goes over all the individual electron wave functions that are occupied by electrons, so the term inside the summation is the probability that an electron in individual wave function $\psi_i(\mathbf{r})$ is located at position $\mathbf{r}$. The factor 2 comes from the Pauli exclusion principle, which allows 2 electrons in the same state with opposite spin.

Employing the variational principle, Slater (1928) was able to demonstrate that, in order to find a solution Ψ for the Hamiltonian in (2.5), which can be rewritten as

$$\check{\mathbf{h}}_e(\mathbf{R}, \mathbf{r}) = \sum_{i=1}^{N} \check{\mathbf{h}}_i + \frac{e^2}{2} \sum_{i=1}^{N} \sum_{j \neq i}^{N} \frac{1}{\|\mathbf{r}_i - \mathbf{r}_j\|}, \tag{2.10}$$

where

$$\check{\mathbf{h}}_i = -\frac{\hbar^2}{2m} \nabla_{\mathbf{r}_i}^2 + V(\mathbf{R}, \mathbf{r}_i), \tag{2.11}$$

the orbitals ψ_i in (2.6) must satisfy, as originally proposed by Hartree,

$$\left(-\frac{\hbar^2}{2m} \nabla^2 + V(\mathbf{R}, \mathbf{r}) + \int \frac{\sum_{j \neq i}^{N} |\psi_j(\mathbf{r}')|^2}{\|\mathbf{r} - \mathbf{r}'\|} \, d^3 r' \right) \psi_i(\mathbf{r}) = \varepsilon_i \psi_i(\mathbf{r}). \tag{2.12}$$

The set of N one-particle equations in (2.12) are known as the *Hartree equations.*

2.2.2 Hartree–Fock Approximation: Explicit Exchange, Averaged Correlation

The Hartree approximation treats the electrons as distinguishable particles. Electrons, however, are indistinguishable spin-1/2 particles (fermions) and Pauli's exclusion principle states that two fermions cannot occupy the same quantum state because the many-fermion wave function has to be antisymmetric upon particle exchange. This means that, if two electrons are exchanged, the wave function must change sign. For two electrons in the same quantum state the only antisymmetric wave function is the null wave function. The Hartree approximation does not contain this feature and, as a consequence, the description of the electronic component is incomplete.

Introducing Pauli's principle can be easily done proposing an antisymmetrized many-electron wave function in the form of a Slater determinant:

$$\Psi(\mathbf{x}_1, \mathbf{x}_2, \ldots, \mathbf{x}_N) = \frac{1}{N!} \begin{vmatrix} \psi_1(1) & \psi_2(1) & \cdots & \psi_N(1) \\ \psi_1(2) & \psi_2(2) & \cdots & \psi_N(2) \\ \vdots & \vdots & \ddots & \vdots \\ \psi_1(N) & \psi_2(N) & \cdots & \psi_N(N) \end{vmatrix} \tag{2.13}$$

where $\psi_i(j)$ refers to the ith one-electron spin orbital, i.e. composed of spatial and spin components, and (j) indicates the spacial and spin coordinates of electron j condensed in a single variable $\mathbf{x}_j = (\mathbf{r}_j, \sigma_j)$. This determinant ensures that the wave function changes sign when exchanging the coordinates of two of the electrons. Although not yet completely general, this wave functions introduces particle exchange in an exact manner.

Applying the variational principle to the Hamiltonian with respect to variations in the one-electron wave functions, results in the one-electron, Hartree–Fock equations:

$$\left(-\frac{\hbar^2}{2m}\nabla^2 + V(\mathbf{R},\mathbf{r}) + V_H(\mathbf{r})\right)\psi_i(\mathbf{r}) - \sum_j^N \delta_{\sigma_i\sigma_j}\int d^3r'\,\frac{\psi_j^*(\mathbf{r}')\psi_i(\mathbf{r}')}{\|\mathbf{r}-\mathbf{r}'\|}\psi_j(\mathbf{r}) = \varepsilon_i\psi_i(\mathbf{r}), \tag{2.14}$$

where $V(\mathbf{R},\mathbf{r})$ and $V_H(\mathbf{r})$ are the electron-nucleus interaction and the Hartree potential previously defined in (2.7) and (2.8), while the last term is called *exchange term*. As written, the Hartree term includes an unphysical self-interaction of electrons. This term is cancelled in the exchange term. The exchange term results from our inclusion of the Pauli principle and the assumed determinantal form of the wavefunction. The effect of exchange is for electrons of like-spin to avoid each other. Each electron of a given spin is consequently surrounded by an "exchange hole", a small volume around the electron which like-spin electron avoid.

2.3 Density Functional Theory

Density functional theory is a phenomenally successful approach to finding solutions to the fundamental equation that describes the quantum behavior of atoms and molecules, the Schrödinger equation, in settings of practical value [14]. This approach has rapidly grown from being a specialized art practiced by a small number of physicists and chemists at the cutting edge of quantum mechanical theory to a tool that is used regularly by large numbers of researchers in chemistry, physics, materials science, chemical engineering, geology, and other disciplines. DFT is currently one of the most successful and popular electronic methods available for computing properties of real solids. It allows for a great simplification in solving the many-body problem based on functionals of the electron density. The theory, while based on a mean-field approach, is formally exact and, as a result, some consider DFT as its own class of method. Density Functional Theory will be the scheme to perform most of the calculations in this thesis, so we will give a more detailed description.

The entire field of density functional theory rests on two fundamental mathematical theorems proved by Kohn and Hohenberg [15] and the derivation of a set of equations by Kohn and Sham [16] in the mid-1960s. The first theorem, proved by Hohenberg and Kohn, states that *The ground-state energy from Schrödinger's equation is a unique functional of the electron density.* Then, the energy E of the system can be expressed as a functional $E\left[n(\mathbf{r})\right]$, where $n(\mathbf{r})$ is the electron density function defined in (2.9). This is why this field is known as density functional theory.

Unfortunately, although the first Hohenberg–Kohn theorem rigorously proves that a functional of the electron density exists that can be used to solve the Schrödinger equation, the theorem says nothing about what the functional actually is. The second Hohenberg–Kohn theorem defines an important property of the functional: *The electron density that minimizes the energy of the overall functional is the true electron density corresponding to the full solution of the Schrödinger equation.* If the "true" functional form were known, then we could vary the electron density until the energy from the functional is minimized, giving us a prescription for finding the relevant electron density. This variational principle is used in practice with approximate forms of the functional.

A useful way to write down the functional described by the Hohenberg–Kohn theorem is in terms of the single-electron wave functions, $\psi_n(\mathbf{r})$. These functions collectively define the electron density through (2.9). The energy functional can be written as

$$E\left[n(\mathbf{r})\right] = E_{\text{known}}\left[n(\mathbf{r})\right] + E_{\text{XC}}\left[n(\mathbf{r})\right], \tag{2.15}$$

where we have split the functional into a collection of terms we can write down in a simple analytical form, $E_{\text{known}}[n(\mathbf{r})]$, and everything else, E_{XC}. The "known" terms include three contributions:

$$E_{\text{known}}[n(\mathbf{r})] = T[n(\mathbf{r})] + V_H[n(\mathbf{r})] + \int V(\mathbf{r})n(\mathbf{r})\, d^3r, \tag{2.16}$$

which correspond to the electrons kinetic energy, defined by

$$T[n(\mathbf{r})] = -\frac{\hbar^2}{2m}\sum_{i=1}^{N}\int \psi_i^* \nabla_i^2 \psi_i\, d^3r, \tag{2.17}$$

the Coulomb interactions between pairs of electrons (Hartree potential)

$$V_H[n(\mathbf{r})] = \frac{e^2}{2}\iint \frac{n(\mathbf{r})n(\mathbf{r}')}{\|\mathbf{r}-\mathbf{r}'\|}\, d^3r\, d^3r', \tag{2.18}$$

and the Coulomb interactions between the electrons and the nuclei. The other term in the complete energy functional, $E_{\text{XC}}[n(\mathbf{r})]$, is the exchange-correlation functional, and it is defined to include all the quantum mechanical effects that are not included in the "known" terms. Kohn and Sham showed that the task of finding the right electron density could be done by means of solving a set of single-electron equations, now known as Kohn–Sham equations:

$$\left[-\frac{\hbar^2}{2m}\nabla^2 + V(\mathbf{r}) + V_H(\mathbf{r}) + V_{\text{XC}}(\mathbf{r})\right]\psi_i(\mathbf{r}) = \varepsilon_i \psi_i(\mathbf{r}), \tag{2.19}$$

In these Schrödinger-like equations the potential energy operators V_H and V, defined in (2.7) and (2.8), appear. They include a self-interaction contribution in the Hartree potential V_H, because the electron we are describing in the Kohn–Sham equation is also part of the total electron density, so part of V_H involves a Coulomb interaction between the electron and itself. The self-interaction is unphysical, and the correction for it is one of several effects that are lumped together into the final potential in the Kohn–Sham equations, V_{XC}, which defines exchange and correlation contributions to the single-electron equations. V_{XC} can formally be defined as a "functional derivative" of the exchange-correlation energy:

$$V_{\mathrm{XC}}(\mathbf{r}) = \frac{\delta E_{\mathrm{XC}}(\mathbf{r})}{\delta n(\mathbf{r})}, \tag{2.20}$$

but true form of the exchange-correlation functional whose existence is guaranteed by the Hohenberg–Kohn theorem is simply not known. Furthermore, to solve the Kohn–Sham equations, we also need to define the Hartree potential, and to define the Hartree potential we need to know the electron density. But to find the electron density, we must know the single-electron wave functions, and to know these wave functions we must solve the Kohn–Sham equations. To break this circle, the problem is usually treated in an iterative way as outlined in the following algorithm:

1. Define an initial, trial electron density, $n(\mathbf{r})$.
2. Solve the Kohn–Sham equations defined using the trial electron density to find the single-particle wave functions, $\psi_i(\mathbf{r})$.
3. Calculate the electron density defined by the Kohn–Sham single-particle wave functions from step 2, $n_{\mathrm{KS}}(\mathbf{r}) = 2\sum_i \psi_i^*(\mathbf{r})\psi_i(\mathbf{r})$.
4. Compare the calculated electron density, $n_{\mathrm{KS}}(\mathbf{r})$, with the electron density used in solving the Kohn–Sham equations, $n(\mathbf{r})$. If the two densities are the same, then this is the ground-state electron density, and it can be used to compute the total energy. If the two densities are different, then the trial electron density must be updated in some way. Once this is done, the process begins again from step 2.

Prescriptions to choose the new electron density $n_{\mathrm{KS}}(\mathbf{r})$ in order to be closer to the actual electron density $n(\mathbf{r})$, how close do the two electron densities have to be before we consider them to be the same, and others details like these are implemented in different manners in DFT-based softwares. We will now briefly discuss a part of the theory which we must solved before getting into the algorithm: the exchange-correlation functional.

2.3.1 Local Density Approximation

As we mentioned, the true form of the exchange-correlation functional, whose existence is guaranteed by the Hohenberg–Kohn theorem, is simply not known. But there is one case where this functional can be derived exactly: the uniform electron gas. For the electron gas, the electron density is constant at all points in space; that is, $n(\mathbf{r}) = \text{constant}$. This situation may appear to be of limited value in any real material since it is variations in electron density that define chemical bonds and generally make materials interesting. But the uniform electron gas provides a practical way to actually use the Kohn–Sham equations. To do this, we set the exchange-correlation potential at each position to be the known exchange-correlation potential from the uniform electron gas at the electron density observed at that position:

$$V_{\mathrm{XC}}(\mathbf{r}) = V_{\mathrm{XC}}^{\text{electron gas}}\left[n(\mathbf{r})\right]. \tag{2.21}$$

This approximation uses only the local density to define the approximate exchange-correlation functional, so it is called the *local density approximation* (LDA). The LDA gives us a way to completely define the Kohn–Sham equations, but it is crucial to remember that the results from these equations do not exactly solve the true Schrödinger equation because we are not using the true exchange-correlation functional.

Although LDA leads to some known errors, like the underestimation in Band gap values, overestimated binding energies and bulk moduli and underestimated volumes of 3d solids; LDA has enjoyed considerable success and is still being widely used.

2.3.2 Generalized Gradient Approximation

The best known class of functional after the LDA uses information about the local electron density and the local gradient in the electron density; this approach defines a *generalized gradient approximation* (GGA). It is tempting to think that because the GGA includes more physical information than the LDA it must be more accurate. Unfortunately, this is not always correct.

Because there are many ways in which information from the gradient of the electron density can be included in a GGA functional, there are a large number of distinct GGA functionals. Two of the most widely used functionals in calculations involving solids are the Perdew–Wang functional (PW91) and the Perdew–Burke–Ernzerhof functional (PBE). Each of these functionals are GGA functionals, and dozens of other GGA functionals, like the Minnesota Functionals, have been developed and used, particularly for calculations with isolated molecules. Because different functionals will give somewhat different results for any particular configuration of atoms, it is necessary to specify what functional was used in any particular calculation rather than simple referring to "a DFT calculation".

2.3.3 Reciprocal space and k-points sampling

Another important issue regarding electronic structure calculations, in particular DFT, is the k-points sampling, which is fundamental to get reliable results. It is not our aim here to give here a complete description on the concepts related to the reciprocal space (the mathematical space of all k-points), since several standard solid-state physics texts cover this subject, but we will review the basic concepts.

When DFT is used to study periodic systems, which represent bulk materials, a primitive cell with a basis of atoms is chosen. This cell, characterized by cell vectors usually called **a**, **b** and **c**, is enough to represent the whole crystal (peridic, infinite systems) through replications along the cell vectors. The linear combinations of these vectors through integer numbers defines the *lattice points*, the mathematical places in which the basis of atoms are placed to form the crystal. The collection of all lattice points is known as *real lattice* (or just *lattice*), and any point between the lattice points, the *real space.* In similar fashion, the *reciprocal lattice,* built from *reciprocal vectors,* is the collection of all *reciprocal lattice points.* Any point between reciprocal lattice points (lattice points included) are regarded as k-points. The name comes after the Bloch's theorem, which arises from the periodicity of the system. This theorem states that the electronic wave functions must satisfy

$$\psi_{\mathbf{k}}(\mathbf{r}) = \exp(i\mathbf{k} \cdot \mathbf{r}) u_{\mathbf{k}}(\mathbf{r}), \tag{2.22}$$

where $u_{\mathbf{k}}(\mathbf{r})$ is periodic function evaluated in a vector of the real space with the same periodicity as the primitive cell, and $\mathbf{k}$ is a vector that differentiates the different wave functions, with units of inverse length.

It turns out that many parts of the mathematical problems posed by DFT are much more convenient to solve in terms of $\mathbf{k}$ than they are to solve in terms of $\mathbf{r}$. Because the functions $\exp(i\mathbf{k} \cdot \mathbf{r})$ are called plane waves, calculations based on this idea are frequently referred to as plane-wave calculations. The space of vectors $\mathbf{r}$ corresponds to the real space, and the space of $\mathbf{k}$, to the reciprocal space (or simply k-space).

The reciprocal vectors, defined by

$$\mathbf{b}_1 = 2\pi \frac{\mathbf{b} \times \mathbf{c}}{\mathbf{a} \cdot (\mathbf{b} \times \mathbf{c})}, \quad \mathbf{b}_2 = 2\pi \frac{\mathbf{c} \times \mathbf{a}}{\mathbf{a} \cdot (\mathbf{b} \times \mathbf{c})}, \quad \mathbf{b}_3 = 2\pi \frac{\mathbf{a} \times \mathbf{b}}{\mathbf{a} \cdot (\mathbf{b} \times \mathbf{c})}, \tag{2.23}$$

define a primitive cell in the reciprocal space, which has many properties and is known as *Brillouin zone* (BZ). Several points in the Brillouin zone with special significance are given individual names. The most important of these is the point where $\mathbf{k} = \mathbf{0}$; this location in k-space is called the Γ point. The volume of the Brillouin zone and the volume of the primitive cell in real space are related by

$$V_{\mathrm{BZ}} = \frac{(2\pi)^3}{V_{\mathrm{cell}}}, \tag{2.24}$$

which means that the bigger the cell in real space, the smaller the Brillouin zone.

In a practical DFT calculation, a great deal of the work reduces to evaluating integrals of the form

$$g = \frac{V_{\mathrm{cell}}}{(2\pi)^3} \int_{\mathrm{BZ}} g(\mathbf{k})\, d\mathbf{k}, \tag{2.25}$$

where g is the property to be calculated. The key features of this integral are that it is defined in reciprocal space and that it integrates only over the possible values of $\mathbf{k}$ in the Brillouin zone. This integrals are evaluated through numerical methods, which allow to replace the integral by a finite sum of the form

$$\sum_{j=1}^{n} c_j g(\mathbf{k}_j). \tag{2.26}$$

The problem of calculating the integral is therefore simplified to evaluate g only in certain k-points and sum over them. To reduce computational time, the evaluation of these integrals must be efficient, and doing so has been studied very carefully through time. Many methods are available nowadays, and the Monkhorst and Pack scheme, developed in 1976, is one of the most used methods. Another famous and useful one, is the tetrahedron method, specially suited to deal with metals, since the Fermi–Dirac occupation function goes abruptly to zero at the fermi energy, which makes the integral particulary difficult to solve for this cases. Through this thesis, we will use these methods depending of the type of material analyzed.

As we mentioned, the volume of the Brillouin is inversely proportional to the volume of the real space cell. This means that big cells will have a small Brillouin zone, and a smaller number of k-points will be needed to evaluate the integrals. Although a thumb rule is that the Γ point is enough to sample the Brillouin zone of supercells (cells obtained from finite replications of primitive cells), this is not always guaranteed, and k-points convergence tests (increasing the number of k-points until the energies do not vary) are always recomended before performing a calculation.

2.3.4 Molecular Dynamics

The atoms of materials are in constant motion, and this is what we know as temperature. The most common approach to study the effect of temperature on the properties of a material at atomic level is known as *Molecular Dynamics* (MD), a technique that tracks the position of the atoms over time and allows for the characterization of material properties, like radial distribution of atoms, diffusion, melting, study of amorphous phases, atoms coordination and characterization of atomic neighborhood among many others.

Many of the relevant thermodynamic properties of a material can be obtained from MD through statistical mechanics, which relates the positions and velocities of atoms, calculated by MD, to macoscopic properties like energy, temperature and pressure. We will now give a brief description of how positions and velocities are obtained during the simulation and how properties are calculated.

Microcanonical Ensemble

In classical mechanics, a system of M atoms at positions $\mathbf{R}_I$ and with velocities $\mathbf{V}_I$ has a kinetic energy

$$K = \frac{1}{2}\sum_{I=1}^{M} M_I \mathbf{V}_I^2, \tag{2.27}$$

where M_I is the mass of the atom associated with the Ith coordinate, and an interaction energy given by a certain potential energy,

$$U = U(\mathbf{R}_1, \ldots, \mathbf{R}_M). \tag{2.28}$$

In this classical mechanics approach, Newton's laws of motion apply to these atoms. That is,

$$\mathbf{F}_I = M_I \frac{d\mathbf{V}_I}{dt}, \tag{2.29}$$

where

$$\mathbf{F}_I = -\nabla_{\mathbf{R}_I} U(\mathbf{R}_1, \ldots, \mathbf{R}_M) \tag{2.30}$$

is the force applied to the Ith atom. These relationships define a set of $6M$ coupled first-order differential equations

$$\frac{d\mathbf{R}_I}{dt} = \mathbf{V}_I \tag{2.31}$$

$$\frac{d\mathbf{V}_I}{dt} = -\frac{1}{M_I}\frac{\partial U(\mathbf{R}_1, \ldots, \mathbf{R}_M)}{\partial \mathbf{R}_I}, \tag{2.32}$$

which can be solved using numerical integration algorithms, like Verlet, Beeman and others. These equations conserve the total energy $E = K + U$ and thus define the framework of the microcanonical ensemble.

The temperature is defined as the ensemble average of the kinetic energy,

$$\langle K \rangle = \left\langle \frac{1}{2}\sum_{I=1}^{M} M_I \mathbf{V}_I^2 \right\rangle = \frac{3}{2} N k_B T, \tag{2.33}$$

but in practice, the ergodic hypothesis is used and this ensemble average is replaced by a time average, provided the simulation time is enough to let the property converge. Removing the brackets gives a definition of *instantaneous temperature*,

$$T_{MD} \equiv \frac{1}{3Nk_B} \sum_{I=1}^{M} M_I \mathbf{V}_I^2, \tag{2.34}$$

which is not physical, but very useful to check its convergence to a mean value, which is the actual temperature. The pressure is also defined through averages, using the Clausius virial theorem:

$$PV = Nk_BT + \frac{1}{3}\left\langle \sum_{I=1}^{M} \mathbf{R}_I \cdot \mathbf{f}_I \right\rangle, \tag{2.35}$$

where $\mathbf{f}_I$ is the force exterted to the Ith particle by its surrounding particles. The brackets can also be removed to define an *instantaneous pressure*, which is equal to the one third of the trace of the stress tensor, defined by its components

$$S_{ij} = \frac{1}{V} \sum_{I=1}^{M} M_I V_{i_I} V_{j_I} + \frac{1}{V} \sum_{I=1}^{M} r_{i_I} f_{j_I}, \tag{2.36}$$

where i and j are equal to x, y, z, that is, $P = (S_{xx} + S_{yy} + S_{zz})/3$.

In quantum mechanics, the Hellmann–Feynman theorem,

$$\frac{dE_\lambda}{d\lambda} = \left\langle \psi(\lambda) \left| \frac{\partial \check{\mathbf{H}}_\lambda}{\partial \lambda} \right| \psi(\lambda) \right\rangle, \tag{2.37}$$

allow us to get the forces choosing $\lambda = X_{IJ}$, where X_{IJ} is the Jth coordinate of $\mathbf{R}_I$. This leads to

$$F_{X_{IJ}} = -\frac{\partial E}{\partial X_{IJ}} = -\left\langle \psi \left| \frac{\partial \check{\mathbf{H}}}{\partial X_{IJ}} \right| \psi \right\rangle, \tag{2.38}$$

which is the Jth component of the force exterted over the Ith atom. The wave function used in this equation correspond to the ground state of the system, obtained by means of the Kohn–Sham equations, and expressing this expectation value in position representation, results in integrals of the electron density, that is, $F_{X_{IJ}} = F_{X_{IJ}}[n(\mathbf{r})]$. The force obtained this way replaces the derivative on the right hand side of equation (2.32), and advance the position of the nuclei as if they were classical particles with the same integration algorithms used for classical MD, like Verlet. This is what we know as *Born–Oppenheimer molecular dynamics.*

Canonical Ensemble

The equations of motion can also be obtained from a Lagrangian approach, where the Euler-Lagrange equations,

$$\frac{d}{dt}\left(\frac{\partial \mathscr{L}}{\partial V_{IJ}}\right) = \frac{\partial \mathscr{L}}{\partial X_{IJ}}, \tag{2.39}$$

lead to (2.31) and (2.32). The Lagrangian of the system, in this case, is

$$\mathscr{L} = K - U = \frac{1}{2}\sum_{I=1}^{M} M_I \mathbf{V}_I^2 - U(\mathbf{R}_1, \ldots, \mathbf{R}_M). \tag{2.40}$$

Under typical experimental conditions, the atoms of a material of interest are able to exchange heat with their surroundings. In this situation, the atoms exist in a canonical ensemble, where the number of particles, volume, and temperature are constant. There are a number of ways to adapt the microcanonical MD method outlined above to mimic a canonical ensemble. One of the most elegant was originally introduced by Nosé, who began by using the Lagrangian for the microcanonical ensemble, and forming an extended Lagrangian:

$$\mathscr{L} = \frac{1}{2}\sum_{I=1}^{M} M_I s^2 \mathbf{V}_I^2 - U(\mathbf{R}_1, \ldots, \mathbf{R}_M) + \frac{Q}{2}\left(\frac{ds}{dt}\right)^2 - g k_B T \ln s. \tag{2.41}$$

Notice that if $s(t) \equiv 1$, then this extended Lagrangian reduces exactly to (2.40). Applying the Euler-Lagrange equations (2.39) to this extended Lagrangian, leads to the equations of motion for the system. These equations were written by Hoover [17] in a convenient form using slightly different variables than the extended Lagrangian above:

$$\begin{aligned}\frac{dX_{IJ}}{dt} &= V_{IJ},\\ \frac{dV_{IJ}}{dt} &= -\frac{1}{M_I}\frac{\partial U(\{X_{nm}\})}{\partial X_{IJ}} - \frac{\xi}{M_I}V_{IJ},\\ \frac{d\xi}{dt} &= \frac{1}{Q}\left[\sum_{I=1}^{M} M_I\mathbf{V}_I^2 - 3Nk_BT\right],\\ \frac{d\ln s}{dt} &= \xi.\end{aligned} \tag{2.42}$$

The first and second equations correspond to (2.31) and (2.32), but the last one, the acceleration, has a "friction" term that either increases or decreases the velocity, depending on the sign of ξ. The third equation looks more meaningful when we write it down in terms of (2.34),

$$\frac{d\xi}{dt} = \frac{3Nk_B}{Q}\left[T_{MD} - T\right], \tag{2.43}$$

since it means that the rate of change of ξ depends on how far is the instantaneous temperature from the target temperature, therefore, ξ acts as a feedback control to hold the instantaneous temperature of the atoms in the simulation. The parameter Q determines how rapidly the feedback between the temperature difference $T_{MD} - T$ is applied to ξ. These equations are, again, solved by numerical integration algorithms.

In this thesis, all simulations performed in the canonical ensemble used this Nosé–Hoover thermostat. In this ensemble, the pressure fluctuates, and a desired mean pressure is obtained by an adequate choice of the volume of the simulation cell. This is subjected to the simulation time, which has to be enough to allow the pressure to converge.

Car–Parrinelo Molecular Dynamics

Although all the molecular dynamics simulations in this thesis were performed using the Born–Oppenheimer molecular dynamics (BOMD) explained above, it is worth to mention an approximation to BOMD, that was a key breakthrough that changed ab initio MD from simply an interesting idea to a powerful and useful method: the Car–Parrinello molecular dynamics (CPMD) [14]. They introduced an algorithm in which the separate tasks of following the motion of nuclei and finding the electronic ground state given the nuclear positions are treated in a unified way through an extended Lagrangian. The central idea in this approach is to define equations of motion for both the nuclei and the electronic degrees of freedom that are simultaneously followed using molecular dynamics. Car and Parrinello's extended Lagrangian is cleverly constructed with nuclear equations of motion, similar to Born–Oppenheimer and the introduction of the electronic degrees of freedom as fictitious dynamical variables. Schematically, this extended Lagrangian is

$$\mathscr{L} = \frac{1}{2}\sum_{I=1}^{M} M_I \mathbf{V}_I^2 - U(\mathbf{R}_1, \ldots, \mathbf{R}_M) + \sum_j 2\mu \int d\mathbf{r} |\dot{\psi}_j|^2 + L_{\mathrm{ortho}}, \tag{2.44}$$

where the first two terms on the right-hand side are the same as in equation (2.40), while the last two terms introduce fictitious degrees of freedom. The third term, that has the form of kinetic energy introduces a fictitious mass, μ, while the final term above is required to keep the one-electron wave functions orthogonal. When the velocities associated with the dynamics based on this lagrangian are used to assign a temperature and scaled to bring $T \rightarrow 0$, the equilibrium state of minimal E is reached and the Lagrangian describes a real physical system on the potential energy surface.

In contrast to Born–Oppenheimer molecular dynamics, wherein the nuclear degrees of freedom are propagated using ionic forces which are calculated at each iteration by approximately solving the electronic problem as explained in the previous sections, the Car–Parrinello method explicitly introduces the electronic degrees of freedom as (fictitious) dynamical variables, writing this extended Lagrangian for the system, which leads to a system of coupled equations of motion for both ions and electrons. In this way, an explicit electronic minimization at each time step, as done in Born–Oppenheimer MD, is not needed: after an initial standard electronic minimization, the fictitious dynamics of the electrons keeps them on the electronic ground state corresponding to each new ionic configuration visited along the dynamics, thus yielding accurate ionic forces. In order to maintain this adiabaticity condition, it is necessary that the fictitious mass of the electrons is chosen small enough to avoid a significant energy transfer from the ionic to the electronic degrees of freedom. This small fictitious mass, in turn, requires that the equations of motion are integrated using a smaller time step than the one commonly used in Born–Oppenheimer molecular dynamics. Because the nuclear and electronic degrees of freedom are propagated simultaneously during a CPMD calculation, the total energy that is calculated at each time step does not correspond exactly to the true Born–Oppenheimer potential energy surface for the nuclear coordinates. It is also important to realize that the dynamics of the electronic degrees of freedom during CPMD cannot be interpreted physically as the dynamics of electrons; the equations of motion for the electrons are merely a mathematical device to allow the dynamics of the nuclei to be generated in a numerically efficient way.

At the time it was introduced, the Car–Parrinello method was adopted for ab initio molecular dynamics as well as for determination of the Kohn–Sham ground state (because their technique was faster than contemporary methods for matrix diagonalization). This situation changed in the 1990s, as a variety of efficient numerical methods for solving the Kohn–Sham equations based on iterative linear algebra methods were developed and widely applied. When used appropriately, the electronic information from a previous MD step can provide a good initial approximation for the ground state of the updated nuclear positions, enabling the energy and forces for a new time step to be computed in an efficient way. Although the extended Lagrangian approach of Car and Parrinello remains influential, calculations based on direct minimization of the Kohn–Sham equations at each time step are now more widely used.

Chapter 3

Computing Properties

3.1 Solubility

Determination of stable phases of solids, clusters and other systems rely of the capacity of determining the configuration of minimum energy, which determines the most stable phase of the system. The solubility of a given material on a given solvent can also be determined using an energetic approach, computing the Gibbs free energy of solvation, corresponding to the change in Gibbs free energy when a molecule or unit of the material is removed from the pure crystal phase and dissolved in the solvent. At a given pressure and temperature, this change is given by

$$\Delta G_{\mathrm{sol}} = G(A : nB) - [G(A) + G(nB)], \tag{3.1}$$

where A corresponds to one molecule (or formula unit) of the solute, dissolved into n atoms of the solvent, B, at a concentration of $1 : n$. The material will dissolve if this difference is less than zero, and becomes more negative as solubility increases.

The first term at the right hand side of equation (3.1) represents a challenge for ab initio simulations, since it involves calculation of the electron density of a system with at least one unit of material A (2 or more atoms) and n atoms of a solvent B, where n must be large (usually more than 200). For this reason, we take the low concentration limit, where we can split this term into a sum of energies of smaller systems by means of the free energy of mixing, which we will explain below.

3.1.1 Free energy of mixing

According to classical statistical mechanics, the single-particle partition function of an ideal 3-dimensional gas of N indistinguishable particles of mass m at a temperature T, confined to a volume V, reads

$$Z = \frac{V^N}{N!}\left(\frac{mk_BT}{2\pi\hbar^2}\right)^{\frac{3N}{2}}, \tag{3.2}$$

from which the Helmholtz free energy can be calculated and, in the Stirling's approximation, takes the form

$$\begin{aligned} F &= -k_BT\ln Z & (3.3)\\ &= -k_BT\left[N\ln\left(V\left(\frac{mk_BT}{2\pi\hbar^2}\right)^{\frac{3}{2}}\right) - N\ln N + N\right] & (3.4)\\ &= -k_BTN\ln\left[\frac{Ve}{N}\left(\frac{mk_BT}{2\pi\hbar^2}\right)^{\frac{3}{2}}\right]. & (3.5)\end{aligned}$$

where k_B is the Boltzmann constant. Therefore, if we have a system of three species, with atomic masses m_a, m_b and m_c, and number of atoms per species N_a, N_b and N_c in a container of volume V, its free energy will be

$$F_1 = -k_BT\left[N_a\ln\left(\frac{Ve}{N_a\Lambda_a^3}\right) + N_b\ln\left(\frac{Ve}{N_b\Lambda_b^3}\right) + N_c\ln\left(\frac{Ve}{N_c\Lambda_c^3}\right)\right], \tag{3.6}$$

where $e = \exp(1)$ and $\Lambda_a = \sqrt{\frac{2\pi\hbar^2}{m_ak_BT}}$, $\Lambda_b = \sqrt{\frac{2\pi\hbar^2}{m_bk_BT}}$ and $\Lambda_c = \sqrt{\frac{2\pi\hbar^2}{m_ck_BT}}$ are the thermal de Broglie wavelengths associated with each type of particle. The expression above corresponds to the free energy of a solution containing atoms of types a, b and c.

Consider a system formed by one atom of type b and $N_a/2$ atoms of type a, and another with one atom of type c and $N_a/2$ atoms of type a. Let the volumes of these systems be V_b and V_c, respectively. Their respectives free energies will be

$$\begin{aligned} F_b &= -k_BT\left[\frac{N_a}{2}\ln\left(\frac{V_b\,e}{(N_a/2)\Lambda_a^3}\right)+N_b\ln\left(\frac{V_b\,e}{N_b\Lambda_b^3}\right)\right], && (3.7)\\ F_c &= -k_BT\left[\frac{N_a}{2}\ln\left(\frac{V_c\,e}{(N_a/2)\Lambda_a^3}\right)+N_c\ln\left(\frac{V_c\,e}{N_c\Lambda_c^3}\right)\right], && (3.8)\end{aligned}$$

where $N_b = N_c = 1$. If systems b and c are mixed together, as shown in figure 4, we will have a solution in a volume $V = V_b + V_c$, with N_a atoms of type a, $N_b = 1$ atoms of type b and $N_c = 1$ atom of type c, which represents a molecule, formed by one atom of type b and one of type c, dissolved in a solvent formed by atoms of type a. The free energy of this system will be given by equation (3.6), representing the final energy of the system, $F_{\text{final}} = F_1$. The free energy of mixing, ΔF, can be found by substracting $F_{\text{initial}} \equiv F_b + F_c$ from F_{final}:

$$\Delta F = F_{\text{final}} - F_{\text{initial}} = -k_BT\left[N_a\ln\left(\frac{V}{2V_b^{\frac{1}{2}}V_c^{\frac{1}{2}}}\right)+\ln\left(\frac{V^2}{V_bV_c}\right)\right]. \tag{3.9}$$

For $V_b = V_c$, we will have a final container of volume $V = 2V_b$, and the expression above reduces to

$$\Delta F = -2k_BT\ln(2). \tag{3.10}$$

If we have more than one atom of a given species in the solute, say 2 atoms of type c, in a diluted system of a-type atoms, we will consider this system as the final state of three different systems mixed together: the first one with one atom of type b and $N_a/3$ of type a, confined to a volume V_b; the second with one atom of type c and $N_a/3$ of type a, confined to a volume V_c; and the third one identical to the second one. To calculate the free energy of the mixed system in this case, we have to add a fourth term to equation (3.6) ($N_d\ln(e\,V/N_d\Lambda_d)$; $N_d = 1$) where Λ_d and the energy

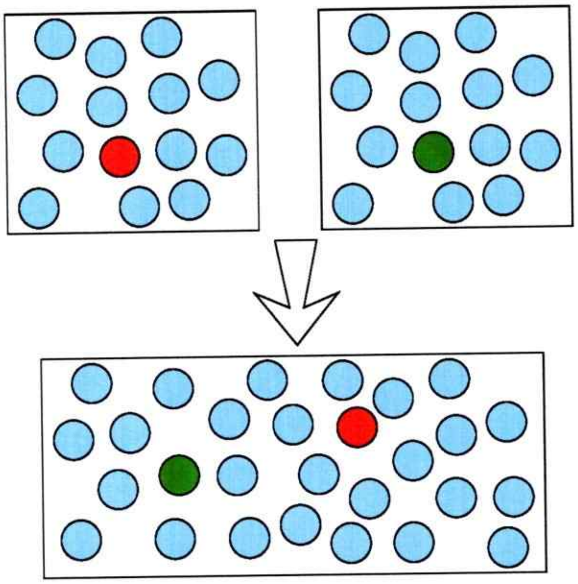

Fig. 4: Two systems mixed together, one containing one containing $N_a/2$ atoms of type a and one atom of type b, an the other containing $N_a/2$ atoms of type a and one of type b.

of the new third container, F_d, are defined analogously to equations (3.7) and (3.8). This additional term results in a free energy of mixing

$$\Delta F = F_{\text{final}} - F_{\text{initial}} = -k_B T \left[N_a \ln \left(\frac{V}{3V_b^{\frac{1}{3}} V_c^{\frac{1}{3}} V_d^{\frac{1}{3}}} \right) + \ln \left(\frac{V^3}{2V_b V_c V_d} \right) \right], \quad (3.11)$$

which, for $V_b = V_c = V_d = V/3$, reduces to

$$\Delta F = -k_B T \ln \left(\frac{27}{2} \right). \quad (3.12)$$

3.1.2 Gibbs free energy of solvation

Now we have an expression for the free energy of mixing, and we can split the first term on the right hand side of (3.1). We are interested in solutes of the type $A = MX$ and $A = MX_2$, where M and X are two different atoms (Mg and O, for example). We will consider the dissolved system, with Gibbs free energy $G(A : nB)$, as the final state of two smaller systems mixed together, each with one atom of the solute, as depicted in figure 4. The energies of the initial systems are $G(\mathrm{B}_{n/2}\mathrm{M})$ and $G(\mathrm{B}_{n/2}\mathrm{X})$, and when the systems are mixed together, considering that the volume of each one is approximately the same at a given pressure, the total Gibbs free energy will be

$$G(MX : nB) \approx G(\mathrm{B}_{n/2}\mathrm{M}) + G(\mathrm{B}_{n/2}\mathrm{X}) - 2k_BT\ln(2). \tag{3.13}$$

The last term arises from the free energy of mixing (3.10). If we have a solute of the type $A = MX_2$, like $\mathrm{SiO_2}$ or $\mathrm{FeO_2}$, the free energy of mixing will be given by (3.12), which leads to

$$G(MX_2 : nB) \approx G(\mathrm{B}_{n/3}\mathrm{M}) + G(\mathrm{B}_{n/3}\mathrm{X}) + G(\mathrm{B}_{n/3}\mathrm{X}) - k_BT\ln\left(\frac{27}{2}\right). \tag{3.14}$$

3.1.3 Solvation at different concentrations

When the Gibbs free energy of solvation ΔG_{sol} is obtained for a given concentration, it can be used to calculate which will be the free energy of solvation at other concentrations. The difference between the free energy of solvation at a concentration $1 : n$ and energy of solvation at a concentration $1 : m$ is given by

$$\Delta G(n, m) \equiv \Delta G_{\mathrm{sol}}(A : mB) - \Delta G_{\mathrm{sol}}(A : nB), \tag{3.15}$$

which can be expressed, as a summation of Hemlholtz free energies:

$$\Delta G(n, m) = F_0(A : mB) - F_0(A : nB) - F_0((m - n)B), \tag{3.16}$$

that can be approximated by

$$\Delta G(n, m) = (-kT)\left[m\ln\left(\frac{mV_B + V_A}{mV_B}\right) - n\ln\left(\frac{nV_B + V_A}{nV_B}\right) + 3\ln\left(\frac{mV_B + V_A}{nV_B + V_A}\right)\right], \tag{3.17}$$

where V_A and V_B are the solute and solvent effective volumes, respectively. A detailed derivation of these expression can be found in the appendix B.

3.2 Thermodynamic Integration

Since the Helmholtz free energy F of a system is not simply a function of the phase space coordinates of the system, but is instead a function of the Boltzmann-weighted integral over phase space (i.e. partition function), it cannot be calculated directly. Therefore, the Gibbs free energy $G = F + PV = U - TS + PV$, needed to calculate solvation energies, is not directly accessible in standard molecular dynamics simulations either. One way to address this problem is by means of a technique called *thermodynamic integration* (TDI), a method that yields the difference in Helmholtz free energy $\Delta F = F_B - F_A$ between two given systems: a reference system A and a system B, whose potential energies U_A and U_B have different dependences on the spatial coordinates. The basis of this technique is that ΔF is the work done on reversibly and isothermally switching from the reference total energy function U_A to the total energy U_B. This technique has been widely used [18–24], and will play the most important role in this thesis regarding to the calculation of solvation energies.

In TDI, a hybrid potential that connects the states A and B is defined by

$$U(\lambda) = U_A + \lambda(U_B - U_A), \tag{3.18}$$

where $U_A = U_A(\{\mathbf{R}_I\})$ and $U_B = U_B(\{\mathbf{R}_I\})$ depend on the instantaneous positions of the atoms, $\{\mathbf{R}_I\}$. For a given value of λ, the free energy of a system governed by this potential will be defined by

$$F(N, V, T, \lambda) = -k_B T \ln Z(N, V, T, \lambda), \tag{3.19}$$

where Z the partition function of the system,

$$Z(N, V, T, \lambda) = \sum_s e^{-U_s(\lambda)/k_B T}. \tag{3.20}$$

In these notation, $U_s(\lambda)$ is the potential energy of a state s in the canonical ensemble with potential energy function $U(\lambda)$ as defined above. Then, if we take the derivative of F with respect to λ, we will get that it equals the ensemble average of the derivative of potential energy with respect to λ, and its integral corresponds to the change in free energy ΔF between states A and B:

$$\begin{aligned}
\Delta F(A \to B) &= \int_A^B dF && (3.21)\\
&= \int_0^1 d\lambda \frac{\partial F}{\partial \lambda} && (3.22)\\
&= -\int_0^1 d\lambda \frac{k_B T}{Z}\frac{\partial Z}{\partial \lambda} && (3.23)\\
&= \int_0^1 d\lambda \frac{k_B T}{Z}\sum_s \exp\left[-U_s(\lambda)/k_B T\right]\frac{1}{k_B T}\frac{\partial U(\lambda)}{\partial \lambda} && (3.24)\\
&= \int_0^1 d\lambda \left\langle \frac{\partial U(\lambda)}{\partial \lambda} \right\rangle. && (3.25)
\end{aligned}$$

For the particular choice of the hybrid potential shown in (3.18), the last equation reads

$$\Delta F = \int_0^1 d\lambda \ \langle U_B - U_A \rangle \qquad (3.26)$$

where the angle brackets denote an average, that depends on λ, taken over trajectories generated in the system governed by the hybrid potential energy function $U(\lambda)$. The figure 5 shows a typical example of the variation of $< U_B - U_A >$ as λ increses. For $\lambda = 0$, the particles are interacting only through the potential U_A, and the interaction is changed smoothly through λ, until the system interacts completely through the potential U_B for $\lambda = 1$.

The practical feasibility of calculating ab initio free energies of liquids and anharmonic solids depends on finding a reference system A for which F_A is readily calculable and the difference $U_B - U_A$ is very small. When ΔF is obtained through

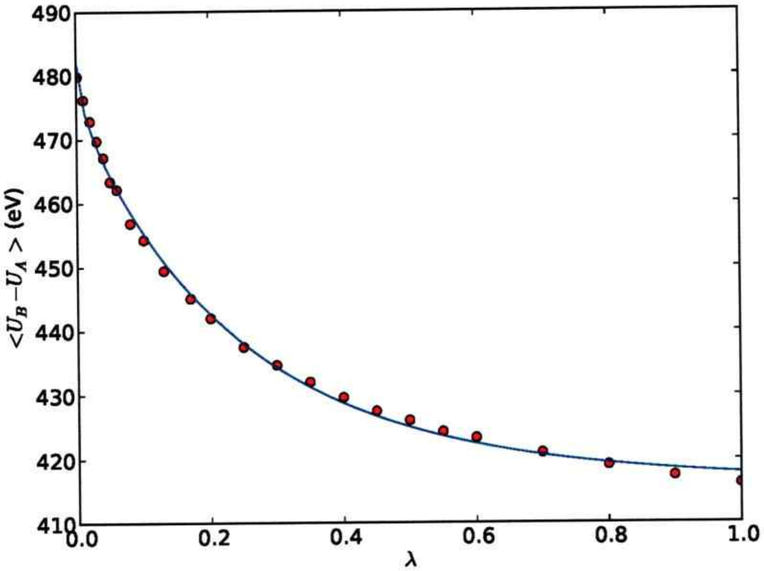

Fig. 5: Thermodynamic Integration: Variation of $< \partial U(\lambda)/\partial\lambda >$ with respect to λ for a silicon oxide (SiO_2) system calculated in this thesis (see chapter 4), when the reference system A is an ideal gas, and the system of interest B is a liquid. The area below this curve represents ΔF.

equation (3.26), the free energy of the system interacting though the potential U_B can be obtained by

$$F_B = F_A + \Delta F. \tag{3.27}$$

For liquid systems, the reference system A is usually chosen as a noninteracting system (ideal gas, $U_A = 0$), with free energy

$$F_{\text{ideal gas}} = -Nk_BT\left(1 + \ln\left(\frac{V}{N}\left(\frac{2\pi mk_BT}{h^2}\right)^{\frac{3}{2}}\right)\right), \tag{3.28}$$

while for solid systems, A is chosen to be a system of non-interacting, three-dimensional harmonic oscillators ($U_A = \frac{1}{2}m\omega^2r^2$), with free energy

$$F_{\text{harm-osc}} = Nk_BT\ln\left(\frac{\hbar\omega}{k_BT}\right). \tag{3.29}$$

In both cases, B is the ab initio system with unknown free energy, which we want to obtain. To reduce the fluctuations and make the difference $U_B - U_A$ small, an intermediate step can be considered, in which the system is taken from the reference system A to a classical system interacting via a pairwise potential, whose parameters are fitted from the ab initio simulations. For solid systems, inverse-power models (like Lennard-Jones potential) are usually not good enough, but adding a contribution of a harmonic term represents the anharmonic solid more accurately [18,25]. When the free energy of this intermediate system is determined, it is used as a new reference system to determine the free energy of the ab initio system, given by $F_{\mathrm{DFT}} = F_{\mathrm{an}} + \Delta F_{\mathrm{an}\to\mathrm{cl}} + \Delta F_{\mathrm{cl}\to\mathrm{DFT}}$, where $F_{\mathrm{an}} = F_A$ is the analytically known free energy of the reference system A, F_{cl} that of the classical-pairwise-potential interacting system, and $F_{\mathrm{DFT}} = F_B$ the free energy of the ab initio system to determine. This two-step thermodinamic integration is the procedure considered for the calculations in the following chapter.

Chapter 4

Rocky Core Erosion in Jupiter and Giant Exoplanets

Silica (SiO_2) is an abundant component of the Earth whose crystalline polymorphs play key roles in its structure and dynamics. Together with ices, is also one of the most important ingredients of the central solid core of giant planets and part of the bulk composition of the so called super-Earths and ocean planets [26]. Experiments on silica has been carried out for decades, but planetary conditions are often hard (or impossible) to reach, and the thermodynamic properties of silica at high pressure remain elusive. This chapter describes calculations of the Gibbs free energy of solvation for silica dissolved into metallic hydrogen to determine if the solid core of gas giants can be eroded. The chapter starts with an introduction to the significance of silica for planetary science and goes over previous theoretical work and challenges. In the final sections, computational details and results are discussed. The calculation of the free energy of solvation indicates that solubility takes place over 5000 K when pressures exceed 1000 GPa, which contributes to dissolve the core of gas giants and provides an alternative explanation for the observed heavy element enrichment in giant planet atmospheres, which is currently attributed to late-arriving planetesimals [27, 28].

4.1 Introduction

Most of the information we have about materials that make the rocky bodies in space comes from the study of meteories [29, 30]. The library of meteorites that have fallen to Earth provide a range of plausible starting compositions for planetary accretion and degassing. The chondrites are the least processed and therefore most primitive meteorite class. Chondrites contain a variety of silicate components, including chondrules (perhaps the earliest condensed material from the planetary nebula), minerals such as olivine and pyroxene, silicates, silicate glass, and in some cases water or carbon-rich veins, indicating alteration after formation [31]. In these meteorites, water is most often in the form of OH within a silicate mineral crystal. The reason the OH within the mineral is called water is that it likely existed as water when the mineral formed and if the mineral melts the OH is released as water. Many chondrites have low oxygen contents and thus also contain metallic iron and nickel. A second class of meteorites is the achondrites. Achondrites generally lack metallic iron and are thought to represent the silicate remnants of planetesimals that accreted and differentiated into metallic iron cores and silicate mantles, only to be broken apart in later collisions. Achondrites have far lower water contents than do most chondrites. Achondrites can contain up to ~3 mass% water, although many have no water at all. More modern simulations of accretion indicate that planets form from differentiated planetary embryos on the scale of thousands of kilometers in radius and that these embryos move radially in the solar system during accretion and so form planets that are mixtures of material from the inner and outer disk. Even assuming planetary formation from differentiated material only, the range of possible bulk compositions for terrestrial planets in our solar system is extremely wide.

Many of the confirmed 1700 extrasolar planets are gas giants that are primarily composed of dense fluid hydrogen and helium. Furthermore the *Kepler* mission has detected 3846 planet candidates and has measured their radii and orbital periods within 22 months of observations [32]. In a few cases with multiple planets in close orbits, masses have been inferred from transit-timing variations [33]. The Juno mission is scheduled to arrive at Jupiter in 2016 and will measure the gravitational field of our largest local gas giant with an unprecedented accuracy, revealing clues about its inner mass distribution. Existing core-accretion models for gas giant formation [34] hold that these planets form from the rapid accretion of gas around a rock–ice protocore (planetary embryos). Therefore, according to our understanding, the evolution of giant planets starts with a differentiated rocky core surrounded by an envelope of hot, dense hydrogen–helium gas. The temperature in the envelope rises, and the gravitational energy from accretion is converted to heat. An adiabatic temperature is rapidly established. The evolution of a giant planet is controlled by the energy loss due to thermal radiation [35]. Conventional giant planet models assume a stable core and a sharp core–mantle boundary instead of taking into account the possibility that the metallic hydrogen layer may act as solvent for the initial protocore. Answering the question of whether giant planet cores remain stable on a billion year time scale may also provide an alternative explanation for the observed heavy element enrichment in giant planet atmospheres, which is currently attributed to late-arriving planetesimals [27, 28]. If a core dissolved, it would lead to double diffusive convection [4, 36–38] because gravity opposes the redistribution of heavy core materials. This would introduce compositional stratification and significantly reduce the rate at which heat can be transported out of the interior, with substantial implications for the thermal evolution and radius contraction of giant planets [39].

4.2 Previous work and motivation

The importance of silica as a prototype and potentially key member among super-Earths mantle minerals and as a rock-forming element of the cores of gas giants, has prompted a number of theoretical studies [30, 40–48]. Since the rocky components of the initial cores of giant planets are likely to be dominated by iron and magnesium silicate minerals, silica appears as an important, representative material. It was shown by Umemoto *et al.* [47] that post-perovskite $MgSiO_3$ separates into MgO and SiO_2 beyond ~ 10 Mbars and ~ 10000 K, which are conditions that are expected to be exceeded at the core–mantle boundaries of typical gas giant planets. Recent ab initio calculations predicted a substantial solubility of MgO, water ice, and iron in fluid metallic hydrogen for the core–mantle boundary of Jupiter and Saturn [21, 22, 49]. Therefore, this study is focused on the solubility of remaining core material, SiO_2, which will allow us to obtain a more complete picture of the behavior of metallic hydrogen as a solvent for planetary core materials.

At the core boundary of giant planets, the temperature and pressure conditions are estimated to be on the order of 10–40 Mbar and 10000 to 20000 K. Because such extreme conditions cannot yet be probed with laboratory experiments, we use ab initio (DFT) computer simulations that can be used directly to characterized material at such P–T conditions [20, 23, 50, 51].

4.3 Computational Methodology

This section discusses the general computational methods and choices made for all silica calculations. The first section describes how the free energy of solvation was calculated, and the second section gives the details of the pseudopotentials, Brillouin zone sampling and crystal structure used in the DFT calculations.

4.3.1 Free energy of solvation

We have calculated the Gibbs free energy of solvation ΔG_{sol} of $\mathrm{SiO_2}$ into metallic hydrogen which, as described in section 3.1, is given by the difference between the Gibbs free energy of the dissolved system and that of the separate compounds at fixed pressure–temperature conditions:

$$\Delta G_{\mathrm{sol}}(\mathrm{SiO_2} : 384\mathrm{H}) = G(\mathrm{H_{384}SiO_2}) - [G(\mathrm{H_{384}}) + G(\mathrm{SiO_2})] \tag{4.1}$$

We begin by computing the free energy of solvation of $\mathrm{SiO_2}$ for a mixing ratio of one solute atom per 128 hydrogen atoms (i.e., one $\mathrm{SiO_2}$ formula unit to 384 H) and later generalize our results to other concentrations. Given the large quantity of hydrogen gas in giant planets, we are primarily concerned with the low-concentration limit. Thus, we can assume that solute atoms do not interact with each other, approximating the energy of the dissolved as a sum of the energy of two independent systems, taking into account the free energy of mixing, as described in section 3.1.1 and 3.1.2, that is,

$$G(\mathrm{H_{384}SiO_2}) \approx G(\mathrm{H_{128}Si}) + 2G(\mathrm{H_{128}O}) - k_B T \log(27/2). \tag{4.2}$$

Since the entropy term in the Gibbs free energies, $G = E + PV - TS = F + PV$, is not directly accessible in standard molecular dynamics simulations, we used the thermodynamic integration (TDI) technique, described in section 3.2, which allow us to calculate the Gibbs free energy through the addition of PV to the Hemlholtz free, F. The splitting of the Gibbs free energy of solvation now depends on the energies of four different, independent systems: pure silica ($G(\mathrm{SiO_2})$), pure fluid hydrogen ($G(\mathrm{H}_{384})$), fluid hydrogen with one O atom ($G(\mathrm{H}_{128}\mathrm{O})$) and fluid hydrogen with one Si atom ($G(\mathrm{H}_{128}\mathrm{Si})$). This significantly reduces the size of the system to be simulated and the need to wait for the dissolution process to happen, which would be extremely time-consuming. Therefore, we need to perform four separate sets of simulations at each pressure and temperature. In TDI, we took five equally spaced λ values between 0 and 1 for each of them to get a smooth curve of $\langle U_B - U_A \rangle$ versus λ that can be interpolated via quadratic interpolation to determine the integral. Once we have obtained $\Delta F = F_B - F_A$, we add the known free energy F_A to determine the energy of the system, F_B, governed by the potential U_B.

The TDI is performed in two steps: first from a system governed by DFT forces to a system interacting via a classical pair potential and then from the classical system to a reference system with a free energy that is known analytically. For fluids, we chose an ideal gas, given by equation (3.28), while for solid systems we selected a system of independent harmonic oscillators as the reference system, whose free energy is given by (3.29). For the fluid systems, we constructed the classical two-body potentials by fitting to the forces of a DFT-MD trajectory using the force-matching methodology [52, 53]. In the case of a solid SiO_2 system, we first determined the harmonic spring constants from mean squared displacement from an atom's lattice site and then fitted the residual forces with pair potentials.

4.3.2 DFT Calculations

Pseudopotentials We used pseudopotentials of the projector-augmented wave (PAW) type [54] provided by the VASP code [55], choosing the GGA-based exchange-correlation functional of Perdew, Burke and Ernzerhof (PBE) [56]. The silicon potential has a Ne core, and takes the 3s and 3p semi-core electrons in their valence configuration, while the oxigen pseudopotential has a He core with the 2s and 2p semi-core electrons in their valence band. For hydrogen, the pseudopotential with one 1s electron provided by VASP was used, which gives excellent description of the bond length for the H_2 dimer, and for H on C surfaces. An energy cutoff of 900 eV was used for the plane-wave expansion to ensure convergence do to the high temperatures analyzed.

K-point sampling For sampling the Brillouin zone of the hydrogen and hydrogen+(Si,O) supercells, we implemented a $2\times2\times2$ Monkhorst-Pack k-point mesh [57], while for the SiO_2 supercell we used Γ point only. An MD time step of 0.2 fs was used, and the simulation time ranged between 0.5 and 2.0 ps. The simulations are confined to the Born-Oppenheimer surface, and the effect of finite temperature on the electronic structure is included through Mermin's formalism [58]. The ΔG_{sol} values were confirmed to be well converged with respect to these parameters for the purpose of this dissolution calculation.

Crystal structure For pure solid SiO_2, we used a 72-atom supercell in the Fe_2P-type structure (space group P-62m), recently predicted by Tsuchiya [46] to be the ground-state structure at pressures above 7 Mbar. For liquid SiO_2, we used a cubic cell with 96 atoms. We analyzed stability of each material phase at pressures ranging from 10 to 40 Mbar and temperatures ranging from 3000 to 20000 K and confirmed that the structure remained solid for all cases under consideration, except for 20000 K and 20 Mbar, where we found liquid SiO_2 to be the stable phase.

P (Mbar)	T (K)	$G(H_{128})$ (eV)	$G(H_{128}O)$ (eV)	$G(H_{128}Si)$ (eV)	$G\ (SiO_2)$ (eV)
10	3000	671.4(2)	688.6(2)	705.4(3)	63.3(1)
10	5000	559.0(5)	573.5(4)	590.5(5)	60.2(1)
20	3000	1270.7(2)	1304.7(2)	1330.1(3)	121.0(1)
20	5000	1170.8(4)	1202.4(5)	1228.2(3)	118.4(1)
20	10000	843.2(4)	868.3(4)	893.8(2)	109.1(4)
20	20000	17.3(5)	26.9(6)	53.6(7)	81.8(1)
40	3000	2131.4(2)	2191.8(2)	2229.4(1)	211.3(1)
40	7000	1936.2(3)	1991.4(3)	2030.7(3)	206.0(2)
40	10000	1747.4(1)	1799.0(6)	1837.6(9)	200.6(3)
40	15000	1384.3(8)	1427.9(4)	1467.6(8)	190.1(4)

Table 4.1: Gibbs Free Energies of pure hydrogen, hydrogen with oxygen, hydrogen with silicon, and SiO_2 (solid in all cases, except for 20 Mbar and 20000 K).

P (Mbar)	$\rho(H_{128})$ ($g\,cm^{-3}$)	$\rho(H_{128}O)$ ($g\,cm^{-3}$)	$\rho(H_{128}Si)$ ($g\,cm^{-3}$)	$\rho\ (SiO_2)$ ($g\,cm^{-3}$)
10	1.88	2.05	2.19	9.52
20	2.27	2.49	2.66	11.19
40	3.48	3.80	4.06	15.36

Table 4.2: Densities of metallic hydrogen (H_{128}), $H_{128}Si$, $H_{128}O$ and SiO_2 systems at 10, 20 and 40 Mbar. The density of silica at ambient pressure (quartz) is 2.66 $g\,cm^{-3}$, while the density of pyrite-type silica is 6.58 $g\,cm^{-3}$ at 271 GPa (2.71 Mbar) and 300 K [43]. Beyond 40 Mbar, its density is greater than that of lead (11.35 $g\,cm^{-3}$).

4.4 Results

Gibbs energies were computed for the following system sizes: H_{128}, $H_{128}Si$, $H_{128}O$, solid SiO_2, which are summarized in Table 4.1. These results are used in conjunction with the equations (4.1) and (4.2) to obtain the Gibbs free energies of solvation in Table 4.3, and plotted as function of temperature in figure 6. We also show the density ρ of each system in Table 4.2 for reference.

The error bars on the G values are dominated by two terms, the more significant

P (Mbar)	T (K)	ΔG_{sol} (eV)
10	3000	4.92 ± 0.69
10	5000	0.32 ± 1.90
20	3000	6.35 ± 0.78
20	5000	2.18 ± 1.63
20	10000	-8.37 ± 1.45
20	20000	-26.47 ± 2.14
40	3000	7.40 ± 0.63
40	7000	-0.93 ± 1.19
40	10000	-7.13 ± 1.60
40	15000	-19.59 ± 2.55

Table 4.3: Gibbs free energies of solubility for SiO_2 into hydrogen at a concentration of one part in 384 hydrogen atoms.

one being the uncertainty in the volume at the desired pressure due to finite simulation time and the other being the uncertainty in the $\langle U_{\mathrm{DFT}} - U_{\mathrm{classical}} \rangle$ terms in the TDI.

A negative Gibbs free energy implies that the dissolved state has a lower Gibbs free energy than the separate phases, demonstrating that solvation is preferred at a concentration of 1:384. A positive free energy indicates that the fluid system is supersaturated and that deposition of fluid SiO_2, or formation of solid grains, will be thermodynamically favored.

Gibbs free energy of solvation can be generalized to other concentrations without performing additional DFT-MD simulations if the average separation between solute atoms is large enough so that their interaction can be neglected. Under this assumption, the free energy of mixing yields the difference of ΔG_{sol} between a solution of

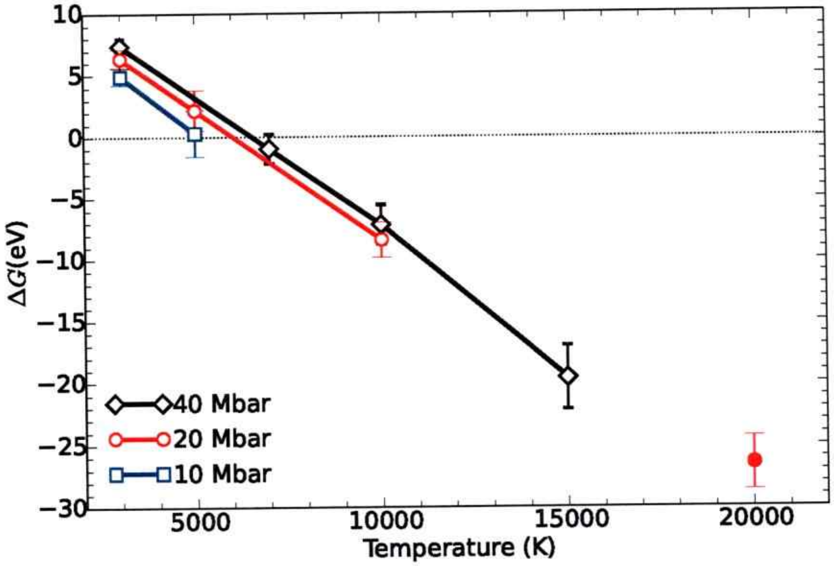

Fig. 6: Computed solvation curve ΔG for different pressures, where a negative Gibbs free energy represents a preference for the dissolved state. Open squares, circles, and diamonds represent states where SiO_2 is solid, while the filled red circle corresponds to a state where SiO_2 was found to be liquid.

one SiO_2 formula unit in m versus n hydrogen atoms (see section 3.1.3),

$$\begin{aligned} \frac{\Delta G_{\text{sol}}[m] - \Delta G_{\text{sol}}[n]}{k_B T} &= m \ln\left(\frac{mV_{\text{H}} + V_{\text{S}i} + 2V_{\text{O}}}{mV_{\text{H}}}\right) \\ &\quad -n \ln\left(\frac{nV_{\text{H}} + V_{\text{S}i} + 2V_{\text{O}}}{nV_{\text{H}}}\right) \\ &\quad +3 \ln\left(\frac{mV_{\text{H}} + V_{\text{S}i} + 2V_{\text{O}}}{nV_{\text{H}} + V_{\text{S}i} + 2V_{\text{O}}}\right), \end{aligned} \tag{4.3}$$

where V_{H}, V_{O} and V_{Si} are the effective volumes of the H, O, and Si atoms that we obtained by comparing the volumes of the different fluid simulations at the same pressure and temperature. Using a linear interpolation for the data in Table 4.3, we can determine the saturation concentration for SiO_2 in fluid hydrogen as a function of temperature and pressure throughout the 10–40 Mbar and 3000–20000 K range. A contour plot of constant saturation solubility is shown in figure 7. Solute concentrations higher than 1:100 are not shown because they may lead to interactions between solute atoms. Despite error bars of approximately 1000 K that should be considered to be uncertainties of the contours, these results show that SiO_2 is highly soluble at both Jupiter's and Saturn's core–mantle boundary conditions. This is in contrast to MgO, which may be not be as highly soluble at Saturnian core conditions. Therefore, there exists the possibility that SiO_2 may dissolve from Saturn's core but leave solid MgO behind.

The Gibbs free energy of solubility ΔG may be split into three components: an internal energy component ΔU, a volume contribution $P\Delta V$, and an entropic term $-T\Delta S$, which lead to $\Delta G = \Delta U - T\Delta S + P\Delta V$. The $P\Delta V$ and ΔU values can be directly extracted from standard DFT-MD simulations. The remaining term is $-T\Delta S$, which is obtained by substracting ΔU to the calculated ΔF in TDI. All terms are shown in figures 8, 9 and 10 as a function of temperature for 10, 20 and 40 Mbar. The $P\Delta V$ term was comparatively close to zero but, in the 20 Mbar

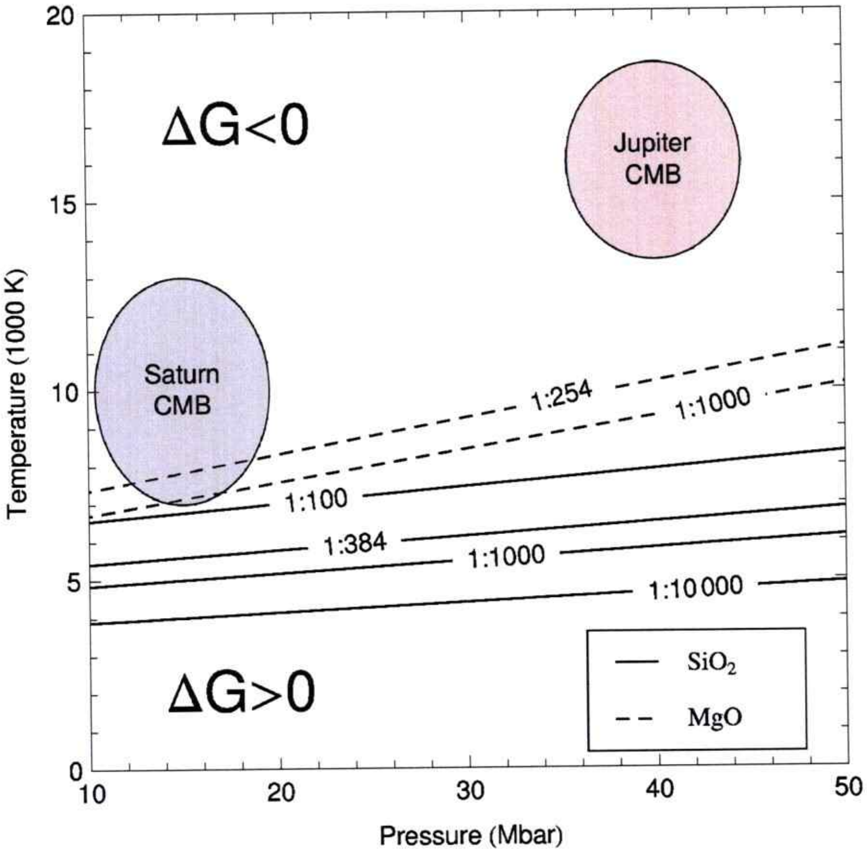

Fig. 7: Saturation solubility of SiO_2 in metallic hydrogen (this work; solid lines) and MgO (from [21]; dashed lines) as a function of temperature and pressure. At a given concentration, the system dissolves ($\Delta G < 0$) for temperatures above the line indicating the saturation solubility at that concentration. The temperature–pressure conditions of the Jovian and Saturnian core–mantle boundaries are shown for comparison.

case, shows a slight preference of approximately 0.5–3.5 eV for materials to remain separate, suggesting the dissolution reaction is not a pressure-driven process. The ΔU term also shows an energy barrier against dissolution that is slightly larger than the $P\Delta V$ term. For all temperatures under consideration, the entropic term $-T\Delta S$ is negative, confirming that more disorder is present in the dissolved state. The $-T\Delta S$ term exhibits a steep negative slope as a function of temperature that introduces a sign change into the Gibbs energy balance at $T = 6000$ K for 20 Mbar. Above this temperature, dissolution is favored, which can be considered to be an entropy-driven process similar to H_2O and MgO [21, 22]. For iron, the $-T\Delta S$ term also favors dissolution, but there is no energy barrier to overcome because at megabar pressures, hydrogen and iron are both metals that mix at low temperatures [49].

Figure 9 shows that the Gibbs free energy of solubility depends linearly on temperature. This trend continues into the liquid phase, as our 20 000 K data point confirms. For the temperature interval from 10 000 and 20 000 K where one expects SiO_2 to melt at 20 Mbar [59], this trend implies that the Gibbs free energy difference between the solid and liquid phases is small compared with the Gibbs free energy change induced by dissolution. If SiO_2 melts in the vicinity of the dissolution transition, one would expect this transition to introduce only a modest change in slope into saturation solubility curves in figure 7 because the Gibbs free energy changes continuously across the melting transition.

4.5 Astrophysical Implications

Our results have important implications for the evolution of giant planets. We predict that the SiO_2 component has been eroded from the cores of Jupiter and Saturn (see figure 3) while MgO in Saturn's core may remain stable. Therefore, a partial solvation

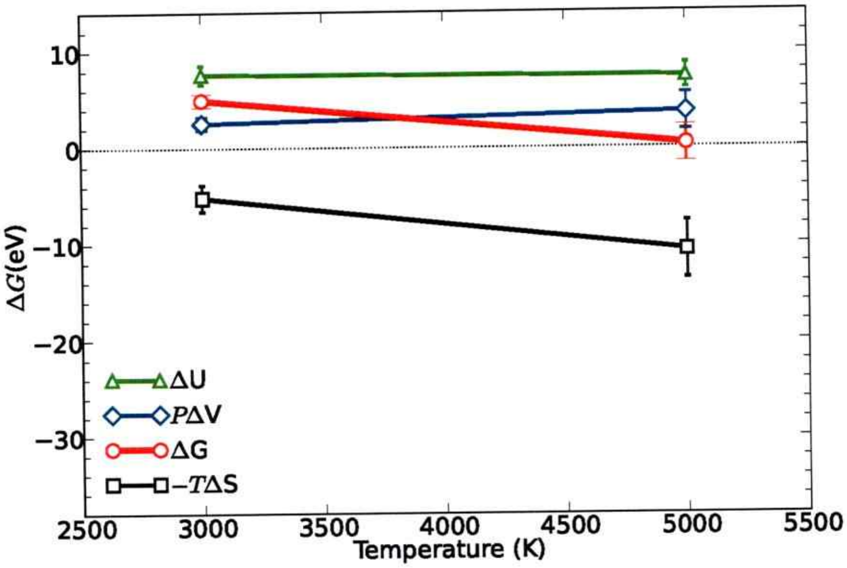

Fig. 8: Splitting of ΔG at 10 Mbar into its three constituent components: the internal energy term ΔU that represents differences in chemical binding, the $P\Delta V$ term that arises from volume differences, and the remaining $-T\Delta S$ term which represents entropic effects.

of the Saturnian core could have taken place, taking away more volatile materials like SiO_2 and water ice and leaving behind less soluble materials like MgO. Because of the differences between the solubility curves of MgO and SiO_2 in figure 7, partial core erosion may also occur in extrasolar gas giant planets that are smaller than Saturn but still large enough to contain metallic hydrogen. In general, larger and hotter interiors are expected to promote core erosion and a greater degree of redistribution of heavy material [36]. Provided the necessary energy for convection, the material may be redistributed throughout the entire planet, leading to an enrichment in heavy elements in giant planet atmospheres that have previously been attributed to late-arriving planetesimals.

Alternatively, the rate of redistribution may be hampered by compositional stratification that is the result of double-diffusive convection [4,36,37]. The stratification

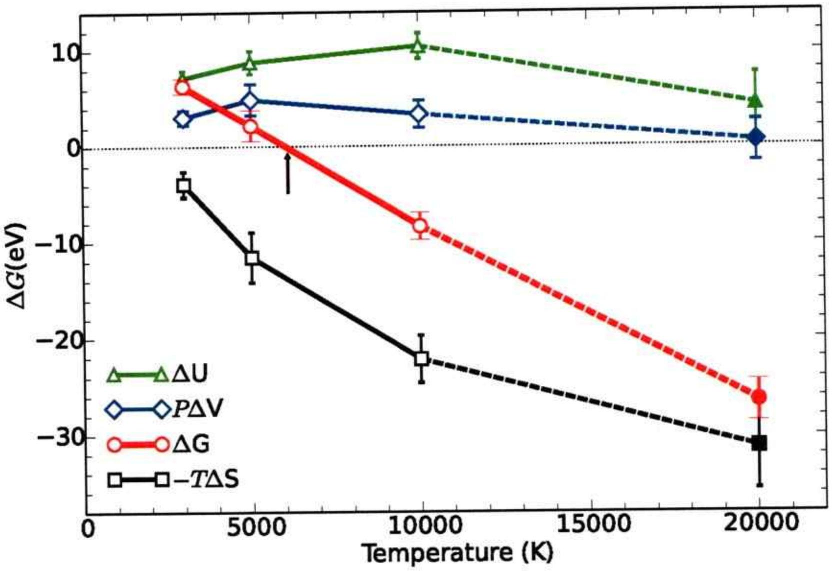

Fig. 9: Splitting of ΔG at 20 Mbar into its three constituent components: the internal energy term ΔU that represents differences in chemical binding, the $P\Delta V$ term that arises from volume differences, and the remaining $-T\Delta S$ term that represents entropic effects. The arrow denotes the temperature above which dissolutions are favored at the concentration of one SiO_2 in 384 hydrogen atoms.

would also limit the heat transport from the core, delay a planet's cooling, and possibly explain the inflated radii that have been observed for a large of number giant exoplanets [39].

Our results confirm that the core erosion must be taken into account when future models of giant planet interiors are constructed. The redistribution of heavy elements has important implications in the heat transport and mass distribution, and core erosion plays a fundamental role in this aspect since it may be the source of the presence of these elements in the outer layers. Further models for the upconvection of core material are also necessary to understand the present structure of Jupiter and other planets, whose effects may be reflected on the gravitational moments to be measured by the Juno mission.

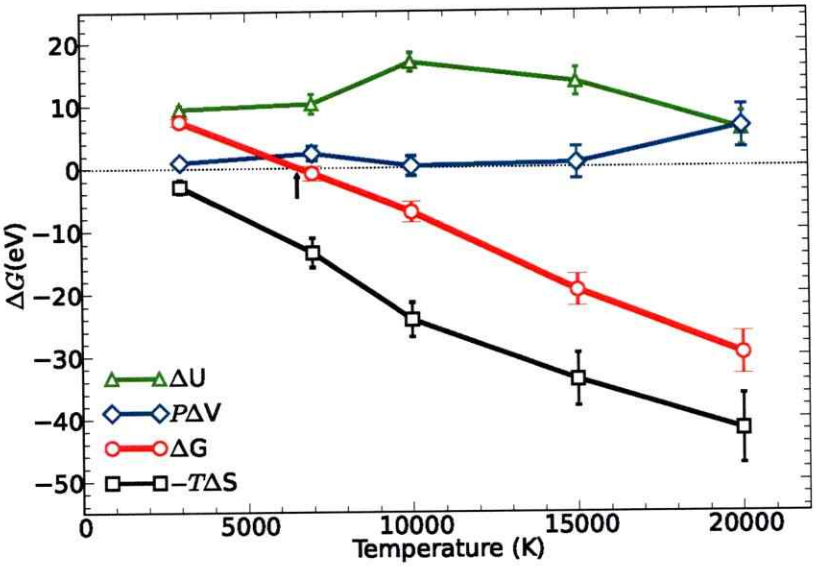

Fig. 10: Splitting of ΔG at 40 Mbar into its three constituent components: the internal energy term ΔU that represents differences in chemical binding, the $P\Delta V$ term that arises from volume differences, and the remaining $-T\Delta S$ term which represents entropic effects. The arrow marks the temperature above which dissolutions favored at concentration of one SiO_2 in 384 hydrogen atoms.

4.6 Conclusions

This chapter has presented DFT calculations of the Gibbs free energy of solvation of silica into metallic hydrogen for different pressures and concentrations. This work provides expand our comprehension of the environment inside gas giants, demonstrating that that metallic hydrogen is a good solvent for silica at megabar pressures for temperatures above 5000 K. This result is consistent with recent ab initio solubility calculations that predicted H_2O to dissolve into metallic hydrogen at 2000 to 3000 K [22] and MgO at 6000–8000 K [21]. This suggests other insulating materials may dissolve at a comparable temperature range. We have assumed that there is sufficient hydrogen available for the approximation of noninteracting solute atoms to remain valid. Also, other stoichiometries of SiO_2 have not been considered, assuming Si and O to dissolve in a one-to-two ratio according to the charge balance. Iron was found to dissolve at low temperatures because it is a metal [49]. Since all materials that have been analyzed up to date dissolve into metallic hydrogen, it suggests that hydrogen will spontaneously react with any material that is used as confinement during dynamic shock wave experiments that reach megabar pressures and high temperatures. Our findings indirectly place a limit on the time scale of such experiments before a significant contamination of the sample sets in.

Chapter 5

The Melting curve of Silica

The objective of this thesis is to understand how the properties of materials are affected by pressure and what is their impact on the evolution of solar and extrasolar planets. In chapter 4, we have reviewed the importance of silica as a key mineral for gas giant planets formation, and realized that it can be dissolved from their rocky core by metallic hydrogen. We also realized that silica was liquid beyond 20000 K at 20 Mbar, but since no studies of the melting behavior of silica has been performed for this regime, we had no clue of the stability of the Fe_2P phase of silica in this context. Establishing the boundary between solid and liquid silica in the pressure–temperature diagram will provide more information for planetary models, and increase our understanding regarding the considerations that must be taken into account when studying the interior of massive rocky planets, like super-Earths, and gas giants. Thus, this chapter focuses the attention on the melting curve of silica for the highest pressures ever reported, presenting the melting curve of SiO_2 up to 6000 GPa (60 Mbar) and covering the range of pressures and temperatures that exist at the interiors of gas giants and massive super-Earths. According to our ab initio simulations, silica, if present, is in solid state in the core of all gas giants of our Solar System.

5.1 Introduction

The quest for extrasolar planets has revealed hundreds of worlds of different classes, inspiring novel concepts about planetary formation and composition [60]. Hundreds of gas giants and super-Earths have been found among them in the last decade [2,61], providing enormous datasets of their atmospheric composition, size and mass. Estimating the internal composition of these planets is based on planet's mass to radius relationships that relies heavily on equations of state (EOS) of materials like hydrogen, helium, "ices" such as water, ammonia, methane and silicate rocks [62–64], which are calculated from electronic structure theory and sometimes measured experimentally on Earth. In this sense, the giant planets resemble natural laboratories for studying the behavior of materials at high pressure and temperature [35], which typically reach values outside the realm of experiment on Earth. This leaves theoretical approaches, such as ab initio calculation, as our only window to understand the properties of matter in these extreme regimes [63].

The models for planetary interiors are constrained by the bulk composition and distribution of certain chemical species, particularly silicates, which are among the most common rock-forming elements [65, 66]. Robust models need to include the EOS for perovskites, magnesiowustites and silicates, and more specifically their phase transitions and melting curves at high pressures. Approximations like uniformlow temperature for the whole planet are used as a practical simplification when modeling rocky planet interiors because the full temperature-dependent EOSs for the materials of interest are either unknown or highly uncertain at the temperatures massive solid planets can reach in their interiors and in the pressure range beyond the reach of static compression experiments ($\lesssim$300 GPa) and the analytical high-pressure laws of plasma physics (10000 GPa) [62]. Such knowledge would allow us to predict, for instance, whether the lowermost mantles of super-Earths, whose bulk composition consist of silicates, can easily melt or not [11,31,45] and the influence of silica on the existence of liquid cores [67]. In this context, the phase diagram of silica becomes fundamental. Currently, the melting curve for silica is known only up to 200 GPa (2 Mbar) [48]. To our knowledge, no calculations have been reported for the so called "multimegabar regime" ($\geqslant$ 1000 GPa), which corresponds to the conditions found in the core of many giant planets and some super-Earths [47]. The extreme pressure and temperature conditions prevalent in giant planet core–mantle boundaries (8000–12000 K and 800–1800 GPa for Saturn, 18000–21000 K and 3500–4500 GPa for Jupiter) and supermassive exoplanets, are not yet obtainable in the laboratory.

On the other hand, the melting process is probably one of the most complex phase transitions in Condensed Matter Physics in terms of basic understanding of its origins and mechanism. It is a critical process that is responsible for both the formation of the iron-rich core and volcanism of rocky planets that transfers gases dissolved in the mantle to the atmosphere [68]. Experiments can only give indirect evidence of melting by characterizing the atomic neighborhood through diffraction, for example, but cannot track the atoms position while a solid is melting. On the other hand, standard molecular dynamics simulations allow us to track the trajectory of each atom, giving a detailed information about the process of melting, to decide when the crystalline lattice has became a liquid. However, it is well known that if a crystal is heated in a completely homogeneous way, it can reach temperatures above the melting temperature T_m without melting, a phenomenon known as overheating.

Lindemann [69] gave an estimation of the melting temperature in terms of the vibration amplitud of atoms, establishing that the melting process starts when the amplitude of vibration of each atom from its position in the crystalline structure becomes so large that it begins to "invade the space" of its nearest neighbors. Assuming a single frequency of vibration ν for all atoms (the Einstein approximation) and using the equipartition theorem from Statistical Mechanics, the melting temperature can be obtained by

$$k_B T_m = 4\pi^2 \nu^2 m f a^2, \tag{5.1}$$

where m is the atomic mass, a is the distance between nearest neighbors and f is Lindemann's allowed threshold of vibration, such that the mean square displacement of each atom is given by $\langle r(t)^2 \rangle = f a^2$.

Another rough criterion to estimate the melting temperature was postulated by Born in 1939 [70]. He assumes that melting is produced at a point when the crystal completely loses its resistance to shear stress, becoming mechanically unstable and then collapsing into a disordered liquid structure. It is usually assumed that the C_{44} elastic constant is the first to vanish with temperature, and in this case the condition for T_m is simply,

$$C_{44}(T_m) = 0. \tag{5.2}$$

However, both the Lindemann and Born criterion have shown to fail in fundamental ways by molecular dynamics, since they are a very simplified view of the melting process which do not take into account the cooperative nature of the process. In particular, neither the Lindemann nor Born criteria conditions are fulfilled when the liquid starts to nucleate, triggering the melting process, while for a finite crystal, where the melting process starts at a temperature lower than the one needed to make the shear resistance equal to zero, the Born criterion is not fulfilled.

Some techniques have had to be developed for molecular dynamics in order to overcome the overheating problem and predict more accurate melting temperatures, which have been extremely successful in determining the melting curve of various materials. Two of the most common approches to calculate melting curves are described in computational methodology, known as two–phase simulations and Z method.

5.2 Previous work and motivation

Ab initio techniques like DFT have been extremely successful in determining the stable structure of various materials. They have allowed scientists to confirm and make interpretation of the diffraction patterns seen in experiments, or predict new phases not previously seen, and to identify the phase boundaries where phase transitions take place. For instance, it has been determined that $MgSiO_3$ becomes unstable and dissociates in the cores of gas giants and terrestrial exoplanets [47], leaving SiO_2 and MgO as separate compounds that form the rocky interior of these planets. In the case of silica, its ambient phase, quartz, is a fourfold coordinated, hexagonal structure with nine atoms in the primitive cell [71]. At higher pressures there are a number of denser phases. The mineral coesite, also fourfold coordinated, is stable from 2–7.5 GPa, and has a large, complex structure, which is a 24 atom monoclinic cell [72]. Further compression transforms coesite to a much denser, sixfold coordinated phase called stishovite, stable up to pressures near 50 GPa. Stishovite has a tetragonal primitive cell with six atoms [73]. In addition to the coesite–stishovite transition, quartz metastably transforms to stishovite at a slightly lower pressure of about 6 GPa. Near 50 GPa, stishovite undergoes a ferroelastic transition to a $CaCl_2$-structured polymorph via instability in an elastic shear constant [74, 75]. This transformation is second order and displacive, where motion of oxygen atoms under stress reduces the symmetry from tetrahedral to orthorhombic. Stishovite and poststishovite phases of silica, in particular, are geophysically important due to its wide range of stability in the mantle, the possible chemical reactions of silicates with liquid Fe at the Earth's core–mantle boundary (CMB) and its presence in impact craters [76] and meteorites [77]. Experiments and computations [77–79] have reported a further transition of the $CaCl_2$-structure to an α-PbO_2-structured polymorph at pressures near the base of Earth's mantle. Above 250 GPa, a tranformation to a pyrite structure takes place, a 5% denser phase in which the silicon coordination number increases from 6, in the α-PbO_2, to 8 [43]. This number is increased to 9 in the cotunnite (α-$PbCl_2$) phase, that takes place at 700 GPa [47, 79]. The first evidential result of a pressure-induced phase transition to the Fe_2P-type structure was reported by Tsuchiya [46] in 2011. The crystal structure consists of closely packed, fairly regular SiO_9 tricapped trigonal prisms with a significantly compact lattice, being the stable structure of silica at the highest pressures ever reported.

Studies about the melting of silica have been carried out through experiments and MD simulations by many authors [40, 44, 48, 80–83]. The melting curve is extended to higher pressures as new phases are discovered, but no studies about melting have been performed for phases beyond the α-PbO_2 phase (160 GPa), where the pyrite, cotunnite and Fe_2P become the stable phases.

5.3 Computational Methodology

The aim of this chapter is to determine the melting curve of silica for high pressures. We have chosen the Z method, which has received a lot of attention in the recent years and seems to be a promising method for calculating melting curves of materials, since it allows to reduce the amount of atoms required to perform the simulations, compared to the two-phase coexistence method, by using a single phase. Both methods are explained below.

5.3.1 Two–phase simulations

A common, simple and widely used approach in atomistic simulations to determine the melting temperature of a substance at a giving pressure (melting point), is the two–phase simulation technique [82, 84–86]. Its main idea is the direct simulation of coexistence of the two phases, liquid and solid, at a given temperature and pressure (NPT ensemble). The simulation cell is divided into two halves, one is filled with atoms arranged in a solid structure and the other with atoms from a liquid simulation of the same system, both at the same density. If we perform NPT molecular dynamics on this composite system for sufficiently long times, we can find upper and lower bounds for T_m at the chosen pressure: if the applied temperature is lower than T_m, the solid phase will start to grow, finally filling the whole simulation cell (the liquid half freezes). If the temperature is higher than T_m, the liquid phase fills the cell instead (the solid half melts). This technique has been used extensively on different kinds of materials, but requires a large amount of atoms (enough for both liquid and solid halves), and a large amount of simulation steps, which is a common problem with the melting process. Sometimes a classical potential is fitted to an ab initio simulation [87] in order to be able to simulate larger systems, but this may introduce undesirable effects that may result in a different melting curve to that one obtained by pure ab initio simulations.

5.3.2 Z method

This novel method has recently received a wide application in melting studies [88–106]. and does not require the coexistence of two phases. Based on the microcanonical ensemble, this method relies on the fact that there is a maximum energy E_{LS} which a solid of N atoms confined to a volume V can have, before tranforming completely into the liquid state. This defines a critical temperature, known as the limit of superheating, and denoted by T_{LS}, above which the crystalline structure cannot survive. A system simulated in the NVE ensemble slightly above T_{LS} will melt, its temperature dropping naturally to T_m at the pressure fixed by the chosen density.

The idea is giving different initial energies to a crystal with a defined volume (different initial temperatures) and plotting the temperature against energy or pressure. The locus of points will be an isochore in the T-P and T-E diagram, which will have a Z shape, as shown in figure 11.

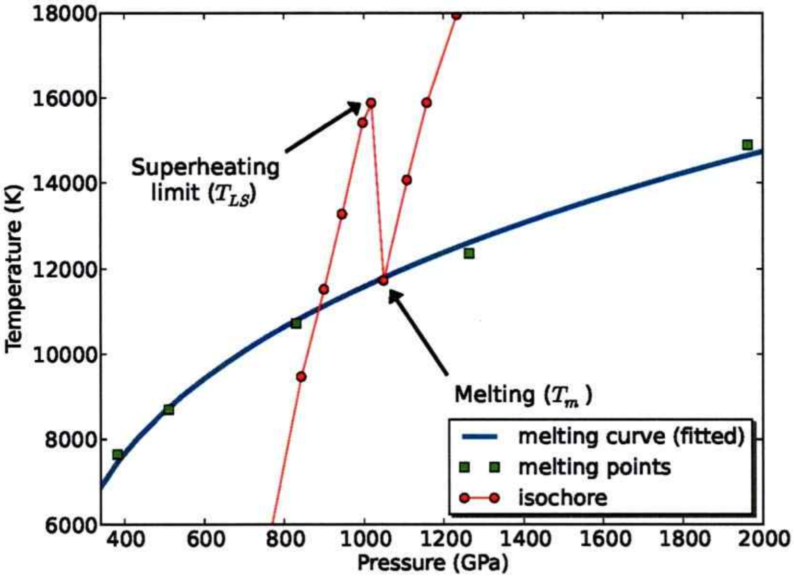

Fig. 11: Example of an isochore in Z method, used to determine the melting temperature in the microcanonical ensemble. The left branch correspond to simulations of the system in solid state, and extends up to the superheating temperature T_{LS}, where the system has an energy E_{LS}. Then, with an energy slightly higher, the equilibrium temperature drops to the melting temperature T_m.

5.3.3 DFT Calculations

We used the same PAW pseudopotentials with the PBE exchange-correlation functional for silicon and oxigen that were used for the calculation of the solvation energy in the previous chapter. The time step used for all MD simulations was of 0.2 fs. The simulations were found to be well-converged within a time of 1 ps. A cutoff energy of 900 eV for the plane wave expansion of the wavefunctions was chosen. More than 10 constant energy simulations of 1 ps were performed for different volumes, until we get a defined slope in the liquid and solid branches.

We used the Z method to obtain the melting points. No fictitious forces or rescaling of velocities were introduced in order to keep a constant temperature, since the simulations are performed in the microcanonical ensemble. Since long waiting times are required in the Z method for the system to melt when it is overheated [88], in which cases the temperature drops to another equilibrium temperature during the simulation, we are not able to know what the melting temperature of the system is for sure. Therefore, we made corrections of the melting temperatures according to a Bayesian analysis, as described in [101], in order to infer the melting point and its uncertainty from the simulation data.

Crystal structures We used three high-pressure phases of silica: the Fe_2P-type structure, and the previously known cotunnite-type and pyrite-type structures. The supercells used contain 72 atoms in the case of Fe_2P phase, and 96 in the case of pyrite and cotunnite. A Γ-point sampling for the Brillouin zone was used for the pyrite and Fe_2P structures, while a $1 \times 1 \times 2$ k-point mesh was used for the case of cotunnite-type SiO_2.

5.4 Results

The following section presents the results comparing the melting points obtained for the three structures of silica chosen, namely, pyrite-, cotunnite- and Fe_2P-type silica.

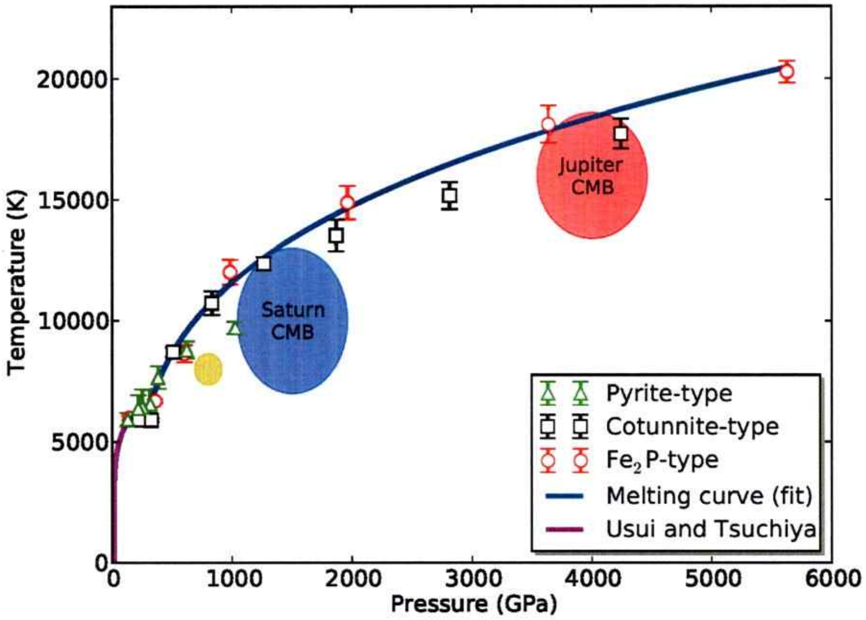

Fig. 12: **SiO_2 melting curve**. Green triangles, black squares and red circles represent the melting conditions for the pyrite, cotunnite and Fe_2P structures of silica. The fitted SiO_2 melting curve is shown as a blue solid, thick curve. The magenta thick curve corresponds to the melting curve of SiO_2 at lower pressures, predicted by Usui & Tsuchiya using two-phase MD [48] method. The yellow area corresponds to the core–mantle boundary conditions (CMBs) for Uranus and Neptune, while the blue and red areas correspond to the CMB conditions of Saturn and Jupiter, respectively [60]. Errors bars indicate the uncertainty in the melting temperature computed by the Bayesian procedure.

Figure 12 shows the melting curve of SiO_2 for an ultra-high pressure regime, up to 6000 GPa. The symbols represent the calculated melting point for pyrite (triangles), cotunnite (squares) and Fe_2P (circles). Errors bars indicate the uncertainty in the melting temperature computed by the Bayesian procedure [101]. At low pressure ($\sim$ 300 GPa) pyrite points are above the other two phases. Then, at slightly higher pressure ($\sim$ 500 GPa) cotunnite overcomes pyrite. Finally, in the high end pressure range, Fe_2P points are above the others. In order to draw the solid–liquid boundary, we chose the more stable phase, that is, the structure corresponding to the higher melting temperature at a given pressure. The melting curve thus obtained, and fitted accordingly [107], corresponds to the blue line in figures 12 and 13.

The range of pressures and temperatures covered by the calculated melting curve is relevant for giant planet interiors. Although the pressures present at the Earth's deep interior are about a few megabar ($\sim$ 300 GPa), some super-Earths might overcome this limit and have core–mantle boundary conditions around and above 1000 GPa [47]. Moreover, the pressures reached at the rocky core of giant planets might exceed 4000 GPa. Our results show that the silica melting curve lies above the core–mantle boundary of the giant planets of our solar system. Thus, silica is expected to be in solid state at the very interior of these planets. This is in perfect agreement with the calculations of the solubility of silica in metallic hydrogen performed in chapter 4, where silica was found to be liquid at 2000 GPa and 20000 K [108].

Figure 13 shows a zoom of the SiO_2 melting curve between 0 and 1500 GPa. We observe that a discontinuity in the slope of the curve occurs at 330 GPa, independent of which initial structure is used (pyrite, cotunnite or Fe_2P). The PbO_2–pyrite boundary has been estimated at 200 GPa [46]. The picture that emerges from our results is that the stability region of pyrite extends up to 480 GPa, at which point it is replaced by cotunnite. Considering the Clausius–Clapeyron equation $dP/dT = \Delta S/\Delta V$, and taking into account that at high pressure $\Delta S \approx k_B \ln 2$ [109], the change in the slope of the melting curve at around 480 GPa is indicative of a volume reduction of

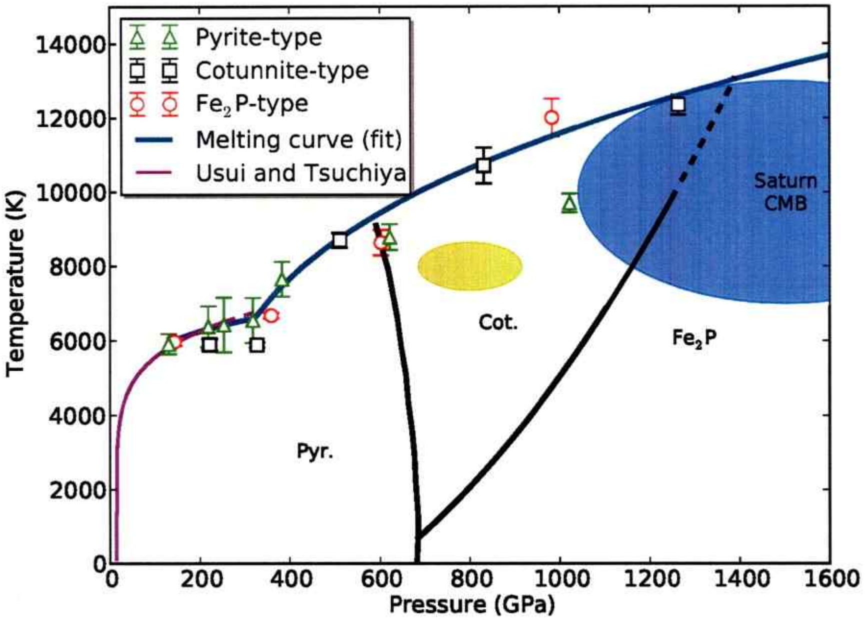

Fig. 13: **SiO_2 melting curve**. The legend is the same as figure 12. Black lines indicate the solid-solid phase boundaries according the calculations of Taku Tsuchiya and Jun Tsuchiya [46]. The dashed, black line is an extension to the cotunnite–Fe_2P boundary predicted by them using a cubic fit, in order to reach the melting curve calculated in this work. The dashed magenta line is an extrapolation the SiO_2 melting curve predicted by Usui & Tsuchiya [48], with overlaps with our melting curve. The green line represents the calculated MgO melting curve reported by Boates [41] for comparison.

$\Delta V \approx 0.114$ Å^3 per SiO_2 unit. The stability of the cotunnite phase ends at 900 GPa, where the Fe_2P type phase begins. Thus, our simulation suggests that the boundaries of the cotunnite phase occurs between 480 and 900 GPa and that at higher pressures, the stable phase is Fe_2P. A previous study by Tsuchiya et al. [46] used MD and meta-dynamics simulations to estimate the pyrite-cotunnite boundary at low temperature around 650 GPa. The extension of this boundary to high temperature intersects with our melting curve at 600 GPa (figure 13), generating a pyrite–cotunnite–liquid triple point. An extrapolation of their cotunnite-Fe_2P boundary hints at another triple point around 1400 GPa. However, according to our results, both triple points occur at lower pressures than predicted by Tsuchiya et al. This suggest a displacement of both solid-solid boundaries but, as in their case, it also confirms that the stability range of the cotunnite phase increases with increasing temperatures.

Finally, an analysis of the melting curves for MgO and SiO_2 might be very useful to predict whether the interiors of gas giants consist of stable rocky cores, if both materials are present within them. We used the MgO melting curve published by Boates et al. [41], up to 600 GPa, which we compared to our obtained SiO_2 curve (figure 13). It is clear that all the MgO values remain above those of SiO_2 for the points shown in figure 13. Although the MgO melting curve remains unknown for pressures higher than 600 GPa, it has been reported that no further solid-solid transitions take place up to 4000 GPa [21]. It is quite possible, then, that MgO melting curve may continue to increase monotonically, staying always above the SiO_2 values, up 1600 GPa (figure 13).

5.5 Astrophysical Implications

Our results have important implications for the interior of super-Earths. The interior of supermassive rocky planets, such as CoRoT-7b, CoRoT-3b, Kepler-10b and GJ 1214b, exhibit pressures that can easily exceed 1000 GPa [63,110], where magnesium perovskite dissociation is promoted and the properties MgO and SiO_2 become relevant. We predict that the SiO_2 component will remain as an stable rocky component in the deep interior of super-Earths, since beyond 700 GPa, a temperature greater than 10000 K is needed to melt it, which is too high for the interior of a rocky planet [13]. Since planets with mantles have hotter interiors due to their insulating character, the knowledge of the melting point of rocks becomes crucial. Studies about the melting behaviour of post-perovskite and MgO at these pressures must be performed since, coupled to our results, they could finally clarify if the lower-most mantle of super-Earths can easily melt or not [11, 31, 68] and give valuable information to the study of plate tectonics, where the inclusion of melts significantly impacts cooling and modulates hence the thermal evolution [111, 112].

Formation of magma oceans is also dependent on the melting properties of rocks, like silica. The difference between the melting temperature of silicates and the geotherm of a planet becomes more significant in planets with high surface gravity, since the pressure increases more rapidly with depth than on Earth, like in CoRoT-7b, where the surface gravity is 22.4 m s^{-2} [67]. The abrupt increase in the slope of the SiO_2 melting curve obtained in this study confirms the assumption that the temperatures found through the deep mantle are not high enough to allow the silicates to be stable in a liquid state at depth if they are not already molten at the surface. As a consequence, there should be no underground oceans, or even large magma reservoirs, on the planetary scale [67].

On the other hand, the conditions at the interior of giant planets lies in the megabar to gigabar pressure range, at temperatures on the order of 10^4 K [35] which, according to our study, is just the region where silica is expected to melt. This is an interesting scenario, since the rocky core of gas giants with interiors hotter than Jupiter, but with similar pressures at the core–mantle boundary, may partially melt their core, with substantial implication in the evolution of the planet; while larger gas giants, with higher inner pressures, should at least have a solid silica component. In the case of the gas giants of our Solar System, silica is expected to be in solid state in their core, as shown in figure 12, although this does not mean that the core remains stable, since it can be affected by the solvation effect of metallic hydrogen as demonstrated in chapter 4.

5.6 Conclusions

We have presented the SiO_2 melting curve by using ab initio calculations and the Z method, up to 6000 GPa and 20000 K. The results allow us to determine the regions in which this important component of the mantle of rocky planets and of the core of gas giants can become liquid, providing constraints in the studies of these bodies that allow more precise frameworks to understand their evolution. We have also estimated that the pyrite-cotunnite phase transition at the melting point may happen at 480 GPa, while the cotunnite-Fe_2P transition may take place at 900 GPa. This promotes further studies of the solid-solid phase transitions of silica in order to determine more precisely where are the boundary for these high pressure phases.

The reliability of our calculations, though, depends on the exchange-correlation functional used. LDA and GGA have shown differences in the predicted melting temperatures [113]. However, in spite of this choise, or the grid of the Brillouin zone used, or the amount of atoms used to get more precise results, we believe that it is very unlikely for DFT to be so much in error in the present case, since an error bar of approximately 1000 K or more should always be considered to be uncertainties of the conditions found inside planets, and whether experiments may confirm our results or not in a near future, the trend of our curve will not be very different from the one obtained by other methods.

Chapter 6

Mechanical instability of body-centered cubic iron at Earth-core conditions

The solid inner core of Earth was discovered in 1936 [114] and, with a radius of 1220 km (see figure 14), is thought to consist almost entirely of iron [115], with less than 10 weight percent alloying elements. Clarifying the phase diagram of iron therefore has important implications for understanding the structure and origin of the inner core, and the energy sources that drive the geomagnetic dynamo. Precise knowledge of structure of iron at inner core conditions is essential for explaining the seismologically observed pattern of the inner core's seismic anisotropy, with longitudinal PKIKP waves travelling 3% faster in polar (along the rotation axis) than equatorial directions [116]. In this chapter we review theoretical evidence pointing to *bcc* iron being unstable at 300–1500 GPa based on first-principles calculations, both for the static lattice and via molecular dynamics. The strongest arguments for high temperature stabilizing *bcc* Fe come from studies using classical many-body potentials or weak requirements of mechanical stability in ab initio simulations, such as hydrostatic stress, a situation that does not occur in a free energy minimum only;

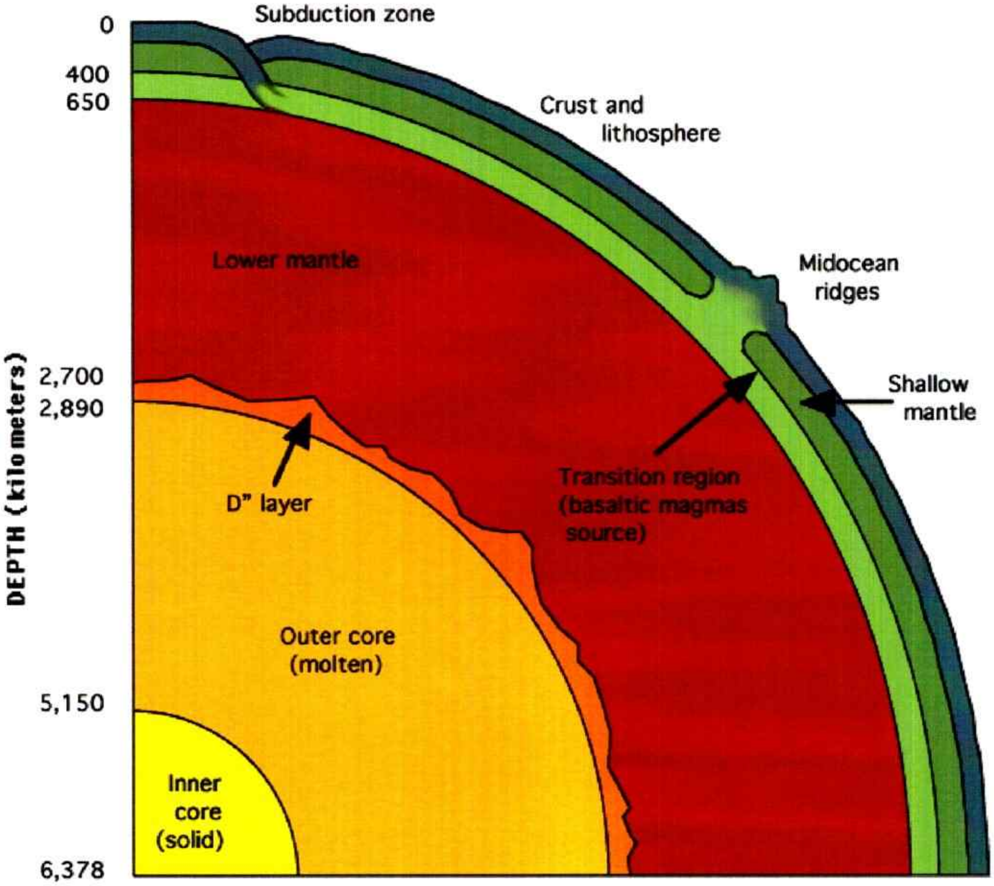

Fig. 14: Interior of planet Earth, showing the different layers and the solid inner core. Image from www.solarviews.com.

but also in a local maximum, where the structure can be unstable under tetragonal strain. We show that despite of taking into account tetragonal distortions in the *bcc* cell, it is still possible to erroneously find stability of *bcc* Fe at Earth's core conditions if the accuracy and convergence are not fulfilled. We find, from fully converged and highly accurate ab-initio calculations, that *bcc* phase of Fe is unstable at Earth inner core (around 300 GPa) for temperatures in the 5500–7000 K range. Ironically, recent theoretical work shows that, at zero temperature, the *bcc* structure is in fact stabilized again at much higher pressures, above 20 TPa (200 Mbar); however, this is because of the engagement of core electrons in the interatomic bonding of iron [117, 118]. Thus, both theory and experiments [119–124] confirm that Fe forms in a close-packed structure at the conditions of Earth-like planetary interiors. The chapter starts with an introduction to the significance of iron for planetary science and goes over previous theoretical work and challenges. We review some criteria to deterime stability and suggest new ones. In the final section, the possibility of having a *bcc* phase for iron at higher temperatures and densities is discussed.

6.1 Introduction

There has been longstanding controversy about the stable crystalline phases of iron at conditions of Earth's inner core, 329–364 GPa (5150–6371 km depth) and ~ 5500 (± 1000) K [125], and at high pressures in general, with claims that at the center of Earth the body-centered cubic (*bcc*) structure may be stable at temperatures close to the iron melting point [126–139], which has been estimated to be 6700 K [18] at these pressure conditions. The theoretical rationale is that entropy associated with atomic vibrations might stabilize the *bcc* relative to close-packed structures at combined high pressures and temperatures. Recent experiments [110, 120, 122, 123, 140, 141] do not reveal evidence for the *bcc* phase at these conditions, but instead point to the hexagonal close-packed (*hcp*) structure being stable. These results have implications for disciplines ranging from applied physics and engineering to the geophysics of planetary cores. In particular, the discovery of large numbers of extrasolar planets provides motivation for understanding the properties of Fe – a key planetary core-forming element – at high pressures and temperatures [11, 13, 49, 62, 142, 143].

The elastic constants of the *hcp* phase of iron, combined with plausible mechanisms for producing lattice preferred orientation in polycrystals, are capable of explaining the seismic anomaly. However for the cubic phases of iron (*fcc* and *bcc*) which also are elastically anisotropic, the pattern of anisotropy is very different and no plausible mechanism has been advanced to explain the dominant pattern of inner-core anisotropy in terms of a cubic polycrystal [144, 145]. Mechanical and thermodynamic stability in iron is strongly influenced by pressure, temperature and composition. The *bcc* phase of iron, the stable polymorph near ambient conditions, transforms to a hexagonal close-packed phase near 10 GPa, and becomes mechanically unstable at higher pressures and low temperatures [146]. Nevertheless, there have been persistent arguments that the stable phase of iron at inner-core conditions is *bcc*. The strongest arguments for a mechanically stable *bcc* phase at high pressures and temperatures come from theoretical calculations (ab initio and classical-potential based molecular dynamics simulations) [131, 136–138]. These past studies suffered from limited reliability of classical many-body potentials, the accuracy of which is untested in studies of the mechanical instability of *bcc* iron, and also from focusing on the hydrostatic nature of the stresses for inferring mechanical stability. However, hydrostatic equilibrium inferred from inspection of stresses does not need to correspond to a free energy minimum; it can instead be due to a local maximum, with the unit cell metastable with respect to a finite tetragonal strain. On this last point, Vočadlo *et al.* [132] ab initio free-energy calculations for the *bcc* phase do consider tetragonal distortions, and using a 128 atoms cell, they find *bcc* Fe becoming mechanically stable above 6000 K at Earth-core density (vs. 4500 K found in a previous paper [130]). However, this study lacks the necessary accuracy and convergence. Similarly, Bouchet, et al. [139] work is inadequate in using hydrostatic equilibrium to determine mechanical stability of the *bcc* structure. Using thermodynamic integration based on first-principles molecular dynamics simulations, Cui *et al.* [147]

analyzed the combined effects of high temperature and impurities on the stability of *bcc* structure of iron with respect to tetragonal strain at Earth inner core pressures. Based on their results for temperatures close to 7000 K they find that although the small amount (6.25 at.%) of silicon or sulphur increases the stability of *bcc* phase it fails to achieve the complete stability. Contrary to these studies, we find from more accurate and fully converged ab initio calculations, that the *bcc* phase of Fe is unstable to temperatures of 7000 K at inner-core densities.

We have carried out studies for the mechanical stability of *bcc* phase under tetragonal and, reported for the first time, orthorhombic strains, employing 128 and 180 atoms cells, respectively, using a $2k$-point mesh in each case, which provides much better accuracy not studied so far. Our fully converged calculations carried out over 10 ps demonstrate the instability of *bcc* phase under tetragonal and orthorhombic distortions beyond the temperature of 6000 K.

6.2 Computational Methodology

Electronic-structure based total-energy calculations were carried out using the projector augmented-wave (PAW) method as implemented in VASP [55, 148], based on density-functional theory (DFT) with the generalized-gradient approximation (GGA) of Perdew, Buke and Ernzerhof (GGA-PBE) [56]. The PAW is closely related to the ultra soft pseudopotential method, and gives results that agree with those of all-electron methods. The $3p$ and $4s$ semi-core electrons were taken in their valence configuration in generating the pseudopotential, and an energy cutoff of 350 eV was used for the plane-wave expansion. The simulations are confined to the Born-Oppenheimer surface, and the effect of finite temperature on the electronic structure is included through Mermin's formalism [58]. We implemented an

$18 \times 18 \times 18$ Monkhorst-Pack k-point mesh [57], and Brillouin-zone (BZ) integration was carried out with the linear tetrahedron method [149].

Tetragonal distortions

For tracking the structural transformation from body-centered cubic (*bcc*) to face-centered cubic (*fcc*), known as the Bain path transformation [150], we used a body-centered tetragonal cell (*bct*, space group I4/mmm) at the volume of 7.2 Å^3/atom, a cell which is able to represent both *bcc* and *fcc* structures by means of a tetragonal distortion of the cell vectors (see table 6.1). The same volume was preserved for every distortion performed.

Structure	b/a	c/a
bcc	1	1
fcc	1	$\sqrt{2}$
fcc	$\sqrt{2}$	1
fcc	$1/\sqrt{2}$	$1/\sqrt{2}$

Table 6.1: Unit cell values for *bcc* and *fcc* in a tetragonal cell with cell vectors **a**, **b** and **c** (*bct*, space group I4/mmm).

Orthorhombic distortions

For the *bcc*-*hcp* transition path under orthorhombic distortions we used an orthorhombic cell with 4 atoms (space group *Cmcm*, lattice vectors **a**, **b** and **c**) and placed Fe atoms at the 4c Wyckoff positions: $(0, y, 1/4)$, $(0, -y, 3/4)$; $(1/2, 1/2 + y, 1/4)$, $(1/2, 1/2 - y, 3/4)$ [151, 152]. This cell is able to accomodate *fcc*, *hcp* and *bcc* structures and we allowed for changes in the cell shape (but not in volume) and relaxation of internal degrees of freedom. When $y = 1/4$, this cell corresponds to a face-centered tetragonal (*fct*) cell if $b/a = 1$, being able to transform from *bcc*

($c/a = \sqrt{2}$) to *fcc* ($c/a = 1$). We get *hcp* choosing $b/a = \sqrt{3}$ and $c/a = \sqrt{8/3}$ for $y = 1/3$ (see table 6.2).

Structure	y	b/a	c/a
bcc	1/4	$\sqrt{2}$	$\sqrt{2}$
fcc	1/4	1	1
hcp	1/3	$\sqrt{3}$	$\sqrt{8/3}$
opt. *hcp*	1/3	$\sqrt{3}$	1.593449

Table 6.2: Unit cell values for *bcc*, *fcc*, *hcp* and optimized *hcp* in orthorhombic cell with cell vectors **a**, **b** and **c**, and atoms in the 4c Wyckoff positions of the space group *Cmcm*.

Molecular dynamics

For molecular dynamics simulations, we used the NVT ensemble (N, number of atoms; V, volume; T, temperature), with a Nosé thermostat [153] and supercells containing 128 (4×4×4 *bct* unit cells) and 180 (5×3×3 orthorhombic unit cells) atoms for tetragonal and orthorhombic distortions, respectively. We sample the Brillouin zone on a $2 \times 2 \times 2$ k-point mesh, and assume thermal equilibrium between ions and electrons via the Mermin functional [58] (i.e., we set the electronic temperature $T_{el} = T$). The calculations were carried out for volume of 7.2 Å^3/atom for temperatures varying from 5500 to 7000 K. Using a time step of 1 fs, we find that 15000 time steps (≈15 ps) yield converged values of the stress tensor, with the final 10 ps used for accumulating averages. The uncertainty in the components of the stress tensor due to thermal fluctuations is evaluated with the blocking method [154]. Although possibility of magnetism is considered in recent paper by Ruban et al. [155], all our calculations are based on PAW approach described above and are non-spin polarized, as previous calculations have shown that the phases of iron are non-magnetic for the pressure-temperature conditions we have considered [130, 146].

6.3 Results

6.3.1 Static Electronic Structure Calculations ($T = 0$)

The total energy was calculated for both tetragonal and orthorhombic distortions by varying c/a as well as b/a, keeping a constant volume of 7.2 Å^3/atom (equivalent to a pressure of ∼300 GPa). In figure 15 we show the energy surface obtained from electronic structure calculations at $T = 0$ K for tetragonal distortions. Under tetragonal distortions, the *bcc* phase occupies a local energy maximum at $b/a = c/a = 1$, and the minima, corresponding to the *fcc* phase, are located at $c/a = \sqrt{2}$, $b/a = 1$; $c/a = 1$, $b/a = \sqrt{2}$; and $c/a = b/a = 1/\sqrt{2}$ (see table 6.1). The *bct* structure is located at a saddle point at $c/a = 0.9$ and $b/a = 1.0$, from which the total energy decreases as the b/a ratio is changed. An energy surface with similar topology is

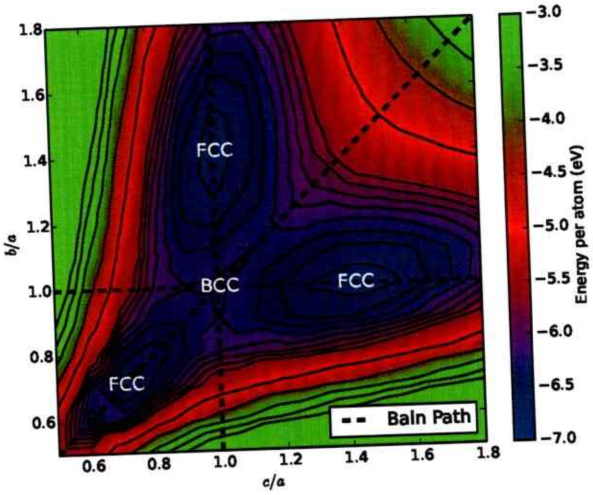

Fig. 15: Energy surface obtained from electronic structure calculations for static ions, using tetragonal (*bct*) cell at 7.2 Å^3/atom and electrons at $T_{el} = 0$ K. At this volume, the pressure is ∼300 GPa. The black dashed lines indicate the *bcc*-*fcc* Bain paths, and the labels show how *bcc* structure is located in a saddle point, while *fcc* is located at local minima.

well known in other transition metals [156], including in iron from a tight-binding model [157]. Our energy surface agrees with a recent ab initio re-determination of the b/a-c/a energy surface [158].

Total energy calculations along *bcc*-*hcp* path using orthorhombic cell (see table 6.2) further reveal stability of the *fcc* ($b/a = c/a = 1$) and *hcp* ($b/a = \sqrt{3} \approx 1.732$, $c/a = \sqrt{8/3} \approx 1.632$) structures, as shown in figure 16. The *bcc* structure ($b/a = c/a = \sqrt{2}$) is clearly unstable but lies close to the energy minimum defining the stability region of *hcp*. Thus the electronic-structure-based total-energy calculations for static ions document the stability of close-packed (*hcp* and *fcc*) structures, in contrast to the *bcc* phase that is seen to be unstable under both tetragonal and orthorhombic distortions.

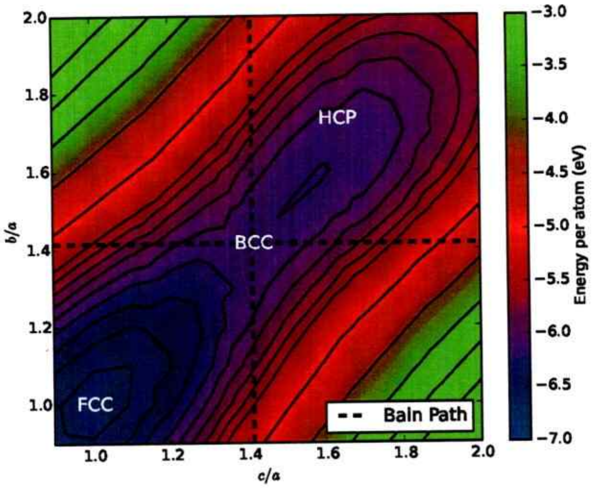

Fig. 16: Energy surface obtained from electronic structure calculations for static ions, using the orthorhombic cell at 7.2 $\mathrm{\AA}^3$/atom and electrons at $T_{el} = 0$ K. At this volume, the pressure is 300 GPa. We notice the stability of *fcc* and *hcp* structures, located in energy local minima, respect to the *bcc*, located in a saddle point and, therefore, unstable.

6.3.2 Molecular Dynamics Simulations

To study the effect of temperature on the structure at this pressure (300 GPa) we performed ab initio molecular dynamics (AIMD) simulations in the 5500–7000 K temperature range for tetragonal strains, as explored by other authors [132, 135], and orthorhombic strains, which have not been explored before. AIMD is more time consuming than molecular dynamics based on semi-empirical classical potentials, but has the important advantage of making no *a priori* assumptions concerning the the nature of the charge density, electronic structure or bonding.

For tetragonal distortions (128 atoms supercell, $4 \times 4 \times 4$ *bct* unit cells) we chose four c/a values along the Bain path, from 0.95 to 1.2, shown in table 6.3.

Point	Supercell vectors			Ratios	
	4a	**4b**	**4c**	b/a	c/a
1st	(9.8993,0,0)	(0, 9.8993,0)	(0,0,9.4044)	1.00	0.95
2nd (*bcc*)	(9.7315,0,0)	(0, 9.7315,0)	(0,0,9.7315)	1.00	1.00
3rd	(9.5745,0,0)	(0, 9.5745,0)	(0,0,10.0533)	1.00	1.05
4th	(9.1577,0,0)	(0, 9.1577,0)	(0,0,10.9893)	1.00	1.20

Table 6.3: Tetragonal distortions. Lattice vectors corresponding to different values of c/a, the second point ($b/a = c/a = 1$) corresponding to the *bcc* lattice. Volume per atom: 7.2 Å^3.

For orthorhombic distortions (180 atoms supercell, $5 \times 3 \times 3$ orthorhombic unit cells) we chose four points: A, B, C, and D, defined in table 6.4. Point A ($b/a = 1.45$, $c/a = 1.42$) is close to *bcc*, while B ($b/a = 1.50$, $c/a = 1.45$) and C ($b/a = 1.573$, $c/a = 1.523$) are distorted towards *hcp* ($b/a \approx 1.73$, $c/a \approx 1.63$). Point D ($b/a = 1.135$, $c/a = 1.125$) corresponds to distortion towards *fcc*. An schematic representation of these points is shown in figure 17.

Point	Supercell vectors			Ratios	
	5**a**	3**b**	3**c**	b/a	c/a
A	(12.0471,0,0)	(0, 10.4810,0)	(0,0,10.2641)	1.450	1.420
B	(11.8290,0,0)	(0, 10.6461,0)	(0,0,10.2912)	1.500	1.450
C	(11.4540,0,0)	(0, 10.8102,0)	(0,0,10.4667)	1.573	1.523
D	(14.1270,0,0)	(0,9.6205,0)	(0,0, 9.5357)	1.135	1.125
fcc	(15.3262,0,0)	(0,9.1957,0)	(0,0,9.1957)	1	1
bcc	(12.1644,0,0)	(0,10.3218,0)	(0,0,10.3218)	$\sqrt{2}$	$\sqrt{2}$
hcp	(10.8373,0,0)	(0,11.2624,0)	(0,0,10.6183)	$\sqrt{3}$	$\sqrt{8/3}$

Table 6.4: Orthorhombic distortions. Lattice vectors corresponding to distortions A, B, C, and D, along with lattice vectors used for *fcc*, *bcc* and *hcp* supercells. Volume per atom: 7.2 Å^3.

Mean Square Displacements

Total and partial mean square displacements (MSD) along the lattice vectors **a**, **b** and **c** (X, Y and Z directions) were computed from the positions of atoms as a function of time from results of molecular dynamic simulations. The the trajectory of atoms obtained from VASP were analyzed with the LPMD software package, a molecular dynamics code developed during the course of this thesis in collaboration with the Group of Nanomaterials at the Universidad de Chile (see appendix C), which was published [159] and uploaded to its own website, `http://www.lpmd.cl`, as a free open-source code. For calculating the partial MSD, a slight modification of the MSD plugin was implemented in the LPMD code: a decomposition in X, Y and Z components which, when added together, sum the total MSD. This allows us to determine what is the dominant direction in which the atoms are moving when a rearrangement of atoms takes place during a simulation. MSD of atoms in tetragonal and orthorhombic cells is presented in figure 18.

For tetragonal distortions (figure 18, left panel), MSD shows an overall motion of atoms along **c** (Z direction) for all points chosen along the Bain path. This motion

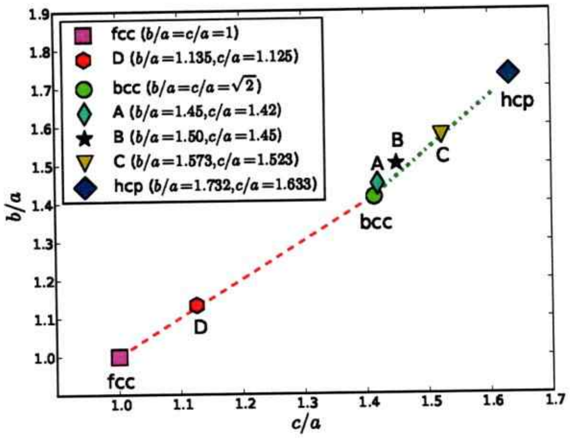

Fig. 17: The figure shows the various points chosen from energy contours in figure 16 for AIMD simulations. Points A, B and C show successive orthorhombic distortions from *bcc* towards *hcp* while point D denotes stretching towards *fcc*.

increases with increase in c/a ratio. We notice that there is almost no difference in the displacements along **a** and **b** (X and Y directions), indicating that atoms vibrate around their initial X and Y positions, but moved to another Z position. For orthorhombic strains (right panel), MSD in the Y direction increases considerably for distortion point B, compared with A, and decreases for point C, which is close to *hcp*. For distortion towards *fcc* (point D), the MSD in X direction is slightly larger than in Y and Z directions. However there is no noticeable difference in the MSD of atoms in any directions for *bcc*. Although point A is close to *bcc* in orthorhombic distortions, we notice large atomic motion in Y direction as compared to the motion in Z direction for $c/a = 1.05$ in tetragonal distortions, which is the closest point to *bcc* for those distortions, indicating stronger instability for orthorhombic distortions. These displacements show strong preference for the *fcc* and *hcp* phases, since for distortions close to these structures, the MSD is isotropic, meaning that atoms remain

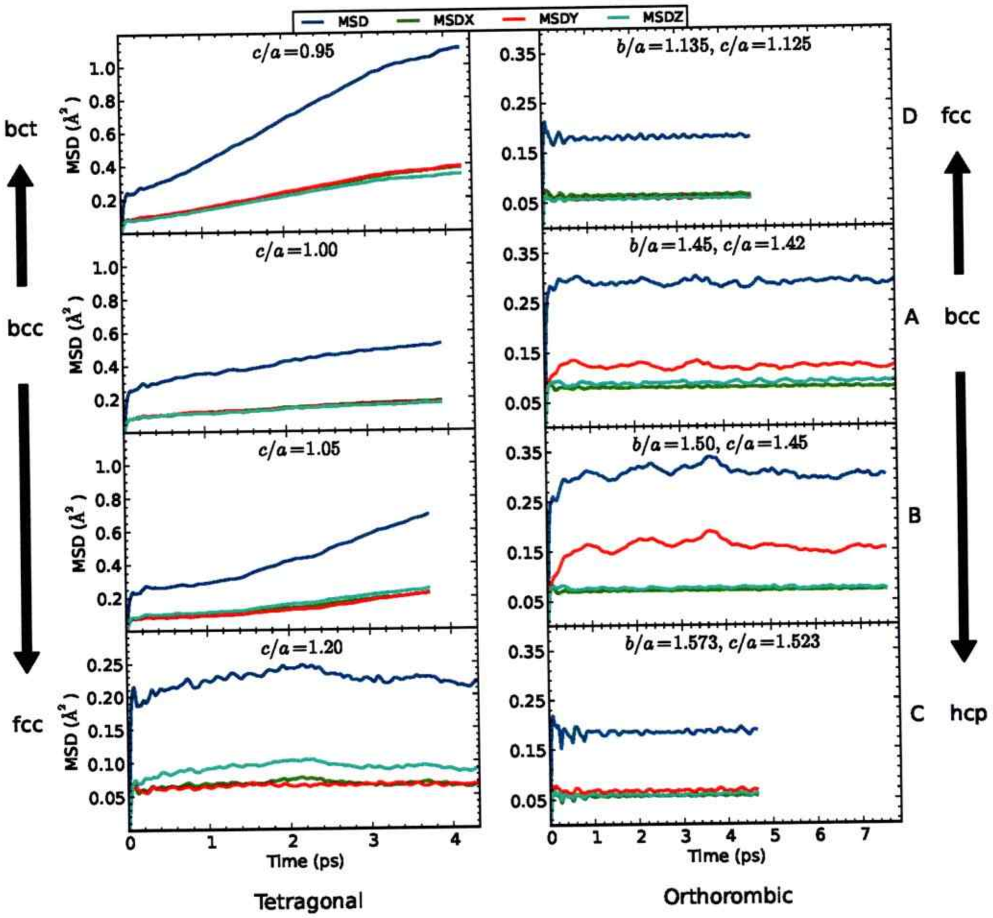

Fig. 18: Mean square displacements (MSD) of atoms along X, Y and Z directions and the resultant MSD for tetragonal (left panel) and orthorhombic (right panel) distortions.

around their initial positions in these structures, while *bcc* shows instabilities in the atoms positions, since the atoms were displaced in a prefered direction.

Stress Stability Analysis Under Tetragonal Distortions

The components of the stress tensor (S_{ij} with $i, j = x, y$ or z) were obtained from the ab initio molecular dynamics and are shown as a function of time in figure 19 for tetragonal and orthorhombic distortions (discussed in the following section). As we can see in the left panel (tetragonal distortions), the tensor S_{ij} becomes anisotropic for values of c/a deviating on either side of $c/a = 1$ (*bcc*), that is, towards either *bct* or *fcc*.

The values of S_{ij} were used to study the relationship between these anisotropies and the stability of the *bcc* phase against pure shear along the isochoric Bain path through stability creteria, as suggested by previous studies [160–164]. In tetragonal distortions at fixed volume and no shear (see appendix D), the strain tensor is defined by

$$\varepsilon = \begin{pmatrix} (1+\delta)^{-\frac{1}{2}} - 1 & 0 & 0 \\ 0 & (1+\delta)^{-\frac{1}{2}} - 1 & 0 \\ 0 & 0 & \delta \end{pmatrix} , \tag{6.1}$$

Since the unstrained tetragonal cell is *bcc*, δ is related to c/a (see equation (D.9)) by

$$\frac{c}{a} = (1+\delta)^{\frac{3}{2}} , \tag{6.2}$$

which means that $\delta = 0$ $(c/a = 1)$ corresponds to the *bcc* structure, while $\delta = \sqrt[3]{2} - 1 \approx 0.26$ $(c/a = \sqrt{2})$ defines the *fcc* structure. The Helmholtz free energy is related to the strain by

$$F(\delta, T) = F(0, T) + VS_L\delta + \frac{3}{2}VB_S\delta^2, \tag{6.3}$$

where the longitudinal stress anisotropy

$$S_L = S_{zz} - \frac{1}{2}(S_{xx} + S_{yy}) \tag{6.4}$$

and the shear elastic constant (shear modulus)

$$B_S = \frac{1}{2}(B_{11} - B_{12}) \tag{6.5}$$

are related by

$$S_L(\delta) = S_L(0) + B_S\delta. \tag{6.6}$$

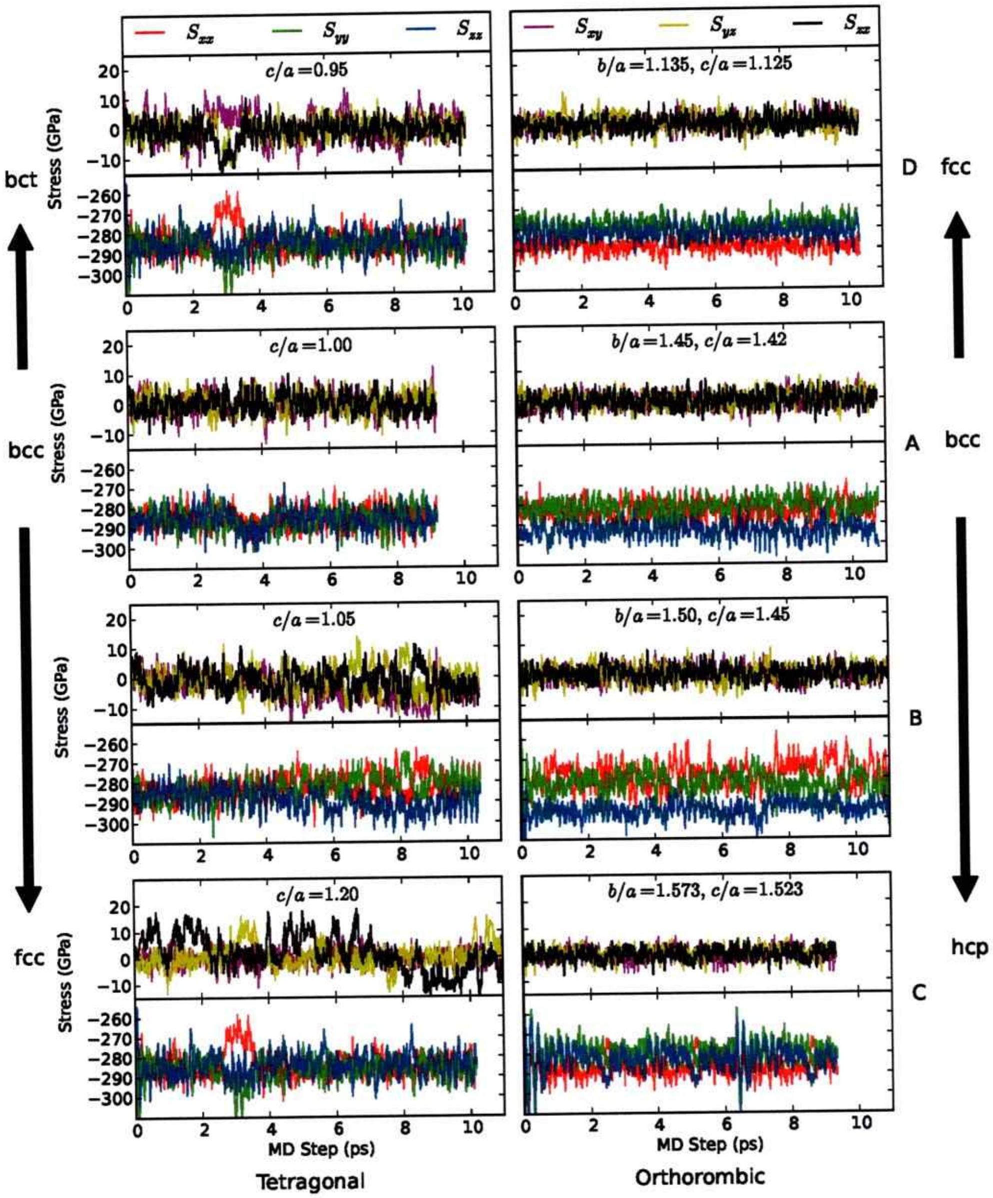

Fig. 19: Variation of various components of stress tensor with time for tetragonal (left panels) and orthorhombic (right panels) distortions.

Here, the shear modulus is written in terms of the B_{ij} coefficients, which are the elastic stiffness constants defined in Wallace's work [165], rather than in terms of the usual C_{ij} stiffness constants, known as moduli of elasticity. The coefficients B_{ij} are related to the C_{ij} through relations that include the pressure applied to the system ($B_{ij} = C_{ij}$ if all $S_{ij} = 0$, that is, zero pressure), and they are the appropriate elastic constants to analyze stability under pressure since, under external loading, the elastic constants C_{ij} are dependent on the applied stress [160, 163, 164].

Three generally accepted elastic stability criteria for a cubic crystal are

$$B_{11} + 2B_{12} > 0, \tag{6.7}$$

$$B_{44} > 0, \tag{6.8}$$

$$B_S = \frac{1}{2}(B_{11} - B_{12}) > 0, \tag{6.9}$$

which are connected to the bulk, shear and tetragonal shear moduli respectively and are referred to as spinodal, shear and Born criteria, respectively [165]. We also write these stability conditions in terms of the B_{ij} coefficients instead of the C_{ij}, since the Born criterion, as well as the others, were formulated in the zero stress state, which makes problematic to predict elastic stability of a crystal under external loading, whereof the need for stress-dependent elastic constants arises. In the case of tetragonal distortions, mechanical stability requires the Helmholtz free energy in (6.3) to be at a minimum with respect to δ, which yields the following two conditions of mechanical stability:

$$S_L = 0, \tag{6.10}$$

$$B_S > 0. \tag{6.11}$$

The first of these, (6.10), is satisfied if the state of stress in the *bcc* phase is isotropic: $S_{ij} = -P\delta_{ij}$ where P is the pressure and δ_{ij} is the Kroenecker delta. The second one, (6.11), is the same as (6.9). Thus, we will focus on these two relationships to study stability under tetragonal distortions, since $S_L = 0$ and $B_S > 0$ provide the necessary and sufficient conditions for mechanical stability.

Extensive convergence tests were performed to obtain S_L, and the error introduced by taking few k-points calculating the longitudinal stress anisotropy was corrected by taking

$$S_L(\delta) = S_L(\delta, \Gamma) + \Delta S_L(\delta), \tag{6.12}$$

where the correction $\Delta S_L(\delta)$ is given by the difference between the value of $S_L(\delta)$ in the converged (infinite k-point) limit and its value using only the Γ point, that is, $\Delta S(\delta) = S_L(\delta, n_k \to \infty) - S_L(\delta, \Gamma)$. Through a series of calculations using the tetragonal 128-atom supercell, it was found that a $2 \times 2 \times 2$ k-point mesh yields fully converged values of the stress tensor. The correction varies linearly as $\Delta S_L(\delta) = 54(c/a - 1)$ GPa over the range $c/a = 0.95$–1.2.

The calculation of S_L and B_S by means of introducing the averages of the S_{ij} components over time into the equations (6.4) and (6.6), leads to the values shown in table 6.5, resulting in longitudinal instabilities according to the stability conditions (6.10) and (6.11). By analogy with S_L, we also compute shear-stress anisotropy

$$S_S = S_{zx} - \frac{1}{2}(S_{xy} + S_{yz}), \tag{6.13}$$

that we believe to be responsible for the *bcc*-*hcp* transition away from the Bain path. A plot of the longitudinal-stress anisotropy S_L is shown together with the shear-stress anisotropy S_S in figure 20.

The mentioned anisotropic behavior of S_{ij} for values of c/a deviating to *bct* and *fcc* is therefore reflected on the calculated values for S_L, produced by the tetragonal distortion; and with no distortion ($c/a = 1$) the stresses are isotropic, implying they are hydrostatic in the simulation cell. Development of anisotropic stresses results in instabilities in the longitudinal stress, S_L, which is related to shear elastic constant

Axial Ratio (c/a)	$\delta = (c/a)^{2/3} - 1$	S_L (GPa)	S_S (GPa)	B_S (GPa)
0.95	-0.0316	1.96	0.62	-62.1
1.05	0.0308	-1.64	-1.30	-53.3
1.1	0.0656	-0.98	0.97	-14.9
1.15	0.0977	-0.96	1.27	-9.8
1.2	0.1292	-0.82	1.57	-6.4

Table 6.5: Variation of S_L, S_S and B_S with axial ratio c/a. Shear elastic constant is seen negative confirming instability of *bcc* iron under tetragonal distortions.

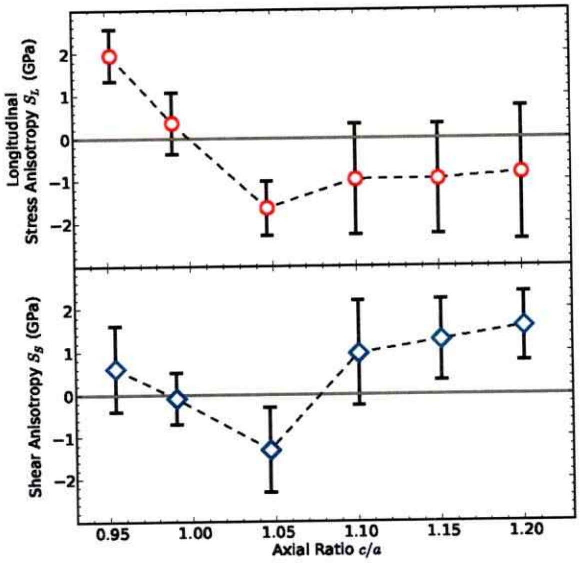

Fig. 20: Comparison of longitudinal stress anisotropy with shear stress anisotropy as a function of c/a ratio. Shear stress instabilities are smaller than longitudinal stress instabilities but mostly positive within the associated uncertainties. The stability criteria (6.10) is violated for all values of c/a.

B_S through (6.6).

In figure 21 we provide the results of total energy calculations and variation of the longitudinal-stress anisotropy S_L along the Bain path at $T = 0$ and $T = 5500$ K.

We point out that shear instabilities are the outcome of MD simulations which are absent in electronic structure based total energy calculations along the Bain Path. In strained configurations, the stress tensor is anisotropic, as demonstrated by the values of the longitudinal stress anisotropy (figures 20 and 21), which decreases monotonically with increasing δ. There is thus no restoring force acting against tetragonal strain: S_{zz} becomes more negative as the c-axis is stretched, corresponding to a driving force acting to further stretch the c-axis. At $\delta = 0$ ($c/a = 1$) the stress tensor is isotropic, in agreement with previous ab initio molecular dynamics simulations [130, 131].

Detailed analysis reveals that *bcc* iron violates the Born stability criterion for shear modulus (6.11), which has not always been examined in previous ab initio molecular dynamics studies. We find that $B_S = -53.3$ GPa for $c/a = 1.05$, clearly documenting instability. This disagrees with a previous ab initio results giving $(B_{11} - B_{12}) > 0$, but the calculations were for much smaller systems (54 atoms) and we infer that they were under-converged [130].

In addition, *bcc* iron has erroneously been claimed stable due to the calculations finding the stress tensor to be isotropic for $c/a = 1$, $S_L(\delta = 0) = 0$: this condition guarantees only that *bcc* iron occupies a local extremum on the energy surface [130, 135, 139]. Later work on the stability of *bcc* iron under tetragonal strain found significantly different results when using a 128 atom cell and a single k-point, including mechanical instability of *bcc* Fe at 6000 K with 64 atom cell [132]. This is in accord with the present, more extensive simulations, where we also find that shear anisotropy develops upon application of tetragonal strain, a feature that is not apparent in low-temperature calculations based on the primitive unit cell. In figure 21, the stress anisotropy obtained from electronic structure calculations (lower

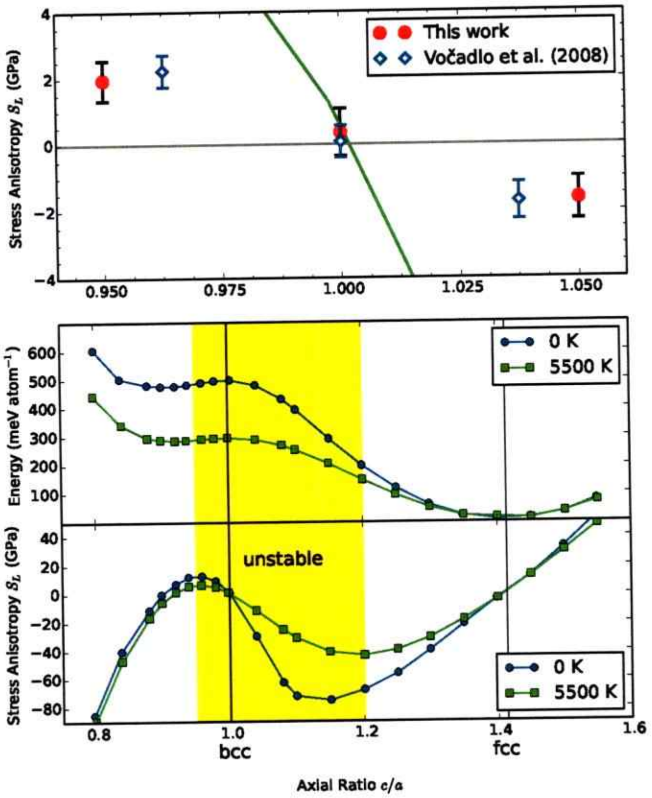

Fig. 21: (Upper)Variation of longitudinal elastic anisotropy with tetragonal strain from ab initio molecular dynamics simulations (red symbols) as compared with the result for the static lattice with $T = 5500$ K (green line). The open diamonds represent the results of Vočadlo *et al.* [132] for a 128 atom cell and a single k-point. (Lower) Computed free energy (top, plotted relative to *fcc* energy) and stress anisotropy S_L (bottom) of iron along the isochoric Bain path at a volume of 7.2 Å^3/atom for the static lattice, and for electrons at $T = 0$ (blue circles) and $T = 5500$ K (green squares). The values of the c/a ratio corresponding to the *bcc* (1.0) and *fcc* ($\sqrt{2}$) structures are indicated by vertical black lines. The yellow shading shows the range of values of the c/a ratio that violate the Born stability criterion (6.11).

panel) can be compared with results from AIMD (upper panel). The shear-stress anisotropy is smaller than the longitudinal anisotropy (mostly positive) for c/a values up to $c/a = 1.2$ (figure 20) demonstrating a further mechanical instability of *bcc* iron that has not previously been recognized.

Other studies claiming mechanical stability of *bcc* iron are not based on ab initio molecular dynamics, but instead on an embedded atom model (EAM) potential that is fit to a limited number of ab initio results [130]. Results based on EAM [131] cannot be considered reliable to study stability, among other reasons, because they predict *bcc* to have the lowest Gibbs free energy at the conditions considered here, in disagreement with ab initio calculations showing that *hcp* is in fact more stable [130]. Therefore, past studies claiming stability of *bcc* Fe suffered from (i) misinterpretation of the requirements for mechanical stability (stability inferred only from isotropy of stress tensor for *bcc*) and/or (ii) the use of classical many-body potentials, the accuracy of which are untested for documenting mechanical stability of *bcc* iron.

Stress Stability Analysis Under Orthorhombic Distortions

The components of the stress tensor are shown as a function of time in figure 19 for the four points chosen for orthorhombic distortions (A, B, C and D, defined in table 6.4 and shown in figure 17), along with the evolution of the stress components in tetragonal distortions. We observe that the stress anisotropy increases for orthorhombic distortions away from *bcc* ($b/a = c/a = \sqrt{2}$) towards A and B. The diagonal elements of the stress tensor show greater spread in values near *bcc* (point A and especially point B) than for closed-packed structures points (C and D, corresponding nearly to *hcp* and *fcc*). The upper panels in figure 19 show the off-diagonal elements. We also notice that the difference in off-diagonal elements of the stress tensor under tetragonal distortion show larger anisotropy (almost by a factor of 10) as compared with the values for orthorhombic distortion. To analyze the mechanical stability in orthorhombic distortions, we compute the quantities

$$S_c = S_{zz} - S_{xx} \tag{6.14}$$

$$S_b = S_{yy} - S_{xx} \tag{6.15}$$

from the diagonal elements of stress tensor, as suggested in previous works [160–163], and the difference between relative strains

$$e_c = \varepsilon_c - \varepsilon_a \tag{6.16}$$

$$e_b = \varepsilon_b - \varepsilon_a, \tag{6.17}$$

that result from stretching *bcc* towards *hcp* or *fcc* (ε_α being the change in the lattice parameter relative to starting *bcc* lattice along $\alpha = X, Y$ or Z). We determine the stability by the sign of the stress-strain products $S_c \cdot e_c$, $S_b \cdot e_b$, with positive values indicating stability and the stresses tend to restore the structure; if the products are negative, then the applied strain is further enhanced and the structure is unstable, that is,

$$S_c e_c > 0, \tag{6.18}$$

$$S_b e_b > 0. \tag{6.19}$$

For distortions of *bcc* towards *hcp*, A ($b/a = 1.45$, $c/a = 1.42$), B ($b/a = 1.5$, $c/a = 1.45$), we find positive values for both e_c and e_b and negative values for both S_c and S_b (see tables 6.6 and 6.7); the structures are therefore mechanically unstable. For points C (close to *hcp*) and D (close to *fcc*) find that $S_c e_c > 0$; $S_b e_b > 0$, indicating that these structures are stable. We found that sampling the Brillouin zone on at least a $2 \times 2 \times 2$ k-point mesh was essential in arriving at these conclusions.

Point / S_{ij}	A	B	C	D
S_{xx} (GPa)	-277.726	-283.095	-287.888	-288.492
S_{yy} (GPa)	-282.017	-284.193	-278.958	-278.156
S_{zz} (GPa)	-295.473	-293.402	-282.686	-281.714
S_{xy} (GPa)	0.0761	-0.238	-0.128	0.131
S_{yz} (GPa)	0.325	0.0574	0.131	0.146
S_{zx} (GPa)	0.139	-0.171	-0.164	-0.003

Table 6.6: Average stress tensor for points A, B, C and D with $2 \times 2 \times 2$ k-points mesh.

Point	ε_a	ε_b	ε_c	e_c	e_b	S_c	S_b	$S_c \times e_c$	$S_b \times e_b$
A	-0.0276	0.0314	-0.003	0.0246	0.0590	-17.747	-4.291	-0.437	-0.253
B	-0.0097	0.0154	-0.0056	0.0041	0.0251	-10.307	-1.038	-0.0421	-0.0261
C	-0.0588	0.0473	0.0134	0.0721	0.1061	5.202	8.930	0.3753	0.9471
D	0.1613	-0.0680	-0.0762	0.2374	0.2293	6.778	10.336	1.6093	2.3699

Table 6.7: Strains along cell vectors $\mathbf{a}, \mathbf{b}$, and $\mathbf{c}$ (ε_a,ε_b, and ε_c, respectively), stress difference $S_c = S_{zz} - S_{xx}$ and $S_b = S_{yy} - S_{xx}$, strain difference $e_c = \varepsilon_c - \varepsilon_a$ and $e_b = \varepsilon_b - \varepsilon_a$, together with stability conditions (6.18) and (6.19).

6.3.3 Structure analysis for tetragonal and orthorhombic distortions

In order to determine the structure resulting from these instabilities, we used the Common Neighbor Analysis (CNA) technique [166], which is based on nearest neighbor atoms coordination to distinguish among different structures produced in the molecular dynamics. The CNA method comes implemented in the LPMD code [159], which was also used to calculate the MSD in the previous section. A detailed explanation of the method can be found in the appendix C.

To analyze the coordination of atoms through CNA, we chose the structure present at the final step of the MD simulations, which represents a thermodynamically equilibrated structure. In figure 22 we show the raw atomic pattern from final

MD step for tetragonal distortion $c/a = 0.95$ and for orthorhombic distortion point A, together with the pair (radial) distribution function (RDF), which we use to fix the cutoff radius r_c for CNA ($r < r_c$ will mean two atoms are bonded), and coordination number as a function of the distance. However, the analysis performed over

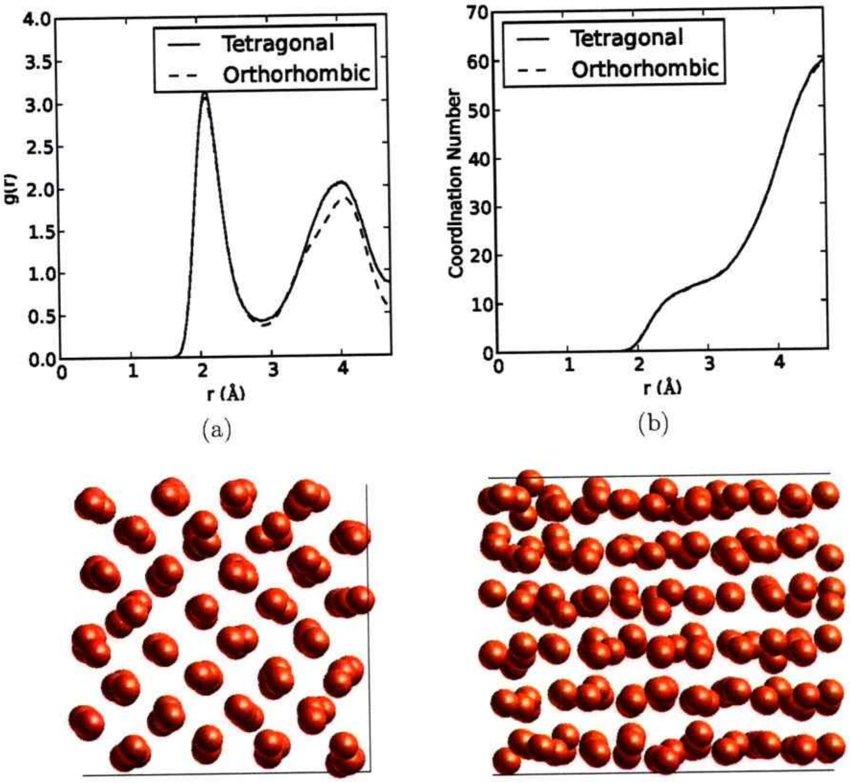

(a)

(b)

(c)

(d)

Fig. 22: (a) and (b) show the time-averaged radial distribution function $g(r)$ and coordination number CN for tetragonal ($c/a = 0.95$) and orthorhombic distortions (point A, $b/a = 1.45$, $c/a = 1.42$). (c) and (d) display atoms in the XY plane of the simulation cells in the final step of MD simulation for tetragonal and orthorhombic distortions, respectively. Common neighbor analysis (CNA) carried out for (c) and (d) and also all other simulations for last snapshot of the simulation failed to reveal any crystalline structure.

the final time step MD simulations failed to provide any structure, so we generated time-averaged structures for each case from the average positions of individual atoms over the entire MD simulation. We display such average structures for $c/a = 0.95$ and $c/a = 1.05$ in figure 23, and for orthorhombic distortion points A and B in figure 24. In both cases, we compare the radial distribution function and coor-

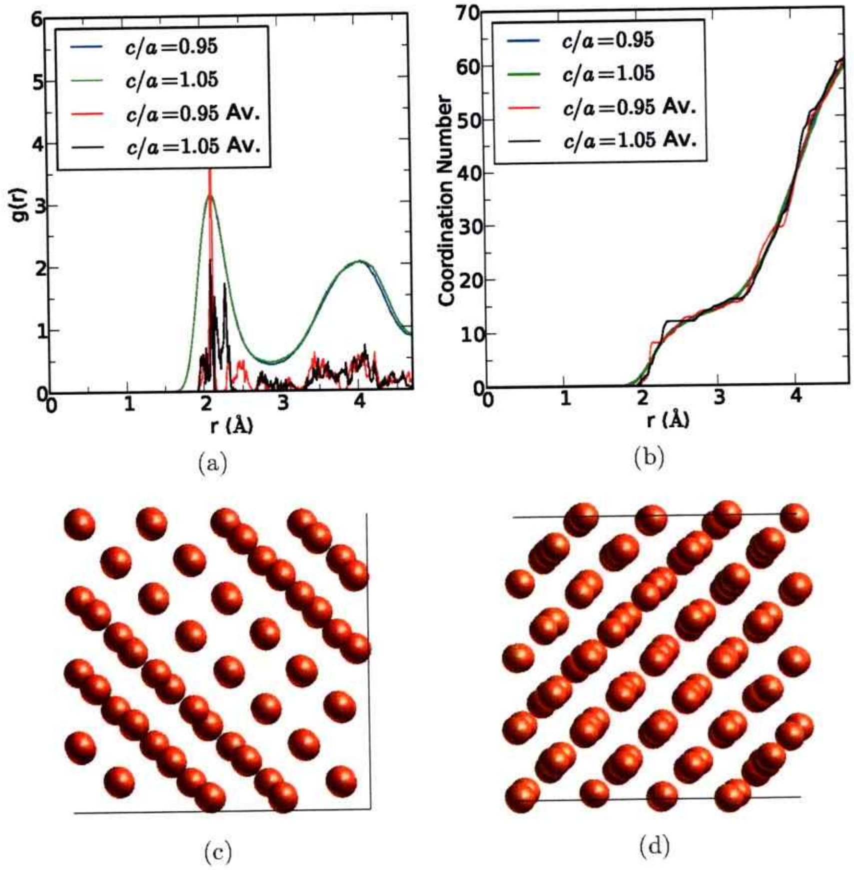

(a)

(b)

(c)

(d)

Fig. 23: Comparison between average structures generated for tetragonal distortions $c/a = 0.95$ and $c/a = 1.05$. (a) and (b) compare the radial distribution function (RDF) and coordination number (CN) of both samples with the instantaneous RDF and CN of their average structures, shown from the XY plane in (c) and (d), respectively. CNA showed them to be mostly *bcc* and *hcp* (see Table 6.8).

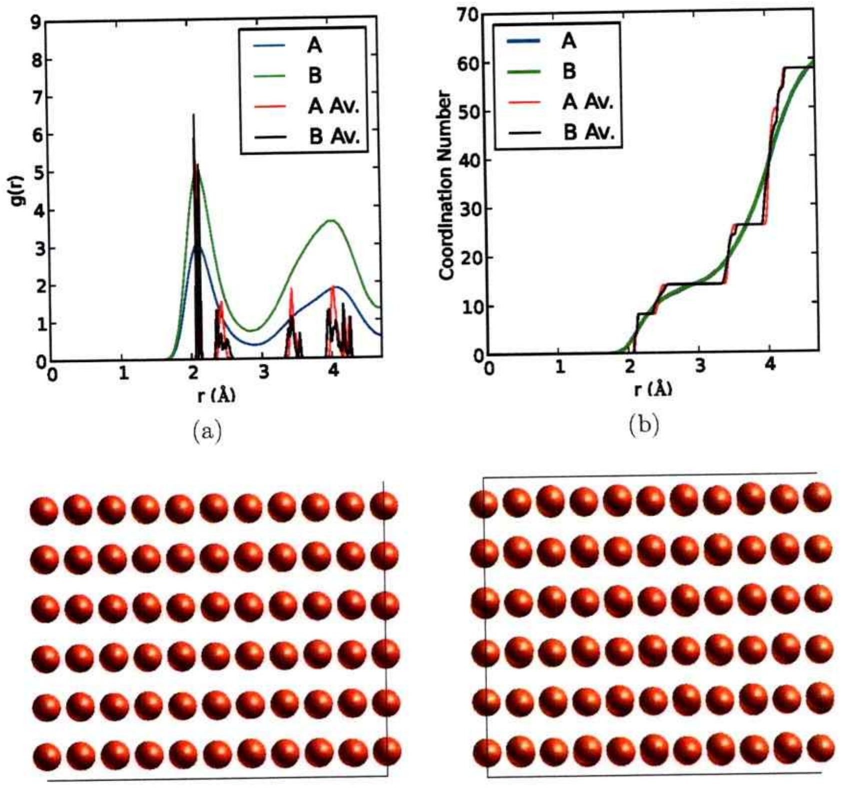

(a) (b)

(c) (d)

Fig. 24: Comparison between average structures generated for orthorhombic distortions A ($b/a = 1.45$,$c/a = 1.42$) and B ($b/a = 1.50$, $c/a = 1.45$). (a) and (b) compare the radial distribution function (RDF) and coordination number (CN) of both samples with the instantaneous RDF and CN of their average structures, shown from the XY plane in (c) and (d), respectively. CNA show them to be mostly *bcc* (see table 6.8).

dination number for these structures. We noticed that for tetragonal distortions of $c/a = 0.95$ and 1.05 (figure 23) the time-averaged structures have a majority of neighboring pairs consistent with *bcc* and *hcp* structures respectively (see table 6.8). Orthorhombic distortions (figure 24) yield time-averaged structures corresponding to *bcc* for point A and an unknown structure for point B. For distortions C and D

the time-averaged structures were *hcp* and *fcc* respectively, consistent with the fact that those are precisely their colsest structures.

Distortion	Types of pairs	Structure	Ideal types of pairs
Tetragonal: $c/a = 0.95$	444 (30.36%) 555 (25%) 666 (44.64%)	*bcc*-like	444 (42.9%) 666 (57.1%)
Tetragonal: $c/a = 1.05$	300 (3.125%) 421 (53.125%) 422 (40.625%) 544 (3.125%)	*hcp*-like	421 (50%) 422 (50%)
Orthorhombic: A	421 (0.80%) 433 (2.88%) 444 (39.36%) 544 (5.12%) 666 (51.84%)	*bcc*-like	444 (42.9%) 666 (57.1%)
Orthorhombic: B	421 (37.40%) 422 (18.04%) 433 (8.66%) 444 (9.20%) 544 (17.33%) 666 (9.37%)	Unknown	

Table 6.8: Resulting structures from positions averaged over entire MD simulation time. Performing quenched molecular dynamics over these structures, led to quenched average structures whose CNA showed 421 and 422 types of pairs only, except for the case of $c/a = 1.05$ where 10.5% of pairs were not 421 nor 422. This shows that all structures are *hcp*.

However, these results were still not satisfactory, since the atoms in average structures had large forces on them. Therefore, we allowed them to relax using a quenched molecular dynamics (QMD) algorithm, which takes the atoms from the final time-step of our AIMD simulation to their closest equilibrium positions. The quenched structures reveal displacements in mean-atomic positions away from *bcc* sites, which is shown for one tetragonal case and one orthorhombic case in figure 25.

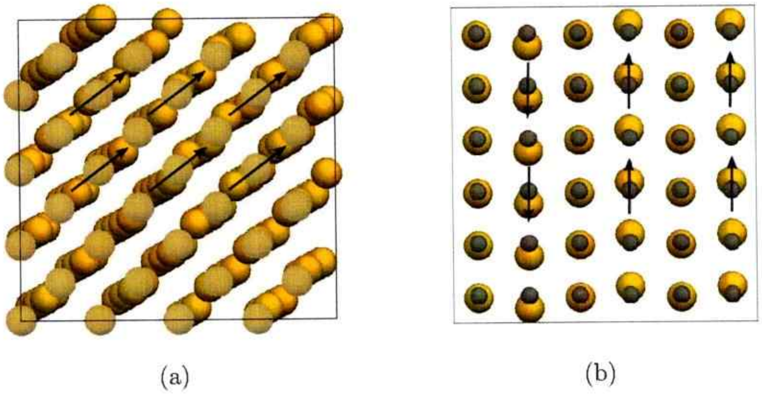
(a) (b)

Fig. 25: Representation of the structure of Fe in the YZ plane resulting from quenching the final time step of the MD run for tetragonal distortion (a) $c/a = 1.05$ and (b) for orthorhombic distorted point A. Arrows show the pattern of atomic motions from ideal *bcc* sites (transparent dots for tetragonal distortion for $c/a = 1.05$ and black dots for orthorhombic distortion point B to relaxed atomic positions (yellow)).

We show in figures 26 and 27 a comparisson between the radial distribution function and coordination number of the samples, and in figure 28, just for clearer comparisson, is a diagram of the same structures put together in their way to their quenched structures. It can be noted in these figures that the smeared pattern of the radial distribution function of the average structures is replaced by clear peaks in the quenched structure, pointing toward well defined structures. Quenching at $c/a = 0.95$ and 1.05 for tetragonal distortion and for orthorhombic distortions A and B led to the final *hcp* structure:

- For $c/a = 0.95$, 75% of the pairs were 421 and 25% were 422 which, in fact, differs from perfect *hcp* only in percentage types (see table C.1), but keeps the same atomic neighbors coordination.
- For $c/a = 1.05$, CNA showed 421 and 422 types of 50% each of neighboring

pairs, consistent with *hcp* structure.

- For tetragonal distortions up to $c/a = 1.2$, all the time-averaged structures were *bcc* (except $c/a = 1.05$ which was *hcp*), and the analysis of quenched atoms from the final MD step yielded the *hcp* structure (table 6.8).
- CNA revealed that the quenched average structure of A and B having only 421 and 422 types of pairs of equal amount, as in the case with *hcp* structure.
- Quenching the average structures for orthorhombic points C and D did not change their structures, and they remained in *hcp* and *fcc* respectively.
- We also carried out relaxation of internal degrees of freedom on atoms from final MD step using conjugate gradient method, which lead to a structure that showed same types of neighboring pairs as we obtained from quenching for orthorhombic distortions.

Our results indicate that the existence of shear stress instabilities (see equation 6.13) to be the cause for *hcp* being more stable, which in fact is away from *bcc*-*fcc* transition path of orthorhombic distortions.

6.3.4 Possibility of *bcc* phase at high temperatures and densities

We investigated stability of *bcc* iron at temperatures higher than 5500 K and inner-core densities. We carried out molecular dynamic simulations at Γ-point along with $2 \times 2 \times 2$ k-point mesh for tetragonal ($c/a = 1.05$) and orthorhombic (point A) at 7000 K. The stress variation for these as a function of time is shown in figure 29. Variation of diagonal and off-diagonal stresses is seen to be anisotropic and very much similar to their behavior at 5500 K, shown in the previous section.

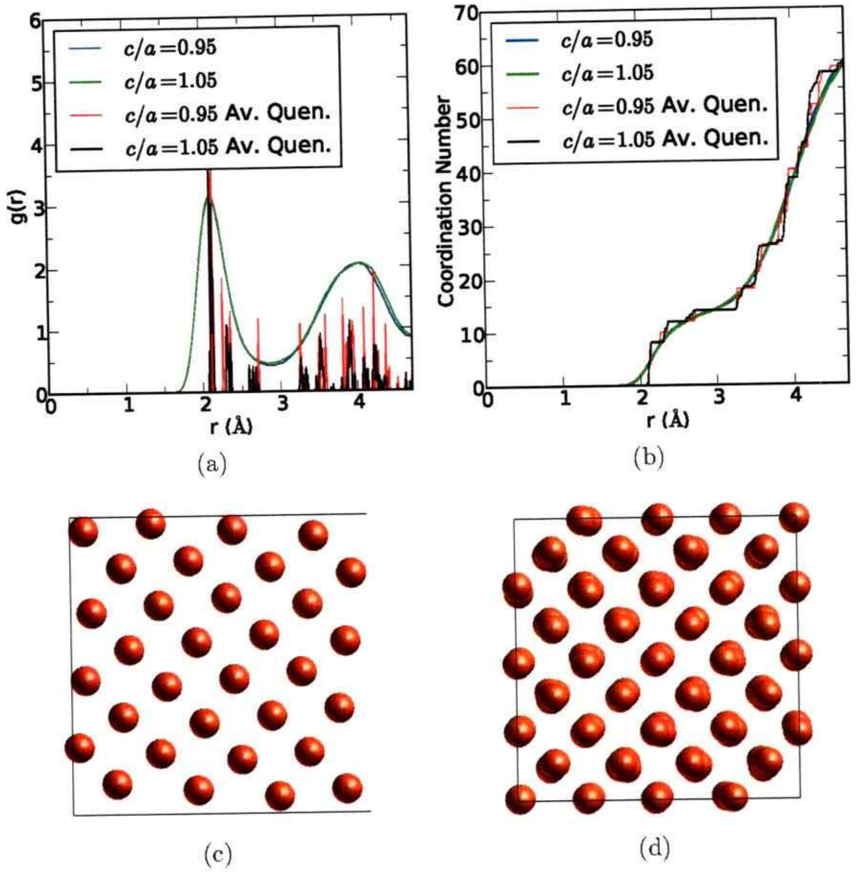

(a)

(b)

(c)

(d)

Fig. 26: Comparison between average structures generated for tetragonal distortions $c/a = 0.95$ and $c/a = 1.05$ after the quenching process (QMD) performed over the structures shown in figure 23. (a) and (b) compare the RDF and CN of both samples with the instantaneous RDF and CN of their quenched average structures, shown from the XY plane in (c) and (d). The observed peaks and steps respectively in RDF and CN are consistent with *hcp* arrangement, according to CNA.

We provide the average stress tensors in table 6.9 for $c/a = 1.05$ and point A at the highest temperature analyzed, 7000 K. Stress stability analysis (section 6.3.2) carried out for this tetragonal distortion at this higher new temperature reveals a negative shear modulus value (-82 GPa). Applying the stress stability analysis for orthorhombic distortion to the point A (equations (6.18) and (6.19)) we find both

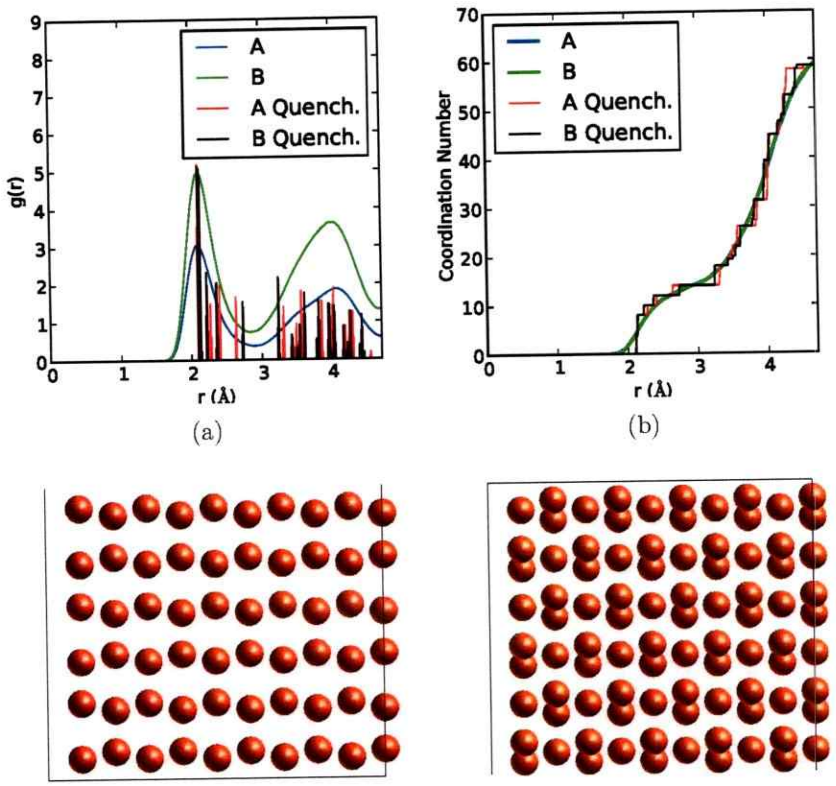

(a) (b)

(c) (d)

Fig. 27: Comparison between average structures generated for orthorhombic distortions A ($b/a = 1.45$, $c/a = 1.42$) and B ($b/a = 1.50$, $c/a = 1.45$) after the quenching process (QMD) performed over the structures shown in figure 24. (a) and (b) compare the RDF and CN of both samples with the instantaneous RDF and CN of their quenched average structures, shown from the XY plane in (c) and (d). The observed peaks and steps respectively in RDF and CN indicate ordered structures. CNA showed (see table 6.8) that (c) was *hcp* and (d) *hcp*-like (presence of small amounts of other pairs).

products $S_c \cdot e_c$ and $S_b \cdot e_b$ to be negative. Thus *bcc* phase of Fe is unstable both under tetragonal and orthorhombic distortions at the temperature of 7000 K. The time-averaged structures for both $c/a = 1.05$ and for point A were found to be in *hcp* with atoms having large forces. Quenching the atoms and treating them with

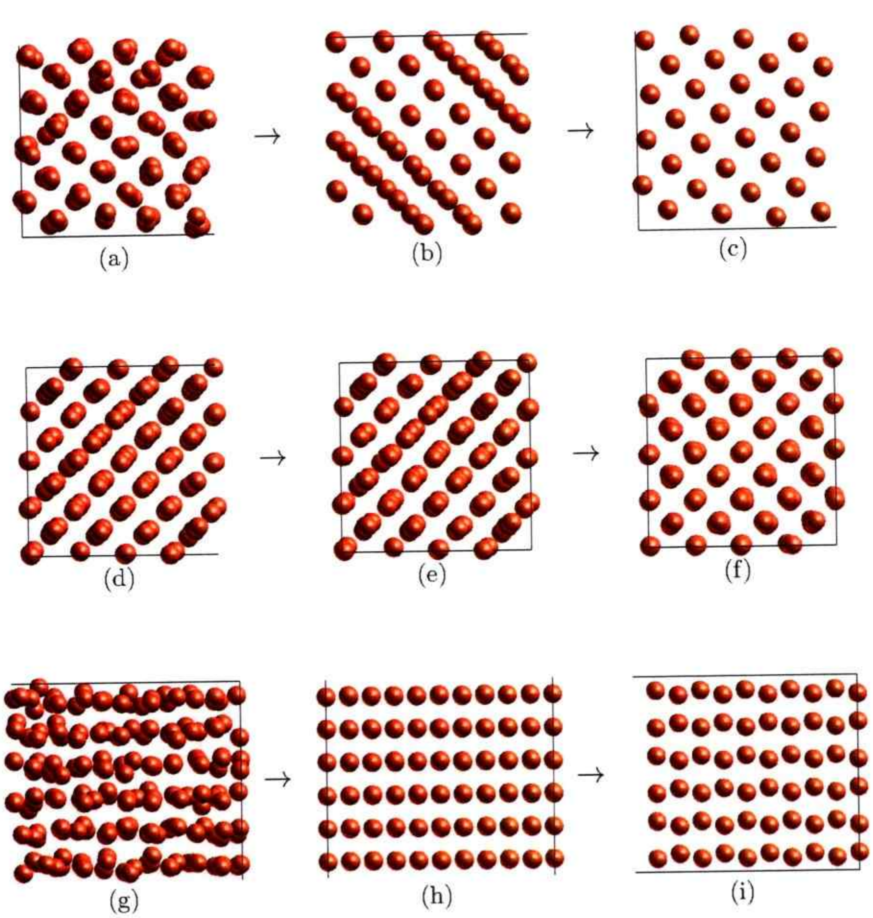

Fig. 28: Path to equilibrium positions, from last step of the MD (left) to the average structure (middle) to the quenched average structure. The first two rows corespond to the tetragonal points $c/a = 0.95$ and $c/a = 1.05$, while the third column is the orthorhombic point A.

CNA showed 421 (50%), 422 (50%) types of pairs. The structure thus is *hcp*, hence our studies do not support that anharmonic or entropy stabilization of *bcc* phase in iron has occurred at 360 GPa pressure even at temperature of 7000 K.

We also carried out AIMD simulations for tetragonal distortions along the isochoric Bain paths for the density and temperature conditions reported in the paper

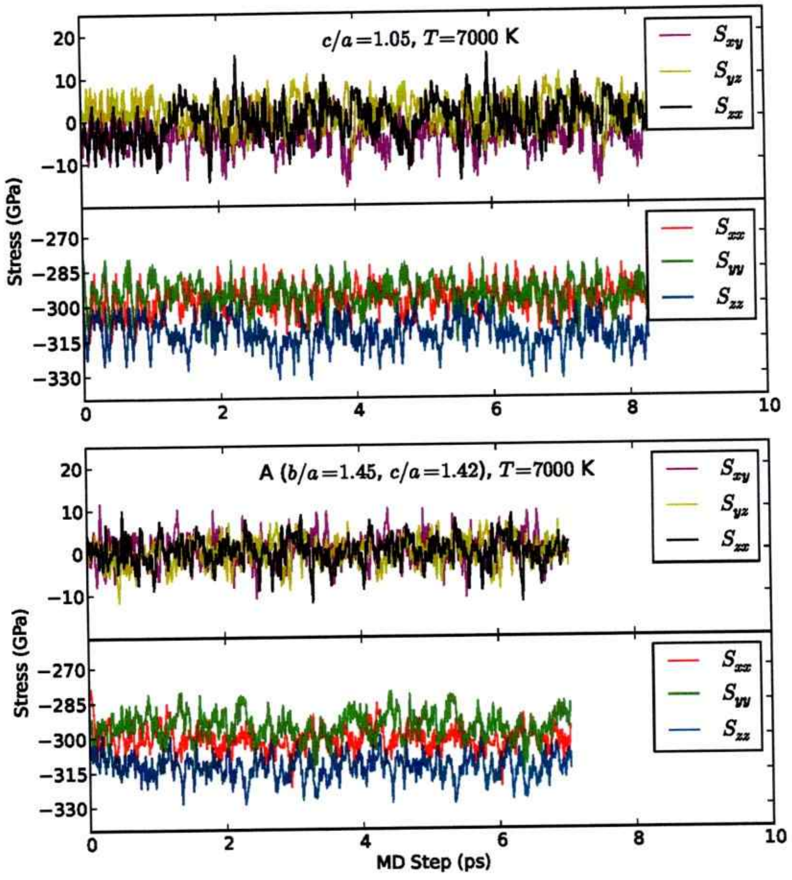

Fig. 29: Variation of various components of stress tensor with time for tetragonal distortion $c/a = 1.05$ (top) and orthorhombic distortion point A (bottom) at temperature of 7000 K.

by Bouchet et al. [139], comparing results for a $2 \times 2 \times 2$ k-point mesh with those for only the Γ-point. Our PAW potentials include $3s$, $3p$, $3d$ and $4s$ states as valence electrons with cutoff radii and cutoff energies the same as the values used in Bouchet study. We find the stresses becoming anisotropic for tetragonal distortions on either side of $c/a = 1$ for densities of 16, 18 and 20 g/cm^3 at temperatures above those Bouchet et al. inferred the *bcc* to be stable (see figure 30 for the evolution of stresses

Point S_{ij}	$c/a = 1.05$	A
S_{xx} (GPa)	-298.012	-288.4922
S_{yy} (GPa)	-295.402	-278.156
S_{zz} (GPa)	-312.222	-281.7144
S_{xy} (GPa)	3.756	0.1311
S_{yz} (GPa)	1.448	0.146
S_{zx} (GPa)	0.070	-0.003

Table 6.9: Average stress tensor for points A and $c/a = 1.05$ (Γ point with $(2 \times 2 \times 2)$ k-points mesh.

ρ (g/cm^3), T (K)	c/a	S_{xx} (GPa)	S_{yy} (GPa)	S_{zz} (GPa)	S_L (GPa)
18, 6000	0.95	952.0($\pm$2.5)	957.0($\pm$1.0)	915.0($\pm$4.1)	40.0($\pm$4.3)
	1.0	939.0($\pm$3.0)	944.0($\pm$4.0)	938.0($\pm$3.0)	
	1.05	931.0($\pm$1.2)	930.0($\pm$1.5)	957.0($\pm$1.8)	-26.0($\pm$2)
20, 7000	0.95	1358.0($\pm$3.2)	1358.0($\pm$3.4)	1313.0($\pm$2.9)	45.0($\pm$3.7)
	1.0	1345.0($\pm$0.2)	1343.0$\pm$(1.6)	1346.0($\pm$0.9)	
	1.03	1330.0($\pm$2.8)	1329.0($\pm$3)	1365.0($\pm$3.0)	-35.0($\pm$3.6)

Table 6.10: Diagonal elements of Stress tensor averaged over the simulation period and longitudinal stress instability calculated in present studies for density temperature values corresponding to Reference [139].

as a function of tetragonal distortion at densities of 18 g/cm^3 and 20 g/cm^3 at temperatures of 6000 K and 7000 K, respectively). The stresses were averaged over the simulation time, the time-averaged diagonal components of stress being provided in table 6.10.

The longitudinal stress anisotropy S_L is close to zero, within the uncertainties in stress (table 6.10). However $S_L > 0$ for $c/a < 1$, and $S_L < 0$ for $c/a > 1$, which is exactly opposite to the requirement for stability. The shear modulus is therefore negative, violating the second stability condition Therefore, our results do not support Bouchet et al.'s conclusion that the *bcc* phase is stable, as the Born stability criterion is robustly violated for pressures up to 1.5 TPa at 7000 K.

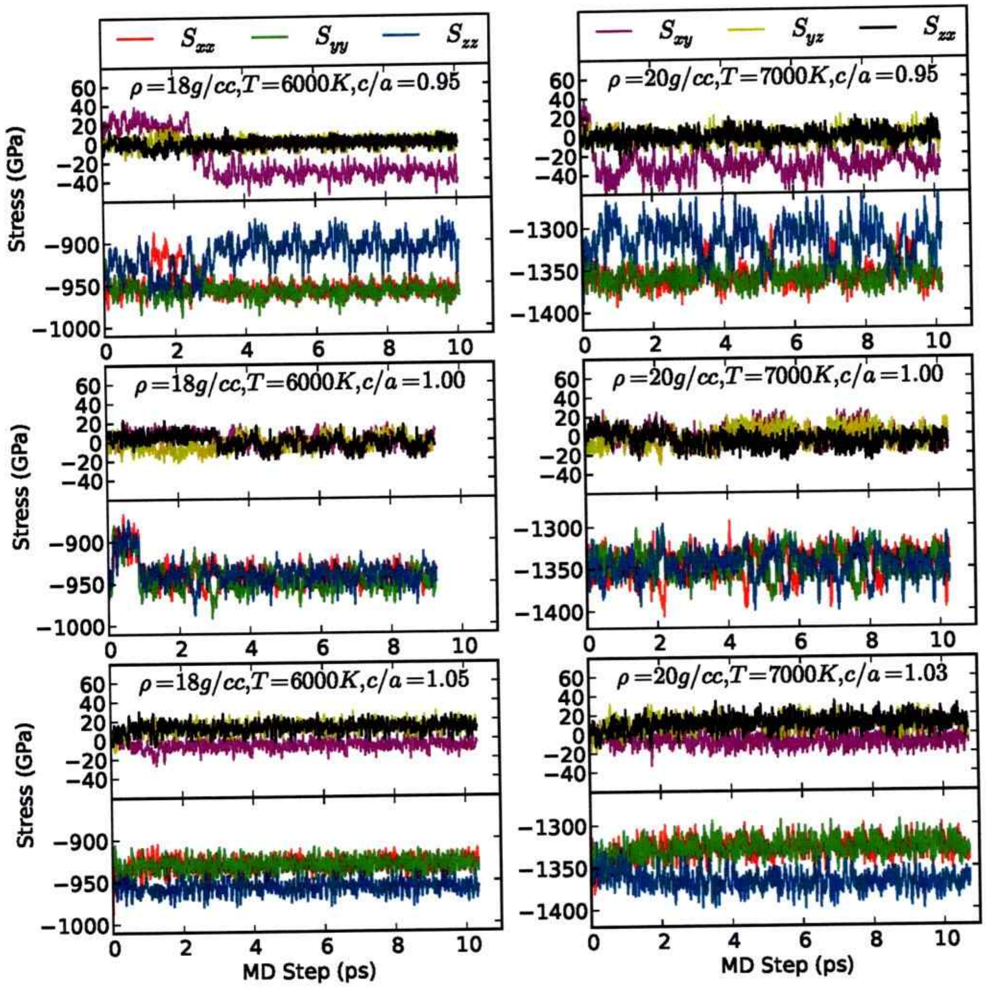

Fig. 30: Variation of stress tensor components with time for tetragonal distortions for density-temperature conditions corresponding to mechanical stability of *bcc* iron in reference [139]. The variation shows that the stresses converge to a mean value that differs from initial values do to changes in the structure during the simulation, which redistribute the stresses and produces the anisotropies. This also highlights the importance of long simulation times to get converged results.

6.4 Conclusions

We find that the mechanical instability of *bcc* iron originates in the static lattice contribution to the Helmholtz free energy (figure 21). For example, a series of static calculations on the Bain path combined with our AIMD results allow us to determine separately the three contributions to the Helmholtz free energy [118],

$$\begin{aligned} F(V,\delta,T,T_{el}) &= F_{st}(V,\delta,T=T_{el}=0) \\ &+ \Delta F_{el}(V,\delta,T=0,T_{el}) \\ &+ \Delta F_{ph}(V,\delta,T,T_{el}), \end{aligned} \tag{6.20}$$

from the static lattice and $T_{el} = 0$, from thermal excitation of electronic states ΔF_{el} at finite T_{el}; and from fully anharmonic lattice vibrations ΔF_{ph}. The variation of longitudinal stress S_L with free energy F for the static lattice shows the same mechanical instability seen in the AIMD calculations. At $T = 0$, S_L decreases with increasing δ, which requires $B_S < 0$, and also accounts for the local maximum in the total energy for *bcc* ($\delta = 0$) via

$$\frac{\partial^2 F}{\partial \delta^2} = 3\,V\,B_S < 0. \tag{6.21}$$

The contributions of ΔF_{el} and ΔF_{ph} are to reduce but not to eliminate the mechanical instability.

The anisotropic structure of Earth's inner core revealed by seismological observations could be explained by the preferred orientation of the hexagonal closepacked (*hcp*) phase of iron [119], being the sound velocity along the *c*axis faster than that of *a*axis one of the evidences, which is confirmed by the inelastic Xray scattering experiment at high pressure and ambient temperature [167, 168]. An alignment of the *hcp*–Fe–Ni–Si alloy with the *c*axis parallel to the Earth's rotation axis could account for the observation of the seismic wave anisotropy of the inner core [119].

Models of Earth's interior that use information from seismic waves, and couple it with models for the inner core that consider the crystal structures of iron in it, have already been purposed [169] and are very useful for understanding the relationship between the seismic scenario and mineral physics. These models are based on the knowledge about the stability of the phases of iron, and thereof the importance of the study presented in this thesis.

The status of experimental and theoretical studies in Fe and its alloys at higher pressures and temperatures of relevance to Earth core conditions is reviewed in detail by Hirose and co-workers [121] for iron and its alloys. Consistent with them, our results point toward a close-packed crystalline structure for Earth's inner core (*hcp* and/or *fcc*), rather than *bcc*. Small amounts of lighter alloying elements such as C, O, Si and S are also expected in Earth's inner core although the exact composition of Earth's inner core is still not known. Theoretical investigations to date find that addition of these elements reduces the *hcp*-*bcc* Gibbs free energy difference, although it does not stabilize the *bcc* structure [170, 171]. Experiments also find that the *hcp* phase is stable in pure Fe and Fe-Si system at the highest pressures and temperatures that have been explored [140, 172]. On cosmochemical grounds, Ni is expected to be the most abundant alloying element. Because Ni tends to stabilize *fcc*, both fcc and *hcp* phases may coexist in the inner core, providing a possible explanation for the variation of anisotropy both laterally and with depth [173]. Very recent results indicating that *hcp* iron may be elastically isotropic at core conditions [174] provide further support for the possibility of a multi-phase inner core.

The experimental support for *bcc* phase came from Dubrovinsky *et al.* work in Fe-10wt%Ni above 225 GPa and 3400 K [128] but their results are not supported by later experiments [120, 124]. In shock studies the iron shock Hugoniot shows anomalies that were originally interpreted as *hcp*-*bcc* phase transformation, but new experiments show these anomalies are more likely due to an extended melting interval [175].

It has been proposed that the *bcc* phase may reappear just below melting temperature of iron at high pressure [128, 129, 131], perhaps stabilized by anharmonic effects as is the case for *bcc* phases of Ti, Zr, Hf [176]. Melting is well determined on the Hugoniot of iron [126, 175], and recent X-ray diffraction under ramp-compression shows that iron remains in a close-packed structure under dynamic loading to 560 GPa [123]. Also, laser-heated diamond-cell experiments with online X-ray diffraction suggest that iron remains in *hcp* structure above 4500 K at 200 GPa [122]. Some experimental support for a *bcc* phase came from work on Fe-10wt%Ni above 225 GPa and 3400 K [128], but these results are not supported by later experiments [120, 121]. Also, studies of Sakai et al. [119] for Fe (273 GPa, 4490K), and for Fe-Ni (250 GPa, 2730K) and Fe-Ni-Si (304 GPa, 2780 K) alloys reveal the *hcp* structure. Recent theoretical work (Γ point only) shows that the presence of up to 6.25 atomic percent Si or S increases the stability of *bcc* Fe at temperatures up to 7000 K, but not enough to actually stabilize this structure [147].

In summary, both theory and experiment now document the stability of close-packed (*hcp*) iron at pressures of 0.3–1.5 TPa and temperatures near the melting point. The inference is that the elastic constants of *hcp* Fe, combined with plausible deformation mechanisms for producing lattice preferred orientation in polycrystals, can explain the observed seismic structure of Earth's inner core [116, 144, 177, 178].

Chapter 7

Conclusions

7.1 Summary

Quantum mechanics provides an exact description of matter at the atomic level, but solving the exact Schrödinger for many electrons and ions is still an elusive problem, with only approximated solutions. The Density Functional Theory (Chemistry Nobel Prize 1998) provides an accurate description of reality by mapping the many-body problem onto an independent electron problem with an effective one-electron potential depending only on the electron density. However, in practice, the functional for exchange-correlation must be approximated for real materials, and approximated functionals sometimes lead to unreliable results. Such problems drive development of non-mean-field based approaches in search of even better accuracy and reliability. Nevertheless, DFT remains as a phenomenally successful approach to finding solutions to the Schrödinger equation, and its predictions have shown to be in very good agreement with the experiments repeatedly [24, 113, 179–181] and, due to that, has become a tool that is used regularly by large numbers of researchers in chemistry, physics, materials science, chemical engineering, geology, and other disciplines. This provides the base to trust DFT for predicting properties of matter not previously studied experimentally, or to generate information that would be essentially impossible to determine through experiments.

As we push the limits of pressure an temperature further, we obtain information about the behavior of materials at extreme conditions, which are needed for a better understanding of the Earth's lower mantle, as well as the internal structure and dynamics of exoplanets. The discoveries of new exoplanets continue apace and reveal an extraordinary diversity of planetary systems and exoplanet physical properties, raising new questions in the fields of planetary and material science. The accuracy of interior models of these planets has been hampered by a lack of experimental or theoretical data on the behavior of materials at high pressures. The best available equations of state (EOSs) for high-pressure materials are based on the extrapolation of experimental data [182]. Therefore, to pursue the physical properties of materials under extreme conditions and its applications to the study of the interior of solar and extrasolar planets, it is fundamental if we want to understand how planets are formed and evolve.

This thesis presents three applications of density functional theory to the study of the interior of planets, which are used to show the importance of theoretical calculations at the atomic level to understand different aspects of planetary science.

The first project (Chapter 4) provides first-principles-based results for solvation energies of silica into metallic hydrogen, to study whether the cores of giant planets can dissolve or not. Prior to this thesis, the possibility of dissolving the rocky cores of gas giants into metallic hydrogen had been studied only using magnesium oxide (MgO) and water ice (H_2O). This thesis presents a study performed on silica (SiO_2), another important candidate for rocky cores composition, showing that this material also dissolves on metallic hydrogen at megabar pressures for temperatures above

5000 K, conditions present in the core–mantle boundary of giant planets, allowing us to conclude that the rocky cores of gas giants may be dissolving. This conclusion is also supported by subsequent results that show that iron is also dissolved by metallic hydrogen, and suggest that other insulating materials may dissolve as well. Partial solvation of the core is predicted for Saturn, since its core–mantle boundary conditions lay in a range of pressures and temperatures where the solubility of SiO_2 is energetically favored, but the solubility of MgO is not. Hot Jupiters, in contrast, are expected to favor much more solubility than the giant planets of our solar system. The study presented here provides indirect evidence of the enrichment in heavy elements in giant planet atmospheres.

The second project (Chapter 5), deals with the melting of silica. Using the Z method, we have determined the melting temperature of silica at pressures not previously reported ($\geq$1000 GPa), covering the range relevant to the interior of massive rocky planets and the core–mantle boundary of gas giants. Any subsequent studies of silica at high pressures will be benefited from our results, since it places limits to the temperatures at which this material remains solid, without which overheated structures may be misinterpreted as stable solid structures in a region of temperatures that would correspond to a liquid. The phase transition of the pyrite-type to cotunnite-type SiO_2 is also questioned in view of the results of this thesis, since a stable phase of a material should correspond to the one with highest melting point [104], compared to the other structures of the same material. Our findings are not in agreement with the phase diagram presented by other authors [46, 183], since the phase boundaries they report indicate that the pyrite-cotunnite-liquid triple point takes place around 600 GPa and 9000 K, while the highest-melting-point criteria in our study indicates that the transition takes place at 480 GPa, while the cotunnite-Fe_2P-liquid triple point, according to our melting criteria, should be located around 900 GPa and 11000 K. These kinds of transitions change our understanding of how planet-forming silicates, such as perovskites, dissociate into elementary oxides at thermodynamic conditions expected in the interior of solar giants and exoplanets, and is important to study these materials in more detail in order to do more accurate predictions about the effects that these phase transitions can have in planetary science.

The third project, presented in Chapter 6, reveals that the body centered cubic structure (*bcc*) of iron should not been regarded as stable at the center of Earth. A static lattice contribution to the Helmholtz free energy is, we believe, the origin of the mechanical instability. Through the analysis of stress anisotropies, coupled with the evaluation of the Born criteria and directional mean squared displacements in both tetragonal and orthorombic strains, this study concludes that *bcc* is unstable at temperatures and pressures relevant to the Earth core. Although previous works have obtained opposite results, concluding that *bcc* iron could become more stable at Earth's core pressures [130], the work done in this thesis shows that the difference in the predictions is due to small-size efects and short simulation times, and that bigger supercells (as the 128- and 180-atoms cell we have used) and a better Brilloin zone sampling lead to more accurate results. Our findings are consistent with recent studies [121] and supported by experiments [140, 172], which support the idea that iron and its alloys should have a close-packed crystalline structure (*hcp* or *fcc*), rather than *bcc*. Although the addition of some lighter alloying elements reduces the *hcp*-*bcc* Gibbs free energy difference [170, 171], it is not enough to stabilize the *bcc* structure. The controversy of the stable phase or phases of iron at Earth's core has not yet been settled, but the more evidence we have in the same direction, the more we will know about the center of our planet and the relationship between its structure and seismic waves.

7.2 Future Research

The increasing number of exoplanets discovered has motivated further research in high pressure physics, an area that has been poorly explored for most of the materials. The more we know about materials at high pressures and temperatures, the better we understand what happens inside of planets, and in turn, the better we understand how planets are formed and evolve. Experiments performed with diamond anvil cells (DAC) have reached pressures around 300 GPa and temperatures up to 1000 K, while dynamic compression is able to reach up to 1000 GPa [84,184,185] by sending a laser-induced shock wave through a sample that is precompressed inside a diamond-anvil cell. These experiments provides information about what is happening inside planets, and confirm theoretical results comming from DFT.

Countless DFT-based studies have studied properties of materials at extreme conditions, predicting properties that have allowed to understand different phenomena inside massive rocky planets and gas giants [8,19–23,46,47,49–51,64,108,110,139,180,182,186]. The studies usually deal with simple crystals, like SiO_2, MgO, Fe, C, perovskites, or hydrogen/helium mixtures. In future projects, it is important to continuing expanding the scope DFT to even more complex materials in order to explore a wider range of planetary compositions.

In this thesis, other stoichiometries of SiO_2 have not been considered for studing its solvation into metallic hydrogen, and it has also been assumed that Si and O dissolve in a one-to-two ratio according to the charge balance. Removing these asumptions may lead to different results, and it would be interesting to consider them in future studies. Another assumption made in this thesis is that the GGA functional of Perdew, Burke and Ernzerhof properly describes the behavior of this materials at these pressures. Although previous studies show that GGA give rise to the same results as LDA for silica at these pressures [46, 183], further studies need to confirm if this holds for other properties, especially regarding to electronic properties, since it is known that DFT fails in predicting the correct structure at ambient conditions and/or accurate elastic stiffness [187]. The process of dissolution is also an interesting phenomenon that has not been analyzed either, since the rate at which these materials dissolve is not known and it is important for determining the history of gaseous planets.

Studies of melting at high pressures are still scarce, and the pressure and temperature conditions at the interior of planets are nowadays out of the realm of the experiments. Until we obtain conclusive experimental evidence in this regard, theoretical predictions are the only possible approach to study materials melting, and different techniques, such as the Z method, two phases method, and thermodynamic integration, should be compared among each other to give consistency to the predictions. The Z method still lacks of a demonstration based on thermodynamics or statistical mechanics, but has proven to be a very good approach to determine melting temperatures, specially at high pressures, since its predictions are in good agreement with the results comming from other techniques, as we have shown for silica in this thesis. The method requires an unknown waiting time for the material to melt during the simulation, and alternative methods should be developed in order to cope with it. Calculating melting curves completes the phase diagram of materials, and thus provides a degree of knowledge that is a starting point to study other properties, or phenomena directly related to melting at the interior of solar and extrasolar planets.

Lastly, a possible, important, and interesting new project could be the design of classical potentials for materials at high pressures. Quantum-mechanics-based methods, such as DFT, are limited to small system sizes compared to classical systems, due to the tremendous efforts that solving the Schrödinger equation requires. Using DFT simulations to fit an appropiate classical potential that describes a material at high pressures correctly, would allow to study other type of phenomena, such as the effect of impurities, vancancies, stacking faults, dislocations, nucleation, propagation of shockwaves, polycrystals, and other phenomena that can be studied only when a large number of atoms is considered. One approach to build such potentials is the force matching methodology proposed by Izvekov, Parrinelo, Burnham and Voth [52], which we used to calculate the classical potentials in the thermodynamic integration in chapter 4, but new techniques are appearing that seem to be simpler and promising [188]. Such a project would be important for advancing the field of computational material science.

Appendices

Appendix A

Astrophysical models

A.1 Gravitational moments

The gravitational moments J_{2n} of a planet are defined by

$$J_{2n} = -\frac{1}{M{R_{eq}}^{2n}} \iiint \rho(r,\theta) r^{2n} P_{2n}(\cos\theta)\, dV, \tag{A.1}$$

where $\rho(r,\theta)$ is the planet density at a distance r from its center and colatitude θ, M the mass of the planet, R_{eq} the equatorial radius, and P_{2n} are Legendre polynomials of order $2n$. They are related to the external gravitational potential V of the planet by

$$V(r,\theta) = -\frac{GM}{r}\left[1 - \sum_{n=1}^{\infty}\left(\frac{R_{eq}}{r}\right)^{2n} J_{2n}P_{2n}(\cos\theta)\right]. \tag{A.2}$$

The gravitational moments J_n can be measured by a spacecraft coming close to the planet, preferably on a polar orbit. Together with the mass,

$$M = \iiint \rho(r,\theta)\, dV, \tag{A.3}$$

provide a constraint on the interior density profile and the possible layering within these planets. [4, 189].

A.2 Interior structure models for solid exoplanets

The most common models for rocky planets consider a spherically symmetric and fully differentiated planet in thermal steady state and perfect mechanical equilibrium. Under these assumptions, its depth-dependent interior structure is described by the following set of coupled differential equations for mass $m(r)$, acceleration of gravity $g(r)$, and pressure $P(r)$:

$$\frac{dm}{dr} = 4\pi r^2 \rho(r), \tag{A.4}$$

$$\frac{dg}{dr} = 4\pi G\rho(r) - 2\frac{g(r)}{r}, \tag{A.5}$$

$$\frac{dP}{dr} = -\rho(r)g. \tag{A.6}$$

where r is the radial distance from the center of the planet, G is the gravitational constant, and ρ is the local density. Within the core, an adiabatic temperature distribution can be assumed, given by $dT/dr = -(\gamma g T)/\Phi$, where γ is the thermodynamic Grüneisen parameter and $\Phi = K_S/\rho$ the seismic parameter. The equation $K_S/K_T = 1 + \gamma\alpha T$ relates the adiabatic bulk modulus K_S to the isothermal bulk modulus K_T, where α is the thermal expansivity of a given material. All these equations are solved using the central boundary conditions of $m(0) = 0$, $g(0) = 0$, $P(0) = P_c$, and $T(0) = T_c$ where P_c and T_c are initial guesses for the central pressure and temperature, respectively. Integration then proceeds outward through each shell until the total mass M_p of the planet of radius R_p is achieved. If necessary, this process will start over with iteratively adjusted central pressure P_c and temperature T_c. The algorithm stops integrating if the surface boundary conditions of $m(R_p) = M_p$, $P(R_p) = P_s$, and $T(R_p) = T_s$ are met at $r = R_p$.

In these models, the local density is calculated by means of equations of state

(EOS) fitted to experimental or simulation data. For example, the third-order Birch-Murnaghan EOS,

$$P = \frac{3}{2}K_0(x^{\frac{7}{3}} - x^{\frac{5}{3}})\left[1 + \frac{3}{4}(K_0' - 4)(x^{\frac{2}{3}} - 1)\right], \tag{A.7}$$

based on the expansion of Eulerian finite strain and widely used in mineralogical and geophysical applications, is used to calculate how the density of a given material behaves with increasing pressure at a constant reference temperature. In this equation $x = \rho/\rho_0$ is the compression ratio to the ambient density ρ_0; K_0 and K_0' denote the isothermal bulk modulus and its pressure derivation at ambient conditions, respectively. Other models make use of the well known Vinet EOS,

$$P = 3K_0x^{\frac{2}{3}}(1 - x^{-\frac{1}{3}})\exp\left[\frac{2}{3}(K_0' - 1)\left(1 - x^{-\frac{1}{3}}\right)\right], \tag{A.8}$$

or some modifications like the generalized Rydberg EOS [190] or the reciprocal K' relation [191], derived from seismic data.

All these equations depend on material properties at high pressures, like ρ_0, K_0 and K_0', which can be obtained from ab initio calculations or experiments. Some applications of these models to rocky planets and how to infer the internal composition can be found in the works of Valencia [10, 11] and Wagner [12, 13].

Appendix B

Solubility

B.1 Solubility at different concentrations

When the solubility problem is addressed, a concentration must be chosen in order to calculate the Gibbs free energy of solvation, ΔG_{sol}. Once this energy has been calculated, it can be used to determine the free energy of solvation at another concentration. For the case of silica dissolved into metallic hydrogen, we have $\Delta G_{\mathrm{sol}}(\mathrm{SiO_2} : \mathrm{H}_n)$, which corresponds to the free energy of solvation at a concentration of one $\mathrm{SiO_2}$ formula unit per n hydrogen atoms. For lower concentrations, say one $\mathrm{SiO_2}$ formula unit per $m > n$ atoms of hydrogen, the free energy of solvation will be $\Delta G_{\mathrm{sol}}(\mathrm{SiO_2} : \mathrm{H}_m)$. Using equation (3.1), the energy difference between these two solvation energies will be

$$\begin{aligned}
\Delta G(n,m) &\equiv \Delta G_{\mathrm{sol}}(\mathrm{SiO_2} : \mathrm{H}_m) - \Delta G_{\mathrm{sol}}(\mathrm{SiO_2} : \mathrm{H}_n) \\
&= G(\mathrm{H}_m\mathrm{SiO_2}) - G(\mathrm{SiO_2}) - G(\mathrm{H}_m) \\
&\quad - G(\mathrm{H}_n\mathrm{SiO_2}) + G(\mathrm{SiO_2}) + G(\mathrm{H}_n) \\
&= G(\mathrm{H}_m\mathrm{SiO_2}) - G(\mathrm{H}_n\mathrm{SiO_2}) - G(\mathrm{H}_{m-n}), \qquad \text{(B.1)}
\end{aligned}$$

since $G(\mathrm{H}_m) - G(\mathrm{H}_n) = G(\mathrm{H}_{m-n})$. Now, since $dG = -S\,dT + V\,dP$, for constant T we have

$$G(\mathrm{H}_m\mathrm{SiO}_2) = F_0(\mathrm{H}_m\mathrm{SiO}_2) + PV(\mathrm{H}_m\mathrm{SiO}_2) + \int V\,dP. \tag{B.2}$$

Therefore, equation (B.1) can be expressed as

$$\begin{aligned}\Delta G(n,m) &= F_0(\mathrm{H}_m\mathrm{SiO}_2) + PV(\mathrm{H}_m\mathrm{SiO}_2) + \int V(\mathrm{H}_m\mathrm{SiO}_2)\,dP \\ &\quad -F_0(\mathrm{H}_n\mathrm{SiO}_2) - PV(\mathrm{H}_n\mathrm{SiO}_2) - \int V(\mathrm{H}_n\mathrm{SiO}_2)\,dP \\ &\quad -F_0(\mathrm{H}_{m-n}) - PV(\mathrm{H}_{m-n}) - \int V(\mathrm{H}_{m-n})\,dP. \qquad (\mathrm{B.3})\end{aligned}$$

Since $n < m$, we can make the separation $V(\mathrm{H}_m\mathrm{SiO}_2) = V(\mathrm{H}_n\mathrm{SiO}_2) + V(\mathrm{H}_{m-n})$, and write

$$\begin{aligned}\Delta G(n,m) &= F_0(\mathrm{H}_m\mathrm{SiO}_2) + PV(\mathrm{H}_n\mathrm{SiO}_2) + PV(\mathrm{H}_{m-n}) \\ &\quad + \int V(\mathrm{H}_n\mathrm{SiO}_2)\,dP + \int V(\mathrm{H}_{m-n})\,dP \\ &\quad -F_0(\mathrm{H}_n\mathrm{SiO}_2) - PV(\mathrm{H}_n\mathrm{SiO}_2) - \int V(\mathrm{H}_n\mathrm{SiO}_2)\,dP \\ &\quad -F_0(\mathrm{H}_{m-n}) - PV(\mathrm{H}_{m-n}) - \int V(\mathrm{H}_{m-n})\,dP \qquad (\mathrm{B.4}) \\ &= F_0(\mathrm{H}_m\mathrm{SiO}_2) - F_0(\mathrm{H}_n\mathrm{SiO}_2) - F_0(\mathrm{H}_{m-n}). \qquad (\mathrm{B.5})\end{aligned}$$

This means that $\Delta G(n,m)$ can be calculated only knowing the Helmholtz free energies of these 3 systems: SiO_2 dissolved into m hydrogen atoms, SiO_2 dissolved into n hydrogen atoms, and a system with $(m-n)$ hydrogen atoms.

In the ideal gas approximation, a system with N atoms of mass m, has a free energy

$$F = -Nk_BT\ln\left[\frac{eV}{N}\left(\frac{mk_BT}{2\pi\hbar^2}\right)^{\frac{3}{2}}\right], \tag{B.6}$$

therefore, for a system with N_H atoms of H, N_Si atoms of Si and N_O atoms of O, has a free energy

$$
\begin{aligned}
F_0(\mathrm{H}_{N_\mathrm{H}}\mathrm{Si}_{N_\mathrm{Si}}\mathrm{O}_{N_\mathrm{O}}) &= -kT\ln\left(\frac{Z_\mathrm{H}^{N_\mathrm{H}}}{N_\mathrm{H}!}\frac{Z_\mathrm{Si}^{N_\mathrm{Si}}}{N_\mathrm{Si}!}\frac{Z_\mathrm{O}^{N_\mathrm{O}}}{N_\mathrm{O}!}\right) \\
&= -kT\ln\left(\frac{Z_\mathrm{H}^{N_\mathrm{H}}}{N_\mathrm{H}!}\right) - kT\ln\left(\frac{Z_\mathrm{Si}^{N_\mathrm{Si}}}{N_\mathrm{Si}!}\right) - kT\ln\left(\frac{Z_\mathrm{O}^{N_\mathrm{O}}}{N_\mathrm{O}!}\right) \\
&= -N_\mathrm{H}kT\ln\left[\frac{eV}{N_\mathrm{H}}\left(\frac{m_\mathrm{H}k_BT}{2\pi\hbar^2}\right)^{\frac{3}{2}}\right] \\
&\quad -N_\mathrm{Si}kT\ln\left[\frac{eV}{N_\mathrm{Si}}\left(\frac{m_\mathrm{Si}k_BT}{2\pi\hbar^2}\right)^{\frac{3}{2}}\right] \\
&\quad -N_\mathrm{O}kT\ln\left[\frac{eV}{N_\mathrm{O}}\left(\frac{m_\mathrm{O}k_BT}{2\pi\hbar^2}\right)^{\frac{3}{2}}\right], \qquad \text{(B.7)}
\end{aligned}
$$

where m_H, m_Si and m_O are the atomic masses of hydrogen, silicon and oxigen at a volume V, and $e = \exp(1)$. Defining $A = e\left(\frac{m_\mathrm{H}k_BT}{2\pi\hbar^2}\right)^{\frac{3}{2}}$, $B = \left(\frac{m_\mathrm{Si}k_BT}{2\pi\hbar^2}\right)^{\frac{3}{2}}$, $C = \left(\frac{m_\mathrm{O}k_BT}{2\pi\hbar^2}\right)^{\frac{3}{2}}$ and using the corresponding values of N_H, N_Si, N_O in each term of equation (B.5), we can approximate these free energies by

$$
\begin{aligned}
F_0(\mathrm{H}_m\mathrm{SiO}_2) &= (-kT)\left[m\ln\left(\frac{AV_1}{m}\right) + 1\ln\left(\frac{BV_1}{1}\right) + 2\ln\left(\frac{CV_1}{2}\right)\right], \qquad \text{(B.8)} \\
F_0(\mathrm{H}_n\mathrm{SiO}_2) &= (-kT)\left[n\ln\left(\frac{AV_2}{n}\right) + 1\ln\left(\frac{BV_2}{1}\right) + 2\ln\left(\frac{CV_2}{2}\right)\right], \qquad \text{(B.9)} \\
F_0(\mathrm{H}_{m-n}) &= (-kT)\left[(m-n)\ln\left(\frac{AV_3}{m-n}\right)\right]. \qquad \text{(B.10)}
\end{aligned}
$$

Using these expressions, equation (B.5) reads

$$
\begin{aligned}
\Delta G(n,m) &= F_0(\mathrm{H}_m\mathrm{SiO}_2) - F_0(\mathrm{H}_n\mathrm{SiO}_2) - F_0(\mathrm{H}_{m-n}) \\
&= (-kT)\left[m\ln\left(\frac{AV_1}{m}\frac{(m-n)}{AV_3}\right) + n\ln\left(\frac{AV_3}{(m-n)}\frac{n}{AV_2}\right)\right. \\
&\quad \left. +\ln\left(\frac{BV_1}{BV_2}\right) + 2\ln\left(\frac{CV_1}{2}\frac{2}{CV_2}\right)\right]. \qquad \text{(B.11)}
\end{aligned}
$$

Expressing the volumes in terms of effective volumes, we have

$$
\begin{aligned}
V_1 &= mV_{\mathrm{H}} + V_{\mathrm{Si}} + 2V_{\mathrm{O}}, \\
V_2 &= nV_{\mathrm{H}} + V_{\mathrm{Si}} + 2V_{\mathrm{O}}, && \text{(B.12)} \\
V_3 &= (m-n)V_{\mathrm{H}}, && \text{(B.13)}
\end{aligned}
$$

and then,

$$
\begin{aligned}
\Delta G(n,m) &= (-kT)\left[m \ln\left(\frac{(m-n)}{m}\frac{mV_{\mathrm{H}} + V_{\mathrm{Si}} + 2V_{\mathrm{O}}}{(m-n)V_{\mathrm{H}}}\right)\right. \\
&\quad \left. + n \ln\left(\frac{n}{(m-n)}\frac{(m-n)V_{\mathrm{H}}}{nV_{\mathrm{H}} + V_{\mathrm{Si}} + 2V_{\mathrm{O}}}\right) + 3\ln\left(\frac{V_1}{V_2}\right)\right] && \text{(B.14)} \\
&= (-kT)\left[m \ln\left(\frac{mV_{\mathrm{H}} + V_{\mathrm{Si}} + 2V_{\mathrm{O}}}{mV_{\mathrm{H}}}\right)\right. \\
&\quad - n \ln\left(\frac{nV_{\mathrm{H}} + V_{\mathrm{Si}} + 2V_{\mathrm{O}}}{nV_{\mathrm{H}}}\right) \\
&\quad \left. + 3\ln\left(\frac{mV_{\mathrm{H}} + V_{\mathrm{Si}} + 2V_{\mathrm{O}}}{nV_{\mathrm{H}} + V_{\mathrm{Si}} + 2V_{\mathrm{O}}}\right)\right]. && \text{(B.15)}
\end{aligned}
$$

Then

$$
\boxed{\Delta G = (-kT)\left[m \ln\left(1 + \frac{r_1 + 2r_2}{m}\right) - n \ln\left(1 + \frac{r_1 + 2r_2}{n}\right) + 3\ln\left(\frac{m + r_1 + 2r_2}{n + r_1 + 2r_2}\right)\right]} \tag{B.16}
$$

where $r_1 = \frac{V_{\mathrm{Si}}}{V_{\mathrm{H}}}$, $r_2 = \frac{V_{\mathrm{O}}}{V_{\mathrm{H}}}$.

Appendix C

Analysis with LPMD

Las Palmeras Molecular Dynamics (LPMD) software package, is a molecular dynamics code developed during the course of this thesis, in collaboration with the Group of Nanomaterials at the Universidad de Chile, which was published [159] and uploaded to its own website, `http://www.lpmd.cl`, as a free open-source code. Although it was initially designed to perform classical molecular dynamics, its tools have proven to be very useful for handling, analyzing, creating and modifying atomic configurations of other programs. In particular, a plugin for VASP is included in the code, which allows to create crystals in the VASP cell input format (POSCAR) and analyze the corresponding output, obtaining properties such as the pair distribution function, mean squared displacement, velocity autocorrelation function, and many others in a very straightforward way.

In order to determine the structure resulting from molecular dynamic simulations, we used the Common Neighbor Analysis (CNA) technique, as proposed by Honeycutt and Andersen [166], based on nearest neighbour atoms. With this technique they could describe the structural transition in small clusters with increasing size from icosahedral structure, to polyicosahedral to face-centered cubic. Faken and Jónsson [192], used a slightly different version of CNA in combination with 3D computer graphics to study the crystal nucleation in a molten copper slab. In the original CNA method [166] proposed by Honeycutt and Andersen a structure is represented by diagrams. Starting with a pair of atoms, α and β, the diagram is classified by a set of four indices: i, j, k, and l. The first index i, with values 1 or 2, indicates if α and β are nearest-neighbours ($i = 1$) or not ($i = 2$). The index j is the number of neighbours shared by common neighbours α and β. The third index, k, is the number of bonds that can be formed between these j common neighbours and the fourth index, l, denotes the number of bonds in the longest continuous chain formed by the k bonds. Two atoms are nearest neighbours if the distance between them is less or equal to a cutoff distance, which is defined as the first minimum in the pair distribution function.

In Figs. 31(a)–(d) we illustrate the four indices used in CNA classification with diagrams of few selected structures. Fig. 31(a) shows the 1421 diagram, present in the *fcc* structure, formed by a pair of nearest neighbour atoms, sharing 4 common neighbours having two bonds. Fig. 31(b) represents the 1422 diagram present in *hcp* structure with same amount as in 1421 diagram. Fig. 31(c) and (d) show the 1444 and 1666 diagrams which are found in the *bcc* structure.

For a given perfect crystal structure, the presence of CNA diagrams is well determined as observed in Table C.1 and can be used to distinguish them. All pairs of nearest neighbour atoms in the *fcc* structure form diagrams of the type 1421. In the *hcp* structure half the pairs of nearest neighbour atoms form 1421 while the other half form 1422 diagrams. The *bcc* structure has an unbalanced distribution of diagrams with 3/7 of the nearest neighbour atoms pairs forming 1444 diagrams while the rest 4/7 forming 1666 diagrams. As we refer only to bonded atoms with first neighbours coordination, $i = 1$ is ommited and we use only jkl indices to identify

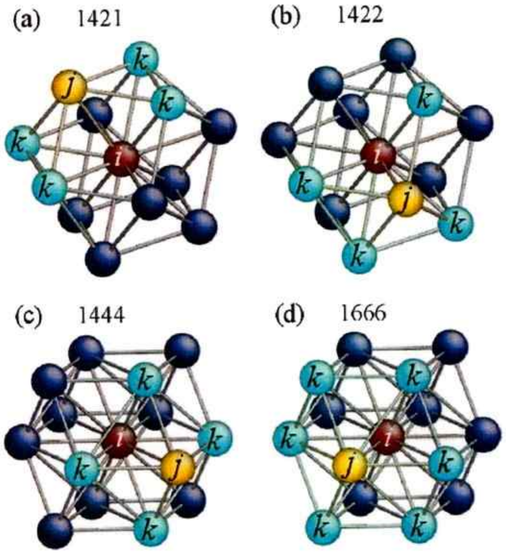

Fig. 31: Illustrations of diagrams constructed from the classification of local structures defined in the CNA method. Brown (i) and yellow (j) atoms indicate one pair of nearest neighbour atoms, light-blue (k) atoms are common neighbours of the brown-yellow pair. (a) shows a 1421 diagram, indicating that brown (i) and yellow (j) atoms are nearest neighbours with 4 common neighbours (k) having two bonds. 1421 is the only diagram present in *fcc* structure. (b)–(d) showing 1422, 1444, and 1666 diagrams are found in the *hcp* and *bcc* structures (figure provided by Tsuzuki *et al.* [193]).

the structure.

CNA diagram	*fcc*	*bcc*	*hcp*
1421	1	0	0.5
1422	0	0	0.5
1444	0	3/7	0
1666	0	4/7	0

Table C.1: Relative presence of different CNA diagrams in the *fcc*, *bcc*, and *hcp* crystal structures

Appendix D

Tetragonal Strain

In elastic strain theory [194], when a strain is performed over a solid with orthonormal vectors $\hat{\mathbf{x}}, \hat{\mathbf{y}}, \hat{\mathbf{z}}$ embedded in it, the new axes are written in terms of the old axes:

$$\begin{aligned} \mathbf{x}' &= (1+\epsilon_{xx})\hat{\mathbf{x}} + \epsilon_{xy}\hat{\mathbf{y}} + \epsilon_{xz}\hat{\mathbf{z}}; \\ \mathbf{y}' &= \epsilon_{yx}\hat{\mathbf{x}} + (1+\epsilon_{yy})\hat{\mathbf{y}} + \epsilon_{yz}\hat{\mathbf{z}}; \\ \mathbf{z}' &= \epsilon_{zx}\hat{\mathbf{x}} + \epsilon_{zy}\hat{\mathbf{y}} + (1+\epsilon_{zz})\hat{\mathbf{z}}. \end{aligned} \tag{D.1}$$

These coefficients form the strain tensor, given by

$$\varepsilon = \begin{pmatrix} \epsilon_{xx} & \epsilon_{xy} & \epsilon_{xz} \\ \epsilon_{yx} & \epsilon_{yy} & \epsilon_{yz} \\ \epsilon_{zx} & \epsilon_{zy} & \epsilon_{zz} \end{pmatrix}. \tag{D.2}$$

Under tetragonal distortions performed over a crystal with Bravais lattice vectors $\mathbf{a} = a\hat{\mathbf{x}}$, $\mathbf{b} = b\hat{\mathbf{y}}$, $\mathbf{c} = c\hat{\mathbf{z}}$, the strain tensor becomes

$$\varepsilon = \begin{pmatrix} x & 0 & 0 \\ 0 & x & 0 \\ 0 & 0 & \delta \end{pmatrix}, \tag{D.3}$$

and the new lattice vectors,

$$\begin{aligned} \mathbf{a}' &= (1+x)a\hat{\mathbf{x}}, \\ \mathbf{b}' &= (1+x)b\hat{\mathbf{y}}, \\ \mathbf{c}' &= (1+\delta)c\hat{\mathbf{z}}. \end{aligned} \tag{D.4}$$

For presserving the volume in the deformation, we require that $V = abc$ equals $V' = a'b'c' = (1+x)^2(1+\delta)abc$, which leads to

$$x = (1+\delta)^{-\frac{1}{2}} - 1, \tag{D.5}$$

and we, therefore, obtain a strain tensor given in terms of a single parameter, δ:

$$\varepsilon = \begin{pmatrix} (1+\delta)^{-\frac{1}{2}} - 1 & 0 & 0 \\ 0 & (1+\delta)^{-\frac{1}{2}} - 1 & 0 \\ 0 & 0 & \delta \end{pmatrix}. \tag{D.6}$$

The size of the new lattice vectors in (D.4) can also be written in terms of δ:

$$\begin{aligned} a' &= (1+\delta)^{-\frac{1}{2}}a \\ b' &= (1+\delta)^{-\frac{1}{2}}b, \\ c' &= (1+\delta)c, \end{aligned} \tag{D.7}$$

from where we get the relationship

$$\frac{c'}{a'} = (1+\delta)^{\frac{3}{2}}\frac{c}{a}. \tag{D.8}$$

For the special case in which the initial cell is cubic, like *bcc*, $c = a$, therefore,

$$\frac{c'}{a'} = (1+\delta)^{\frac{3}{2}}. \tag{D.9}$$

Bibliography

[1] Mayor, M. & Queloz, D. A Jupiter-mass companion to a solar-type star. *Nature* **378**, 355–359 (1995).

[2] Schneider, J. The Extrasolar Planet Encyclopaedia (2011). URL `http://exoplanet.eu/catalog.php`.

[3] Guillot, T. Interiors of giant planets inside and outside the solar system. *Science* **286**, 72 (1999).

[4] Leconte, J. & Chabrier, G. A new vision of giant planet interiors: Impact of double diffusive convection. *Astronomy & Astrophysics* **540**, A20 (2012).

[5] Fortney, J. J., Ikoma, M., Nettelmann, N., Guillot, T. & Marley, M. S. Self-Consistent Model Atmospheres and the Cooling of the Solar System'S Giant Planets. *The Astrophysical Journal* **729**, 32 (2011).

[6] Saumon, D., Chabrier, G. & van Horn, H. M. An Equation of State for Low-Mass Stars and Giant Planets. *The Astrophysical Journal Supplement Series* **99**, 713 (1995).

[7] Saumon, D. & Guillot, T. Shock Compression of Deuterium and the Interiors of Jupiter and Saturn. *The Astrophysical Journal* **609**, 1170–1180 (2004).

[8] Militzer, B., Hubbard, W. B., Vorberger, J., Tamblyn, I. & Bonev, S. A. A Massive Core in Jupiter Predicted from First-Principles Simulations. *The Astrophysical Journal* **688**, L45–L48 (2008).

[9] Nettelmann, N., Becker, A., Holst, B. & Redmer, R. Jupiter Models with Ab Initio Hydrogen equation of state (H-REOS.2). *The Astrophysical Journal* **750**, 52 (2012).

[10] Valencia, D., O'Connell, R. J. & Sasselov, D. Internal structure of massive terrestrial planets. *Icarus* **181**, 545–554 (2006).

[11] Valencia, D., Ikoma, M., Guillot, T. & Nettelmann, N. Composition and fate of short-period super-Earths. *Astronomy and Astrophysics* **516**, A20 (2010).

[12] Wagner, F., Sohl, F., Hussmann, H., Grott, M. & Rauer, H. Interior structure models of solid exoplanets using material laws in the infinite pressure limit. *Icarus* **214**, 366–376 (2011).

[13] Wagner, F. W., Tosi, N., Sohl, F., Rauer, H. & Spohn, T. Rocky super-Earth interiors. *Astronomy & Astrophysics* **541**, A103 (2012).

[14] Sholl, D. & Steckel, J. *Density Functional Theory: A Practical Introduction* (Wiley, Hoboken, New Jersey, 2011).

[15] Hohenberg, P. & Kohn, W. Inhomogeneous Electron Gas. *Physical Review* **136**, B864–B871 (1964).

[16] Kohn, W. & Sham, L. J. Self-Consistent Equations Including Exchange and Correlation Effects. *Physical Review* **140**, A1133–A1138 (1965).

[17] Hoover, W. Canonical dynamics: Equilibrium phase-space distributions. *Physical Review A* **31**, 1695–1697 (1985).

[18] Alfè, D., Gilland, M. J. & Price, G. D. The melting curve of iron at the pressures of the earth's core from ab initio calculations. *Nature* **401**, 462 (1999).

[19] Morales, M. A. *et al.* Phase separation in hydrogen-helium mixtures at mbar pressures. *PNAS* **106**, 1324 (2009).

[20] Wilson, H. F. & Militzer, B. Sequestration of noble gases in giant planet interiors. *Phys. Rev. Lett.* **104**, 121101 (2010).

[21] Wilson, H. & Militzer, B. Rocky Core Solubility in Jupiter and Giant Exoplanets. *Physical Review Letters* **108**, 111101 (2012).

[22] Wilson, H. F. & Militzer, B. Solubility of Water Ice in Metallic Hydrogen: Consequences for Core Erosion in Gas Giant Planets. *Astrophys. J.* **745**, 54 (2012).

[23] Militzer, B. Equation of state calculations of hydrogen-helium mixtures in solar and extrasolar giant planets. *Phys. Rev. B* **87**, 014202 (2013).

[24] Sugino, O. & Car, R. Ab Initio Molecular Dynamics Study of First-Order Phase Transitions: Melting of Silicon. *Physical Review Letters* **74**, 1823–1826 (1995).

[25] Frenkel, D. & Smit, B. *Understanding Molecular Simulation: From Algorithms to Applications* (Elsevier, 1996).

[26] Kerley, G. Structures of the planets Jupiter and Saturn. *Research Rep.* **KTS-04-1** (2004).

[27] Niemann, H. B. *et al.* The Galileo Probe Mass Spectrometer: Composition of Jupiter's Atmosphere. *Science* **272**, 846 (1996).

[28] Mahaffy, P. R. *et al.* Heavy noble gases in the atmosphere of jupiter. *Bull. Am. Astron. Soc.* **30**, 1066 (1998).

[29] Armitage, P. J. *Astrophysics of planet formation* (Cambridge University Press, New York, 2010).

[30] Davidson, J. *et al.* Abundances of presolar silicon carbide grains in primitive meteorites determined by NanoSIMS. *Geochimica et Cosmochimica Acta* (2014).

[31] Elkins-Tanton, L. T. & Seager, S. Ranges of Atmospheric Mass and Composition of Super-Earth Exoplanets. *The Astrophysical Journal* **685**, 1237–1246 (2008).

[32] Batalha, N. M., Rowe, J. F. & et. al, S. T. B. Planetary Candidates Observed by Kepler. III. Analysis of the First 16 Months of Data. *The Astrophysical Journal Supplement Series* **204**, 24 (2013).

[33] Charbonneau, D. *et al.* A super-Earth transiting a nearby low-mass star. *Nature* **462**, 891–894 (2009).

[34] Mizuno, H., Nakazawa, K. & Hayashi, C. Instability of a gaseous envelope surrounding a planetary core and formation of giant planets. *Prog. Theor. Phys.* **60**, 699 (1978).

[35] Fortney, J. J. & Nettelmann, N. The Interior Structure, Composition, and Evolution of Giant Planets. *Space Science Reviews* **152**, 423–447 (2009).

[36] Guillot, T., Stevenson, D. J., Hubbard, W. B. & Saumon, D. *The interior of Jupiter*, 35–57 (Cambridge University Press, 2004).

[37] Stevenson, D. J. Formation of the giant planets. *Planet. Space. Sci* **30**, 755 (1982).

[38] Leconte, J. & Chabrier, G. Layered convection as the origin of Saturn's luminosity anomaly. *Nature Geoscience* **6**, 347 (2013).

[39] Chabrier, G. & Baraffe, I. Heat Transport in Giant (Exo)planets: A New Perspective. *The Astrophysical Journal* **661**, L81–L84 (2007).

[40] Belonoshko, A. & Dubrovinsky, L. S. Molecular dynamics of stishovite melting. *Geochimica et cosmochimica acta* **59**, 1883–1889 (1995).

[41] Boates, B. & Bonev, S. A. Demixing Instability in Dense Molten $MgSiO_3$ and the Phase Diagram of MgO. *Physical Review Letters* **110**, 135504 (2013).

[42] Hicks, D. G. *et al.* Dissociation of liquid silica at high pressures and temperatures. *Phys. Rev. Lett.* **97**, 025502 (2006).

[43] Kuwayama, Y., Hirose, K., Sata, N. & Ohishi, Y. The pyrite-type high-pressure form of silica. *Science (New York, N.Y.)* **309**, 923–5 (2005).

[44] Luo, S.-N., Çağin, T., Strachan, A., Goddard, W. A. & Ahrens, T. J. Molecular dynamics modeling of stishovite. *Earth and Planetary Science Letters* **202**, 147–157 (2002).

[45] Schaefer, L. & Fegley, B. Chemistry of Silicate Atmospheres of Evaporating Super-Earths. *The Astrophysical Journal* **703**, L113–L117 (2009).

[46] Tsuchiya, T. & Tsuchiya, J. Prediction of a hexagonal SiO_2 phase affecting stabilities of $MgSiO_3$ and $CaSiO_3$ at multimegabar pressures. *Proceedings of the National Academy of Sciences of the United States of America* **108**, 1252–5 (2011).

[47] Umemoto, K., Wentzcovitch, R. M. & Allen, P. B. Dissociation of $MgSiO_3$ in the cores of gas giants and terrestrial exoplanets. *Science (New York, N.Y.)* **311**, 983–6 (2006).

[48] Usui, Y. & Tsuchiya, T. Ab initio two-phase molecular dynamics on the melting curve of SiO_2. *Journal of Earth Science* **21**, 801–810 (2010).

[49] Wahl, S. M., Wilson, H. F. & Militzer, B. Solubility of Iron in Metallic Hydrogen and Stability of Dense Cores in Giant Planets. *The Astrophysical Journal* **773**, 95 (2013).

[50] Militzer, B. & Wilson, H. F. New phases of water ice predicted at megabar pressures. *Phys. Rev. Lett.* **105**, 195701 (2010).

[51] Zhang, S., Wilson, H. F., Driver, K. P. & Militzer, B. H_4O and other hydrogen-oxygen compounds at giant-planet core pressures. *Physical Review B* **87**, 024112 (2013).

[52] Izvekov, S., Parrinello, M., Burnham, C. J. & Voth, G. A. Effective force fields for condensed phase systems from *ab initio* molecular dynamics simulation: A new method for force-matching. *J. Chem. Phys.* **120**, 10896 (2004).

[53] Tangney, P. & Scandolo, S. An ab initio parametrized interatomic force field for silica. *The Journal of Chemical Physics* **117**, 8898 (2002).

[54] Blochl, P. E. Projector augmented-wave method. *Phys. Rev. B* **50**, 17953 (1994).

[55] Kresse, G. & Furthmüller, J. Efficient iterative schemes for ab initio total-energy calculations using a plane-wave basis set. *Phys. Rev. B* **54**, 11169 (1996).

[56] Perdew, J. P., Burke, K. & Ernzerhof, M. Generalized gradient approximation made simple. *Phys. Rev. Lett.* **77**, 3865 (1996).

[57] Monkhorst, H. J. & Pack, J. D. Special points for brillouin-zone integrations. *Phys. Rev. B* **13**, 5188–5192 (1976).

[58] Mermin, N. D. Thermal properties of the inhomogeneous electron gas. *Phys. Rev.* **137**, A1441–A1443 (1965).

[59] González-Cataldo, F., Davis, S. & Gutiérrez, G. Melting of SiO_2 at multi-megabar pressures: implications for gas giants and super-Earths. *Proceedings of the National Academy of Sciences* (2014). Submitted.

[60] Guillot, T. Interiors of Giant Planets Inside and Outside the Solar System. *Science* **286**, 72–77 (1999).

[61] Burrows, A. A theoretical look at the direct detection of giant planets outside the Solar System. *Nature* **433**, 261–8 (2005).

[62] Seager, S., Kuchner, M., Hier-Majumder, C. A. & Militzer, B. Mass-Radius Relationships for Solid Exoplanets. *The Astrophysical Journal* **669**, 1279–1297 (2007).

[63] Swift, D. C. *et al.* Mass-radius relationships for exoplanets. *The Astrophysical Journal* **744**, 59 (2012).

[64] Militzer, B. & Hubbard, W. B. Ab Initio Equation of State for Hydrogen-Helium Mixtures With Recalibration of the Giant-Planet Mass-Radius Relation. *The Astrophysical Journal* **774**, 148 (2013).

[65] Hubbard, W. & Marley, M. S. Optimized Jupiter, Saturn, and Uranus interior models. *Icarus* **78**, 102–118 (1989).

[66] Howard, A. W. *et al.* A rocky composition for an Earth-sized exoplanet. *Nature* **503**, 381–4 (2013).

[67] Léger, A. *et al.* The extreme physical properties of the CoRoT-7b super-Earth. *Icarus* **213**, 1–11 (2011).

[68] Baraffe, I., Chabrier, G., Fortney, J. & Sotin, C. Planetary internal structures. *ArXiv e-prints* (2014). `1401.4738`.

[69] Lindemann, F. A. The calculation of molecular vibration frequencies. *Phys. Z.* **11**, 609 (1910).

[70] Born, M. Thermodynamics of Crystals and Melting. *The Journal of Chemical Physics* **7**, 591 (1939).

[71] Levien, L., Prewitt, C. T. & Weidner, D. J. Structure and elastic properties of quartz at pressure. *American Mineralogist* **65**, 920–930 (1980).

[72] Levien, L. & Prewitt, C. T. High-pressure crystal structure and compressibility of coesite. *American Mineralogist* **66**, 324–333 (1981).

[73] Ross, N. L., Shu, J. & Hazen, R. M. High-pressure crystal chemistry of stishovite. *American Mineralogist* **75**, 739–747 (1990).

[74] Kingma, K. J., Cohen, R. E., Hemley, R. J. & Mao, H.-k. Transformation of stishovite to a denser phase at lower-mantle pressures. *Nature* **374**, 243–245 (1995).

[75] Togo, A., Oba, F. & Tanaka, I. First-principles calculations of the ferroelastic transition between rutile-type and CaCl2-type SiO2 at high pressures. *Physical Review B* **78**, 134106 (2008).

[76] Chao, E. C. T., Fahey, J. J., Littler, J. & Milton, D. J. Stishovite, SiO_2 , a very high pressure new mineral from Meteor Crater, Arizona. *Journal of Geophysical Research* **67**, 419–421 (1962).

[77] Goresy, A. E., Dubrovinsky, L. S., Sharp, T. G., Saxena, S. & Chen, M. A Monoclinic Post-Stishovite Polymorph of Silica in the Shergotty Meteorite. *Science* **288**, 1632–1634 (2000).

[78] Dubrovinsky, L. *et al.* Pressure-induced transformations of cristobalite. *Chemical Physics Letters* **333**, 264–270 (2001).

[79] Oganov, A., Gillan, M. & Price, G. Structural stability of silica at high pressures and temperatures. *Physical Review B* **71**, 064104 (2005).

[80] Jackson, I. Melting of the silica isotypes SiO2, BeF2 and GeO2 at elevated pressures. *Physics of the Earth and Planetary Interiors* **13**, 218–231 (1976).

[81] Zhang, J., Liebermann, R. C., Gasparik, T., Herzberg, C. T. & Fei, Y. Melting and subsolidus relations of SiO_2 at 9–14 GPa. *Journal of Geophysical Research* **98**, 19785 (1993).

[82] Belonoshko, A. Molecular dynamics of silica at high pressures: Equation of state, structure, and phase transitions. *Geochimica et cosmochimica acta* **58** (1994).

[83] Hudon, P., Jung, I.-H. & Baker, D. R. Melting of β-quartz up to 2.0 GPa and thermodynamic optimization of the silica liquidus up to 6.0 GPa. *Physics of the Earth and Planetary Interiors* **130**, 159–174 (2002).

[84] Correa, A., Bonev, S. A. & Galli, G. Carbon under extreme conditions: phase boundaries and electronic properties from first-principles theory. *Proceedings of the National Academy of Sciences of the United States of America* **103**, 1204–8 (2006).

[85] Belonoshko, A., Ahuja, R. & Johansson, B. Quasi-Ab initio molecular dynamic study of Fe melting. *Physical review letters* **84**, 3638–41 (2000).

[86] Morris, J., Wang, C., Ho, K. & Chan, C. Melting line of aluminum from simulations of coexisting phases. *Physical Review B* **49**, 3109–3115 (1994).

[87] Cazorla, C., Gillan, M. J., Taioli, S. & Alfè, D. Melting curve and Hugoniot of molybdenum up to 400 GPa by ab initio simulations. *Journal of Physics: Conference Series* **121**, 012009 (2008).

[88] Alfè, D., Cazorla, C. & Gillan, M. J. The kinetics of homogeneous melting beyond the limit of superheating. *The Journal of chemical physics* **135**, 024102 (2011).

[89] Belonoshko, A., Skorodumova, N., Rosengren, A. & Johansson, B. Melting and critical superheating. *Physical Review B* **73**, 012201 (2006).

[90] Belonoshko, A. *et al.* Properties of the fcc Lennard-Jones crystal model at the limit of superheating. *Physical Review B* **76**, 064121 (2007).

[91] Belonoshko, A. *et al.* Molybdenum at High Pressure and Temperature: Melting from Another Solid Phase. *Physical Review Letters* **100**, 135701 (2008).

[92] Belonoshko, A., Arapan, S., Martonak, R. & Rosengren, A. MgO phase diagram from first principles in a wide pressure-temperature range. *Physical Review B* **81**, 054110 (2010).

[93] Belonoshko, a. B. & Rosengren, a. High-pressure melting curve of platinum from ab initio Z method. *Physical Review B* **85**, 174104 (2012).

[94] Benazzouz, B. K., Zaoui, A. & Belonoshko, A. B. Determination of the melting temperature of kaolinite by means of the Z-method. *American Mineralogist* **98**, 1881–1885 (2013).

[95] Bouchet, J., Bottin, F., Jomard, G. & Zérah, G. Melting curve of aluminum up to 300 GPa obtained through ab initio molecular dynamics simulations. *Physical Review B* **80**, 094102 (2009).

[96] Burakovsky, L. *et al.* High-Pressure–High-Temperature Polymorphism in Ta: Resolving an Ongoing Experimental Controversy. *Physical Review Letters* **104**, 255702 (2010).

[97] Burakovsky, L., Chen, S. P., Preston, D. L. & Sheppard, D. G. Z methodology for phase diagram studies: platinum and tantalum as examples. *Journal of Physics: Conference Series* **500**, 162001 (2014).

[98] Davis, S., Belonoshko, A., Johansson, B., Skorodumova, N. V. & van Duin, A. C. T. High-pressure melting curve of hydrogen. *The Journal of chemical physics* **129**, 194508 (2008).

[99] Davis, S., Belonoshko, A. B., Rosengren, A., van Duin, A. C. & Johansson, B. Molecular dynamics simulation of zirconia melting. *Central European Journal of Physics* **8**, 789–797 (2010).

[100] Davis, S., Belonoshko, A., Johansson, B. & Rosengren, A. Model for diffusion at the microcanonical superheating limit from atomistic computer simulations. *Physical Review B* **84**, 064102 (2011).

[101] Davis, S. & Gutiérrez, G. Bayesian inference as a tool for analysis of first-principles calculations of complex materials: an application to the melting point of Ti_2GaN. *Modelling and Simulation in Materials Science and Engineering* **21**, 075001 (2013).

[102] Finney, A. R. & Rodger, P. M. Applying the z method to estimate temperatures of melting in structure ii clathrate hydrates. *Phys. Chem. Chem. Phys.* **13**, 19979–19987" (2011).

[103] Li, D., Zhang, P., Yan, J. & Liu, H. Y. Melting curve of lithium from quantum molecular-dynamics simulations. *EPL (Europhysics Letters)* **95**, 56004 (2011).

[104] Li, D., Zhang, P. & Yan, J. Ab initio molecular dynamics study of high-pressure melting of beryllium oxide. *Scientific reports* **4**, 4707 (2014).

[105] Moriarty, J. a., Hood, R. Q. & Yang, L. H. Quantum-Mechanical Interatomic Potentials with Electron Temperature for Strong-Coupling Transition Metals. *Physical Review Letters* **108**, 036401 (2012).

[106] Sun, J., Martinez-Canales, M., Klug, D. D., Pickard, C. J. & Needs, R. J. Stable All-Nitrogen Metallic Salt at Terapascal Pressures. *Physical Review Letters* **111**, 175502 (2013).

[107] Kechin, V. Melting curve equations at high pressure. *Physical Review B* **65**, 052102 (2001).

[108] González-Cataldo, F., Wilson, H. F. & Militzer, B. Ab Initio Free Energy Calculations of the Solubility of Silica in Metallic Hydrogen and Application To Giant Planet Cores. *The Astrophysical Journal* **787**, 79 (2014).

[109] Tallon, J. L. The entropy change on melting of simple substances. *Physics Letters A* **76**, 139 – 142 (1980).

[110] Morard, G., Bouchet, J., Valencia, D., Mazevet, S. & Guyot, F. The melting curve of iron at extreme pressures: Implications for planetary cores. *High Energy Density Physics* **7**, 141–144 (2011).

[111] Stamenković, V. & Breuer, D. The tectonic mode of rocky planets: Part 1 Driving factors, models & parameters. *Icarus* **234**, 174–193 (2014).

[112] Valencia, D., O'Connell, R. J. & Sasselov, D. D. Inevitability of Plate Tectonics on Super-Earths. *The Astrophysical Journal* **670**, L45–L48 (2007).

[113] Alfè, D. Melting Curve of MgO from First-Principles Simulations. *Physical Review Letters* **94**, 235701 (2005).

[114] Lehmann, I. P'. *Publ. Bur. Cent. Assoc. Int. Seismol. A* **14**, 3 (1936).

[115] Poirier, J. *Introduction to the Physics of the Earth's Interior* (Cambridge University Press, 2000).

[116] Morelli, A., Dziewonski, A. M. & Woodhouse, J. H. Anisotropy of the inner core inferred from PKIKP travel times. *Geophysical Research Letters* **13**, 1545–1548 (1986).

[117] Pickard, C. J. & Needs, R. J. Stable phases of iron at terapascal pressures. *Journal of Physics: Condensed Matter* **21**, 452205 (2009).

[118] Stixrude, L. Structure of Iron to 1Gbar and 40000K. *Physical Review Letters* **108**, 055505 (2012).

[119] Sakai, T., Ohtani, E., Hirao, N. & Ohishi, Y. Stability field of the hcp-structure for Fe, Fe-Ni, and Fe-Ni-Si alloys up to 3 Mbar. *Geophysical Research Letters* **38**, L09302 (2011).

[120] Tateno, S., Hirose, K., Komabayashi, T., Ozawa, H. & Ohishi, Y. The structure of Fe-Ni alloy in Earth's inner core. *Geophysical Research Letters* **39**, L12305 (2012).

[121] Hirose, K., Labrosse, S. & Hernlund, J. Composition and state of the core. *Annual Review of Earth and Planetary Sciences* **41**, 657–691 (2013).

[122] Anzellini, S., Dewaele, A., Mezouar, M., Loubeyre, P. & Morard, G. Melting of Iron at Earth's Inner Core Boundary Based on Fast X-ray Diffraction. *Science* **340**, 464–466 (2013).

[123] Ping, Y. *et al.* Solid Iron Compressed Up to 560 GPa. *Phys. Rev. Lett.* **111**, 065501 (2013).

[124] Sakai, T., Ohtani, E., Hirao, N. & Ohishi, Y. Stability field of the hcp-structure for Fe, Fe-Ni, and Fe-Ni-Si alloys up to 3 mbar. *Geophysical Research Letters* **38**, L09302 (2011).

[125] Song, X. & Helmberger, D. V. Seismic evidence for an inner core transition zone. *Science* **282**, 924–927 (1998).

[126] Brown, J. M. & McQueen, R. G. Phase transitions, Grüneisen parameter, and elasticity for shocked iron between 77 GPa and 400 GPa. *Journal of Geophysical Research: Solid Earth* **91**, 7485–7494 (1986).

[127] Boehler, R. Temperatures in the Earth's core from melting-point measurements of iron at high static pressures. *Nature* **363**, 534 (1993).

[128] Dubrovinsky, L. *et al.* Body-centered cubic iron-nickel alloy in earth's core. *Science* **316**, 1880–1883 (2007).

[129] Ross, M., Young, D. A. & Grover, R. Theory of the iron phase diagram at earth core conditions. *Journal of Geophysical Research: Solid Earth* **95**, 21713–21716 (1990).

[130] Vočadlo, L. *et al.* Possible thermal and chemical stabilization of body-centred-cubic iron in the earth's core. *Nature* **424**, 536–539 (2003).

[131] Belonoshko, A. B., Ahuja, R. & Johansson, B. Stability of the body-centred-cubic phase of iron in the earth's inner core. *Nature* **424**, 1032–1034 (2003).

[132] Vočadlo, L. *et al.* The stability of bcc-Fe at high pressures and temperatures with respect to tetragonal strain. *Physics of the Earth and Planetary Interiors* **170**, 52–59 (2008).

[133] Luo, W. *et al.* Dynamical stability of body center cubic iron at the earths core conditions. *Proceedings of the National Academy of Sciences* **107**, 9962–9964 (2010).

[134] Kong, L. T., Li, J. F., Shi, Q. W., Huang, H. J. & Zhao, K. Dynamical stability of iron under high-temperature and high-pressure conditions. *Europhysics Letters* **97**, 56004 (2012).

[135] Belonoshko, A. B., Isaev, E. I., Skorodumova, N. V. & Johansson, B. Stability of the body-centered-tetragonal phase of Fe at high pressure: Ground-state energies, phonon spectra, and molecular dynamics simulations. *Phys. Rev. B* **74**, 214102 (2006).

[136] Belonoshko, A. *et al.* Origin of the low rigidity of the Earth's inner core. *Science (New York, N.Y.)* **316**, 1603–5 (2007).

[137] Belonoshko, A. B., Skorodumova, N. V., Rosengren, A. & Johansson, B. Elastic anisotropy of earth's inner core. *Science* **319**, 797–800 (2008).

[138] Belonoshko, A. B. *et al.* Quenching of bcc-fe from high to room temperature at high-pressure conditions: a molecular dynamics simulation. *New Journal of Physics* **11**, 093039 (2009).

[139] Bouchet, J., Mazevet, S., Morard, G., Guyot, F. & Musella, R. Ab initio equation of state of iron up to 1500 GPa. *Physical Review B* **87**, 094102 (2013).

[140] Tateno, S., Hirose, K., Ohishi, Y. & Tatsumi, Y. The Structure of Iron in Earth's Inner Core. *Science* **330**, 359–361 (2010).

[141] Wang, J. *et al.* Ramp compression of iron to 273 GPa. *Journal of Applied Physics* **114**, 023513 (2013).

[142] Deming, D. Extrasolar planets: An infernal Earth. *Nature* **2**, 217–20 (2013).

[143] Petigura, E. A., Howard, A. W. & Marcy, G. W. Prevalence of Earth-size planets orbiting Sun-like stars. *Proceedings of the National Academy of Sciences* **110**, 19273–19278 (2013).

[144] Stixrude, L. & Cohen, R. E. High-pressure elasticity of iron and anisotropy of earth's inner core. *Science* **267**, 1972–1975 (1995).

[145] Vočadlo, L. Ab initio calculations of the elasticity of iron and iron alloys at inner core conditions: Evidence for a partially molten inner core? *Earth and Planetary Science Letters* **254**, 227 – 232 (2007).

[146] Stixrude, L., Cohen, R. E. & Singh, D. J. Iron at high pressure: Linearized-augmented-plane-wave computations in the generalized-gradient approximation. *Phys. Rev. B* **50**, 6442–6445 (1994).

[147] Cui, H., Zhang, Z. & Zhang, Y. The effect of si and s on the stability of bcc iron with respect to tetragonal strain at the earth's inner core conditions. *Geophysical Research Letters* **40**, 2958–2962 (2013).

[148] Kresse, G. & Joubert, D. From ultrasoft pseudopotentials to the projector augmented-wave method. *Phys. Rev. B* **59**, 1758–1775 (1999).

[149] Blöchl, P. E., Jepsen, O. & Andersen, O. K. Improved tetrahedron method for brillouin-zone integrations. *Phys. Rev. B* **49**, 16223–16233 (1994).

[150] Bain, E. The nature of martensite. *Transactions of the American Institute of Mining, Metallurgical, and Petroleum Engineers* **70**, 25–46 (1924).

[151] Akahama, Y., Kawamura, H. & Le Bihan, T. New δ (distorted-bcc) titanium to 220 gpa. *Phys. Rev. Lett.* **87**, 275503 (2001).

[152] Verma, A. K., Modak, P., Rao, R. S., Godwal, B. K. & Jeanloz, R. High-pressure phases of titanium: First-principles calculations. *Phys. Rev. B* **75**, 014109 (2007).

[153] Flyvbjerg, H. & Petersen, H. G. Error estimates on averages of correlated data. *The Journal of Chemical Physics* **91**, 461–466 (1989).

[154] Adams, D. J. & Oganov, A. R. *Ab initio* molecular dynamics study of $CaSiO_3$ perovskite at *P-T* conditions of Earth's lower mantle. *Phys. Rev. B* **73**, 184106 (2006).

[155] Ruban, A. V., Belonoshko, A. B. & Skorodumova, N. V. Impact of magnetism on Fe under Earth's core conditions. *Phys. Rev. B* **87**, 014405 (2013).

[156] Mehl, M. J., Aguayo, A., Boyer, L. L. & de Coss, R. Absence of metastable states in strained monatomic cubic crystals. *Phys. Rev. B* **70**, 014105 (2004).

[157] Stixrude, L. & Cohen, R. E. Constraints on the crystalline structure of the inner core: Mechanical instability of bcc iron at high pressure. *Geophysical Research Letters* **22**, 125–128 (1995).

[158] Mikhaylushkin, A. S., Abrikosov, I. A., Belonoshko, A. B., Johansson, B. & Simak, S. I. Instability of the body-centered tetragonal phase of iron under extreme conditions. *Phys. Rev. B* **79**, 132106 (2009).

[159] Davis, S., Loyola, C., González, F. & Peralta, J. Las Palmeras Molecular Dynamics: A flexible and modular molecular dynamics code. *Computer Physics Communications* **181**, 2126–2139 (2010).

[160] Wang, H. & Li, M. Unifying the criteria of elastic stability of solids. *Journal of Physics: Condensed Matter* **24**, 245402 (2012).

[161] Karki, B. B., Ackland, G. J. & Crain, J. Elastic instabilities in crystals from ab initio stress - strain relations. *Journal of Physics: Condensed Matter* **9**, 8579 (1997).

[162] Wang, J., Yip, S., Phillpot, S. R. & Wolf, D. Crystal instabilities at finite strain. *Phys. Rev. Lett.* **71**, 4182–4185 (1993).

[163] Grimvall, G., Magyari-Köpe, B., Ozoliņš, V. & Persson, K. A. Lattice instabilities in metallic elements. *Rev. Mod. Phys.* **84**, 945–986 (2012).

[164] Sha, X. & Cohen, R. E. First-principles thermoelasticity of bcc iron under pressure. *Phys. Rev. B* **74**, 214111 (2006).

[165] Wallace, D. *Thermodynamics of crystals* (Wiley, 1972).

[166] Honeycutt, J. D. & Andersen, H. C. Molecular dynamics study of melting and freezing of small Lennard-Jones clusters. *The Journal of Physical Chemistry* **91**, 4950–4963 (1987).

[167] Antonangeli, D. *et al.* Elastic anisotropy in textured hcp-iron to 112 GPa from sound wave propagation measurements. *Earth and Planetary Science Letters* **225**, 243–251 (2004).

[168] Mao, W. L. *et al.* Experimental determination of the elasticity of iron at high pressure. *Journal of Geophysical Research: Solid Earth* **113**, 1–14 (2008).

[169] Mattesini, M. *et al.* Candy Wrapper for the Earth's inner core. *Scientific reports* **3**, 2096 (2013).

[170] Côté, A. S., Vočadlo, L. & Brodholt, J. P. Light elements in the core: Effects of impurities on the phase diagram of iron. *Geophysical Research Letters* **35**, L05306 (2008).

[171] Côté, A. S., Vočadlo, L., Dobson, D. P., Alfè, D. & Brodholt, J. P. Ab initio lattice dynamics calculations on the combined effect of temperature and silicon on the stability of different iron phases in the Earth's inner core. *Physics of the Earth and Planetary Interiors* **178**, 2–7 (2010).

[172] Asanuma, H. *et al.* Phase relations of Fe-Si alloy up to core conditions: Implications for the earth inner core. *Geophysical Research Letters* **35**, L12307 (2008).

[173] Kuwayama, Y., Hirose, K., Sata, N. & Ohishi, Y. Phase relations of iron and ironnickel alloys up to 300gpa: Implications for composition and structure of the earth's inner core. *Earth and Planetary Science Letters* **273**, 379 – 385 (2008).

[174] Sha, X. & Cohen, R. E. Elastic isotropy of ε-Fe under earth's core conditions. *Geophysical Research Letters* **37**, L10302 (2010).

[175] Nguyen, J. H. & Holmes, N. C. Melting of iron at the physical conditions of the earth's core. *Nature* **427**, 339–342 (2004).

[176] Souvatzis, P., Eriksson, O., Katsnelson, M. I. & Rudin, S. P. Entropy driven stabilization of energetically unstable crystal structures explained from first principles theory. *Phys. Rev. Lett.* **100**, 095901 (2008).

[177] Steinle-Neumann, G., Stixrude, L. & Cohen, R. E. First-principles elastic constants for the hcp transition metals fe, co, and re at high pressure. *Phys. Rev. B* **60**, 791–799 (1999).

[178] Steinle-Neumann, G., Stixrude, L., Cohen, R. E. & Gulseren, O. Elasticity of iron at the temperature of the earth's inner core. *Nature* **413**, 57–60 (2001).

[179] Bernard, S. & Bercegeay, C. First-principles equations of state and elastic properties of seven metals. *Physical Review B* **72** (2005).

[180] Umemoto, K. & Wentzcovitch, R. M. Prediction of an U_2S_3-type polymorph of Al_2O_3 at 3.7 Mbar. *Proceedings of the National Academy of Sciences of the United States of America* **105**, 6526–30 (2008).

[181] Gutiérrez, G., Menéndez-Proupin, E. & Singh, A. K. Elastic properties of the bcc structure of bismuth at high pressure. *Journal of Applied Physics* **99**, 103504 (2006).

[182] Wilson, H. F. & Militzer, B. Interior Phase Transformations and Mass-Radius Relationships of Silicon-Carbon Planets. *The Astrophysical Journal* **793**, 34 (2014).

[183] Wu, S. *et al.* Identification of post-pyrite phase transitions in SiO_{2} by a genetic algorithm. *Physical Review B* **83**, 184102 (2011).

[184] Bradley, D. *et al.* Diamond at 800 GPa. *Physical Review Letters* **102**, 075503 (2009).

[185] Jeanloz, R. *et al.* Achieving high-density states through shock-wave loading of precompressed samples. *Proceedings of the National Academy of Sciences of the United States of America* **104**, 9172–9177 (2007).

[186] Godwal, B., González-Cataldo, F., Verma, A., Stixrude, L. & Jeanloz, R. Stability of iron crystal structures at 0.31.5 TPa. *Earth and Planetary Science Letters* **409**, 299–306 (2015).

[187] Driver, K. *Establishing Quantum Monte Carlo and Hybrid Density Functional Theory as benchmarking tools for complex solids.* Ph.D. thesis, The Ohio State University (2011).

[188] González, D. & Davis, S. Fitting of interatomic potentials without forces: a parallel particle swarm optimization algorithm. *Computer Physics Communications* **185**, 3090–3093 (2014).

[189] Guillot, T. The interiors of giant planets: Models and outstanding questions. *Annual Review of Earth and Planetary Sciences* **33**, 493–530 (2005).

[190] Stacey, F. D. High pressure equations of state and planetary interiors. *Reports on Progress in Physics* **68**, 341 (2005).

[191] Stacey, F. D. The K-primed approach to high-pressure equations of state. *Geophysical Journal International* **143**, 621–628 (2000).

[192] Faken, D. & Jónsson, H. Systematic analysis of local atomic structure combined with 3D computer graphics. *Computational Materials Science* **2**, 279–286 (1994).

[193] Tsuzuki, H., Branicio, P. S. & Rino, J. P. Structural characterization of deformed crystals by analysis of common atomic neighborhood. *Computer Physics Communications* **177**, 518–523 (2007).

[194] Kittel, C. *Introduction to Solid State Physics* (John Wiley & Sons, Inc., New York, 1986), 6th edn.